



**HAL**  
open science

# Segmentation and Symbolic Representation of Brain Vascular Network: Application to ArterioVenous Malformations

Fan Li

► **To cite this version:**

Fan Li. Segmentation and Symbolic Representation of Brain Vascular Network: Application to ArterioVenous Malformations. General Mathematics [math.GM]. Université Paris-Est, 2016. English. NNT: 2016PESC1048 . tel-01526456

**HAL Id: tel-01526456**

**<https://theses.hal.science/tel-01526456>**

Submitted on 23 May 2017

**HAL** is a multi-disciplinary open access archive for the deposit and dissemination of scientific research documents, whether they are published or not. The documents may come from teaching and research institutions in France or abroad, or from public or private research centers.

L'archive ouverte pluridisciplinaire **HAL**, est destinée au dépôt et à la diffusion de documents scientifiques de niveau recherche, publiés ou non, émanant des établissements d'enseignement et de recherche français ou étrangers, des laboratoires publics ou privés.



DOCTORAL SCHOOL "MATHEMATICS AND SCIENCE AND TECHNOLOGIES OF  
INFORMATION AND COMMUNICATION"

Thesis to obtain the Doctor of Philosophy grade of the University Paris-Est

Speciality: **Signal, Image, Automatic**

Fan LI

**Segmentation and Symbolic Representation of Cerebral Vascular  
Network: applied to modelize ArterioVenous Malformations**

01 Juin 2016

Pr.	Eric PETIT	University of Paris Est Créteil	(Director)
Dr.	Yasmina CHENOUNE	ESME Sudria Engineering School	(Supervisor)
Dr.	Olena TANKYEVYCH	University of Paris Est Créteil	(Supervisor)

Composition of the jury:

Pr.	Yacine AMIRAT	University of Paris Est Créteil	(President)
Pr.	Maciej ORKISZ	University of Claude Bernard Lyon 1	(Referee)
Pr.	Nicolas PASSAT	University of Reims Champagne-Ardenne	(Referee)
Dr.	Catalin FETITA	Télécom SudParis	(Examinator)
Dr.	Hocine REDJEM	Hospital of Rothschild Foundation	(Examinator)

© 01 Juin 2016

*To my parents and my friends*



## ABSTRACT

---

The processing and analysis of 3D Rotational Angiographic images (3DRA) of high spatial resolution to facilitate intervention planning in interventional neuro-radiology is a new and booming research area. Neuroradiologists need interactive tools for the planning of embolization procedures and the optimization of the guidance of micro-catheters during endovascular interventions. The exploitation of imaging data to help in diagnosis and treatment requires the development of robust algorithms and efficient methods. These methods allow integrating information included in these images in order to extract useful anatomical descriptors during preoperative and peroperative phases.

This thesis is dedicated to the development of a complete processing pipeline including segmentation, three-dimensional (3D) reconstruction and symbolic representation of cerebral vessels from 3DRA images, aiming to facilitate the embolization intervention planning for the treatment of cerebral ArterioVenous Malformations (AVMs).

The first part of the work is devoted to the study of the different approaches used for the segmentation of vessels. Two segmentation methods are then proposed. First, a 2D slice-by-slice segmentation method is developed, followed by a robust vessel tracking process that enables detecting bifurcations and further following several branches of the same vessel. A mesh based on the Constrained Delaunay triangulation allows then the 3D reconstruction and visualization of the obtained vessels.

Then, a region growing based method is introduced to segment 3DRA images. It presents the advantages of being faster and processing the whole 3D volume of images. This method is region growing based. The 3D process starts from an initial pre-segmented slice using the geodesic reconstruction, where the seeds are automatically placed. Finally, a representation of the vasculature is obtained, in which these three entities are clearly visible: the feeding arteries, the draining veins and the nidus.

The second part of the thesis is devoted to the symbolic representation of the vessels. The hierarchical study of the skeleton allows giving a graphic description of the cerebral vascular network. From this graphic description, the vessels and their branches are labeled and one or more vessels can be isolated from the rest of network for a more accurate visual analysis, which is not possible with the original 3D reconstructions. Moreover, this improves the determination of the optimal paths for the AVM embolization and reduces the complexity due to the entanglement of the malformed vessels.

Thus the complete processing pipeline developed leads to a precise 3D description of the vessels. It allows a better understanding of the cerebral vascular network structure and provides the possibility to neuroradiologists of extracting anatomical and geometric descriptors (size, diameter *etc.*) of the vessels. Finally, a verification step of the results by a neuroradiology expert enabled clinical validation of the 3D segmentation and reconstruction results. The integration of the developed algorithms in a user-friendly graphical interface should be achieved to allow the exploitation of our results in clinical routine.

**Keywords:** medical image processing, segmentation, cerebral arteriovenous malformations, symbolic representation, vessel network analysis

## RÉSUMÉ

---

Le traitement et l'analyse d'images angiographiques rotationnelles 3D (3DRA) de haute résolution spatiale pour l'aide à la planification d'interventions en neuro-radiologie interventionnelle est un domaine de recherche récent et en plein essor. Les neuroradiologues ont besoin d'outils interactifs pour la planification des procédures d'embolisation et l'optimisation du guidage de microcathéters durant les interventions endovasculaires. L'exploitation des données d'imagerie pour l'aide au diagnostic et la thérapeutique requiert le développement d'algorithmes robustes et de méthodes efficaces. Ces méthodes permettent d'intégrer les informations contenues dans ces images pour en extraire des descripteurs anatomiques utiles durant les phases pre et per-opératoires.

Cette thèse est dédiée au développement d'une chaîne de traitement complète comprenant la segmentation, la reconstruction tridimensionnelle (3D) et la représentation symbolique de vaisseaux cérébraux à partir d'images 3DRA, pour faciliter la planification d'interventions d'embolisation pour le traitement de Malformations ArtérioVeineuses cérébrales (MAVs).

La première partie du travail est consacrée à l'étude des différentes approches utilisées en segmentation des vaisseaux. Deux méthodes de segmentation sont ensuite proposées. Tout d'abord, une méthode de segmentation 2D coupe par coupe est développée ainsi qu'une technique robuste de suivi de vaisseaux permettant de détecter les bifurcations et de poursuivre le tracking de plusieurs branches du même vaisseau. Un maillage basé sur la triangulation Contrainte de Delaunay permet ensuite la reconstruction et la visualisation 3D des vaisseaux ainsi obtenus. Ensuite, une méthode de segmentation 3D automatisée des images 3DRA est développée, elle présente l'avantage d'être plus rapide et de traiter le volume d'images entier en 3D. Cette méthode est basée sur la croissance de régions. Le processus 3D démarre à partir d'une coupe initiale pré-segmentée en utilisant la reconstruction géodésique et sur laquelle les germes sont placés de manière automatique. Finalement, une représentation du réseau vasculaire sur laquelle on distingue clairement les trois entités que sont les artères, les veines

drainantes et le nidus est obtenue.

La deuxième partie de la thèse est consacrée à la représentation symbolique des vaisseaux. L'étude hiérarchique du squelette permet de donner une description graphique du réseau vasculaire cérébral. A partir de cette description graphique, les vaisseaux et leurs branches sont labellisés et un ou plusieurs vaisseaux peuvent être isolés du reste du réseau pour une analyse visuelle plus précise, ce qui n'est pas possible avec les reconstructions 3D du constructeur. De plus, cette représentation améliore la détermination des chemins optimaux pour l'embolisation de la MAV et réduit la complexité due à l'enchevêtrement des vaisseaux malformés.

La chaîne de traitement complète ainsi développée aboutit à une description 3D précise des vaisseaux. Elle permet une meilleure compréhension structurelle du réseau vasculaire cérébral et offre aux neuroradiologues la possibilité d'extraire des descripteurs anatomiques, et géométriques (taille, diamètre, *etc.*) des vaisseaux. Enfin, une étape de vérification des résultats par un expert neuroradiologue a permis la validation clinique des résultats de segmentation et de reconstruction 3D. L'intégration des algorithmes développés dans une interface graphique intuitive et facile d'utilisation devra être faite pour permettre l'exploitation de nos résultats en routine clinique.

**Mots clés:** traitement d'image médicale, segmentation, malformations artérioveineuse cérébrales, représentation symbolique, analyse de réseaux vasculaires

## ACKNOWLEDGEMENT

---

Foremost, I would like to express my utmost gratitude to my PhD director, Prof. Éric PETIT. This thesis would not be possible without his endless help and selfless guidance. His kindness, generosity, patience and encouragements have accompanied me all the way during the past four years. He is more like my "life mentor" than a PhD director. My acknowledgements of his supports are indeed beyond words.

I am endlessly grateful to my thesis supervisor, Dr. Yasmina CHENOUNE, for giving me the opportunity to lance my doctoral project. I have been lucky enough to spend these years under her supervisions. She is such a nice, amiable and charming woman, who is always there for me. It is truly great pleasure to work with her. I really appreciated all the efforts she has made.

I would also give my special acknowledgements to Dr. Raphaël BLANC and Dr. Michel PIOTIN, as well as all the personnel from the Hospital of Rothschild Foundation.

I would like to equally acknowledge the other thesis supervisor: Dr. Olena TANKYEVYCH. Her patient explications and extensive knowledge broadened my horizon and allowed me to learn faster than ever before. I really wish to continue the cooperation with her in my upcoming career.

I am truly grateful to every committee member of my thesis defense. Especially I wish to thank Pr. Maciej ORKISZ from University of Claude Bernard Lyon 1 (CREATIS, CNRS UMR 5220) and Pr. Nicolas PASSAT from University of Reims Champagne-Ardenne (EA 3804 CReSTIC) for having accepted to be my PhD thesis referees. I really appreciate them for having read my manuscript even the given time is inadequate. Besides, I am equally grateful to Dr. Catalin FETITA from Télécom SudParis and Hocine REDJEM from the Hospital of Rothschild Foundation. It is really great honour to have them being my examiners.

Notably, I need to give my acknowledgements to the ESME Sudria Engineering School for funding my thesis project. In fact I have spend most of my doctoral time here, and it is like home to me. I am grateful to Dr. Sebastien HERRY, Salma REBAI, Karim AIT ABDERRAHIM and all the other researchers here, for their help, support and collaboration.

I would like as well to thank Michel COUPRIE and Gilles BERTRAND for their help on my project.

My greatest appreciation goes to my closest friends, Recca, Weiwei and Haotian, they have always been on my side, never giving me up. They have encouraged me to keep fighting and be happy. Together, we have shared too much joy as well as bitterness. Thanks to Banban and Mi, they are like my big brother and sister, ready to help me whenever and whatever. I shall be forever grateful to have them all.

Last but not least, I own all the "success" to my dearest parents. They have sacrificed too much for me and encouraged me to follow my dreams. Even we seldom see each other due to the distance, I have missed them day and night.

Thanks again for the people above, as well as those I forgot to mention. I do believe that the PhD career is a milestone to my life, yet the longest journey begins with the first step, and tomorrow is another day. Nothing is impossible to a willing heart, and I may always remind myself to be hungry and keep learning.

# CONTENTS

---

1	INTRODUCTION	1
1.1	Motivations of this work . . . . .	1
1.2	Contents of this thesis . . . . .	2
2	BRAIN ARTERIOVENOUS MALFORMATIONS	3
2.1	Background of brain arteriovenous malformations . . . . .	5
2.1.1	Definition . . . . .	5
2.1.2	Pathogenesis . . . . .	8
2.1.3	Epidemiology . . . . .	8
2.1.4	Symptoms . . . . .	8
2.1.5	Classifications . . . . .	9
2.2	Diagnosis and treatments . . . . .	11
2.2.1	Microsurgical resection . . . . .	11
2.2.2	Stereotactic radiosurgery . . . . .	11
2.2.3	Endovascular embolization . . . . .	12
2.2.4	Treatment choice . . . . .	13
2.3	Imaging techniques of brain arteriovenous malformations . . . . .	13
2.3.1	Angiography and digital subtraction angiography images . . . . .	13
2.3.2	Computed tomography angiography images . . . . .	14
2.3.3	Magnetic resonance angiography images . . . . .	15
2.3.4	3D rotational angiography images . . . . .	16
2.4	Conclusion . . . . .	18
3	SEGMENTATION AND VISUALIZATION OF CEREBRAL VASCULAR NETWORK	21
3.1	Introduction . . . . .	23
3.2	Classical methods and techniques for vessels segmentation . . . . .	24
3.2.1	Thresholding . . . . .	25
3.2.2	Statistical model analysis . . . . .	26
3.2.3	Deformable models . . . . .	27
3.2.4	Pattern recognition . . . . .	29
3.2.5	Region growing . . . . .	31
3.2.6	Mathematical morphology approaches . . . . .	35

3.3	Specific models based on vessel features . . . . .	37
3.3.1	Tube-like multi-scale filters . . . . .	37
3.3.2	Geometrical models . . . . .	39
3.3.3	Discussion . . . . .	40
3.4	Vessel reconstruction and 3D visualization . . . . .	42
3.4.1	Vessel reconstruction . . . . .	42
3.4.2	Vessel visualization . . . . .	42
3.5	Contributions . . . . .	47
3.5.1	2D slice-by-slice segmentation . . . . .	48
3.5.2	3D region growing segmentation . . . . .	52
3.5.3	3D vessels reconstruction . . . . .	57
3.5.4	Separation of the arteries, nidus and veins . . . . .	57
3.6	Results . . . . .	60
3.7	Conclusion . . . . .	74
4	SYMBOLIC REPRESENTATION OF BRAIN VASCULAR NETWORK	75
4.1	Introduction . . . . .	77
4.2	State of the art . . . . .	79
4.2.1	Topology study . . . . .	79
4.2.2	Skeletonization . . . . .	80
4.2.3	Conversion from skeleton to graph . . . . .	84
4.2.4	Topological and hierarchical analysis . . . . .	87
4.3	Proposed method . . . . .	91
4.3.1	Skeletonization . . . . .	91
4.3.2	Conversion from skeleton to graph . . . . .	91
4.3.3	Geometrical measurements . . . . .	98
4.4	Results . . . . .	99
4.4.1	Results of the synthetic vascular network . . . . .	99
4.4.2	Results of the clinical vascular network . . . . .	104
4.5	Discussion . . . . .	110
5	CONCLUSION	115
5.1	Contributions . . . . .	115
5.2	Perspectives . . . . .	116
<b>I</b>	<b>Annexes</b>	<b>119</b>
A	ANNEXES	121

A.1 Geodesic reconstruction . . . . .	121
A.2 Distance regularized level set evolution . . . . .	122
BIBLIO	125

## LIST OF FIGURES

---

Figure 2.1	The vessel connection in normal brain . . . . .	6
Figure 2.2	The blood circulation in human body . . . . .	6
Figure 2.3	Sketch of different features of Brain ArterioVenous Malformation . . . . .	7
Figure 2.4	Illustration of embolization procedure . . . . .	12
Figure 2.5	An example of DSA image . . . . .	14
Figure 2.6	Examples of CTA and MRA brain images . . . . .	15
Figure 2.7	Philips Allura System . . . . .	17
Figure 2.8	3DRA images and the reconstruction . . . . .	18
Figure 2.9	AVM treatment with multimodalities . . . . .	19
Figure 3.1	Evolution of the 3D charged fluid model . . . . .	29
Figure 3.2	Example of fuzzy-based segmentation . . . . .	31
Figure 3.3	Shape-based region growing . . . . .	32
Figure 3.4	Branch-based region growing . . . . .	33
Figure 3.5	Region growing for flower segmentation . . . . .	35
Figure 3.6	An example of AVM delineation . . . . .	36
Figure 3.7	Segmentation results in an intra-patient case . . . . .	37
Figure 3.8	Hessian eigenvalues shape-space . . . . .	38
Figure 3.9	Hessian-based multi-scale filter . . . . .	39
Figure 3.10	An illustration of generalized cylinder model . . . . .	41
Figure 3.11	Shape-enhanced maximum intensity projection . . . . .	44
Figure 3.12	An example of smoothed surface rendering . . . . .	45
Figure 3.13	Small anatomic tree structures are modelled by placing ball-shaped markers and represented as a special variant of splines	46
Figure 3.14	Hybrid combination of the direct volume rendering of bone structures and surface rendering of intra-hepatic structures (liver, vascular systems, tumours in the right view). The bone structures serve as anatomic reference for the intra-hepatic structures [1]. . . . .	47
Figure 3.15	Logarithmic histogram of pixels intensities of a 3DRA image, normalized between 0 and 255. . . . .	48
Figure 3.16	The schema of our tracking algorithm . . . . .	50

Figure 3.17	The interface of our segmentation program . . . . .	51
Figure 3.18	An illustration of 2D vessel segmentation with geodesic reconstruction . . . . .	52
Figure 3.19	An illustration of 2D vessel segmentation with level set . . .	53
Figure 3.20	An illustration of vessel-tracking with the proposed method.	53
Figure 3.21	3D neighborhoods. From left to right: 6-connectivity, 18-connectivity, 26-connectivity. . . . .	55
Figure 3.22	Results of the separation of vessel network . . . . .	59
Figure 3.23	Comparison of reconstruction . . . . .	62
Figure 3.24	Segmentation algorithm . . . . .	63
Figure 3.25	An example of reconstruction . . . . .	64
Figure 3.26	The sensitivity of our segmentation to parameter . . . . .	64
Figure 3.27	Examples of vessel reconstruction . . . . .	65
Figure 3.28	Comparison of the segmentation results of clinical data (Patient 1) . . . . .	66
Figure 3.29	Comparison of the segmentation results of clinical data (Patient 2) . . . . .	67
Figure 3.30	Comparison of the segmentation results of clinical data (Patient 3) . . . . .	68
Figure 3.31	Comparison of the segmentation results of clinical data (Patient 4) . . . . .	69
Figure 3.32	Comparison of the segmentation results of clinical data (Patient 5) . . . . .	70
Figure 3.33	Comparison of the segmentation results of clinical data (Patient 6, series 1) . . . . .	71
Figure 3.34	Comparison of the segmentation results of clinical data (Patient 6, series 2) . . . . .	72
Figure 3.35	Comparison of the segmentation results of clinical data (Patient 7, 8, 9, 10) . . . . .	73
Figure 4.1	An example of one stage of mapping AVM interconnectivity	78
Figure 4.2	Example of simple points . . . . .	81
Figure 4.3	Comparison of symmetric and asymmetric results . . . . .	83
Figure 4.4	Decomposition of skeleton branches with the analysis of skeleton connectivity information . . . . .	85
Figure 4.5	A graph based on the skeleton . . . . .	86
Figure 4.6	Visualization of different subtrees of intra-cerebral vasculature with AVM . . . . .	86

Figure 4.7	An illustration of embolization intervention planning from nidus to ICA . . . . .	88
Figure 4.8	Study of the graph topology with Strahler Ordering . . . . .	89
Figure 4.9	Different hierarchical models of network . . . . .	90
Figure 4.10	Classification of skeleton points from phantom image . . . . .	92
Figure 4.11	Classification of skeleton points to branch points, terminal points and junctions . . . . .	92
Figure 4.12	Classification of the skeleton points into three types from the number of neighbourhood . . . . .	94
Figure 4.13	The kissing vessel issue . . . . .	97
Figure 4.14	Several possible graph models of vascular skeleton network . . . . .	97
Figure 4.15	Construction of graph from the skeleton of phantom image . . . . .	97
Figure 4.16	Diameter estimation with medial axis . . . . .	99
Figure 4.17	The symbolic representation results on a synthetic vascular tree . . . . .	101
Figure 4.18	Bland Altman plot of mean radius . . . . .	104
Figure 4.19	Geometrical features of synthetic vascular tree . . . . .	105
Figure 4.20	Synthetic vascular images with the presence of loop and their 3D graph representations . . . . .	106
Figure 4.21	An example of synthetic vascular image with multi-edges and its graph representation in 2D and 3D . . . . .	107
Figure 4.22	Illustration of topological correction . . . . .	107
Figure 4.23	Analysis of vessel tree topology . . . . .	108
Figure 4.24	Selective visualization of vascular tree . . . . .	109
Figure 4.25	Overlay of the obtained results on MIP images . . . . .	111
Figure 4.26	Segmentation correction . . . . .	113
Figure 5.1	The interface of VesselExplorer software . . . . .	117

## LIST OF TABLES

---

Table 2.1	The Spetzler-Martin grading system for AVMs . . . . .	10
Table 2.2	Recommended treatment option order of AVMs . . . . .	13
Table 4.1	Topological classification of 3D points according to the values of $C$ and $\bar{C}$ . . . . .	80
Table 4.2	The different geometrical parameters of one clinical dataset	110

## ACRONYMS

---

3DRA	3D Rotational Angiography
AVMs	ArterioVenous Malformations
BAT	Bolus Arrival Time
CDT	Constrained Delaunay Triangulation
CE	Contrast Enhanced
CT	Computed Tomography
CTA	Computed Tomography Angiography
CVP	Closest Vessel Projection
DCE	Dynamic Contrast Enhanced
DSA	Digital Subtraction Angiography
DT	Distance Transformation
EM	Expectation Maximization
FMM	Finite Mixture Model
GAR	Geodesic Active Regions
GVF	Gradient Vector Flow
HSV	Hue Saturation Value
ICH	Intra-Cerebral Haemorrhage
IVUS	Intra-Vascular UltraSound
KNN	K-Nearest Neighbors
MIP	Maximum Intensity Projection
MPR	Multi Planar Reconstruction

MR	Magnetic Resonance
MRA	Magnetic Resonance Angiography
MRI	Magnetic Resonance Imaging
MGU	Maxwell Gaussian Uniform
MU	Maxwell Uniform
PC	Phase Contrast
PDF	Probability Density Function
ROI	Region Of Interest
SAH	Sub Arachnoid Haemorrhage
SE	Structuring Element
SR	Surface Rendering
SVM	Support Vector Machine
TOF	Time Of Flight
TTP	Time To Peak
VR	Volume Rendering
VRG	Variational Region Growing



## INTRODUCTION

---

### 1.1 MOTIVATIONS OF THIS WORK

The term of cerebral *ArterioVenous Malformations* (AVM) denotes vascular malformations between arteries and veins of the brain, where the two components are interconnected by a direct circuit. The arteriovenous shunt may cause increased blood pressure in the draining veins and thus lead to breakage and cerebral hemorrhage. The embolization intervention is an efficient treatment therapy dealing with such disease. It consists in navigating with micro-catheters from the groin throughout the intracranial vasculature and injecting a glue-like material to occlude the feeding arteries and draining veins, in order to isolate the malformation (nidus) and cut its blood support. A detailed introduction of AVM and embolization procedure will be presented in [Chapter 2](#).

Since the cerebral vascular network is highly complex, embolization intervention is a difficult task that may last several hours. A prior knowledge of network structure is thus indispensable for a successful treatment management and intervention planning. Particularly for preparing the embolization intervention, the required information include the precise position and size information of the nidus, the identification of the feeding arteries, the draining veins and the geometrical and hierarchical parameters of the vessels.

Several angiographic imaging techniques (DSA, MRA, CTA, 3DRA, *etc.*) allow obtaining such information from vascular images in two or three dimensions (2D or 3D, see [Section 2.3](#)). Some robust and accurate post-processing algorithms and techniques are required for the exploitation, the analysis and the interpretation of these high resolution images.

In fact, the latest healthcare systems can deliver an initial segmentation and even a 3D visualization of vascular network. By registering different modalities and with 3D visualizations, the neuroradiologists attempt to manually design the optimal navigation paths of micro-catheter during the embolization procedure. However, such approaches present some limitations. An entire brain vascular network brings too much useless information, the vessels overlappings may also influence the analyses.

In addition, the available 3D reconstructions from manufacturer imaging systems are solely dedicated to the visualization of cerebral vasculature but do not provide an assistance to analyse and interpret the complex structure of AVM to the neuroradiologists. The clinical experiments require the possibility of 3D manipulation of the vascular network for the purpose of tracking or isolating a specific vessel to study its trajectory, termination and possible connections with the other vessels. As far as we know, there are no existing tools that can provide such solution.

The aim of our work is to provide a robust and interactive application, which meets the need of the neuroradiologists for the planning of embolization procedures and the optimization of the guidance of micro-catheters during endovascular interventions. The analysis is based on the exploitation of *3D Rotational Angiographic images* (3DRA), which is a new promising modality, offering high spatial resolution images.

## 1.2 CONTENTS OF THIS THESIS

This thesis is organized as follows. The [Chapter 2](#) contains the necessary background to understand the medical context of this study. We first introduce some elementary anatomical and pathological notions about the cerebral AVM disease. Then, we explain the two steps of diagnosis and treatments of AVM with a particular emphasis on the embolization procedure through endovascular interventions. In the last section we show the principal angiographic imaging techniques that are widely applied for vessels abnormalities diagnosis and treatment therapies.

Our contributions to the segmentation of cerebral vessels in 3DRA images are presented in [Chapter 3](#). Two segmentation methods are proposed: 1) A 2D slice-by-slice segmentation approach followed by a robust vessel tracking algorithm and 2) A 3D region growing based segmentation method. Then, a technique of 3D reconstruction of the vessels using the Constrained Delaunay Triangulation is developed. Thus, a 3D representation of the vasculature is significantly contributed to address the studied problem that allows distinguishing the three entities: arterial network, draining veins and nidus. Another contribution deals with the symbolic representation of the arterial vascular network, as presented in [Chapter 4](#). In this chapter, we have mentioned the topology study of vascular network, the skeletonization and the conversion from the skeleton to graph representation.

The conclusion and perspectives are finally developed in [Chapter 5](#).

## BRAIN ARTERIOVENOUS MALFORMATIONS

---

### Contents

---

2.1	Background of brain arteriovenous malformations . . . . .	5
2.1.1	Definition . . . . .	5
2.1.2	Pathogenesis . . . . .	8
2.1.3	Epidemiology . . . . .	8
2.1.4	Symptoms . . . . .	8
2.1.5	Classifications . . . . .	9
2.2	Diagnosis and treatments . . . . .	11
2.2.1	Microsurgical resection . . . . .	11
2.2.2	Stereotactic radiosurgery . . . . .	11
2.2.3	Endovascular embolization . . . . .	12
2.2.4	Treatment choice . . . . .	13
2.3	Imaging techniques of brain arteriovenous malformations . . . . .	13
2.3.1	Angiography and digital subtraction angiography images . . . . .	13
2.3.2	Computed tomography angiography images . . . . .	14
2.3.3	Magnetic resonance angiography images . . . . .	15
2.3.4	3D rotational angiography images . . . . .	16
2.4	Conclusion . . . . .	18

---



## 2.1 BACKGROUND OF BRAIN ARTERIOVENOUS MALFORMATIONS

### 2.1.1 Definition

Nutrient and oxygen exchange in our internal body are realized by the blood circulation. The arteries and veins communicate through the capillary bed (see [Figure 2.1](#)). Arteries provide the transport of blood directly from the heart and lungs toward the terminals of the body. The resources in the arteries are retrieved by capillaries in order to supply the needs and pick up cell metabolic wastes. The capillaries pass blood into the veins, which deals with the brain drain blood and other agencies and return them to the heart and lungs, to acquire new nutrients and oxygen (see [Figure 2.2](#)). As artery is responsible for the transportation of blood from the heart, artery walls are much thicker and more muscular compared to vein walls in order to endure a higher pressure.

Since the first recognition over a century ago [2], cerebral *ArterioVenous Malformations* (AVMs) was regarded as one of the most surgically challenging diseases by neurosurgeons. This disease involves an abnormal tangle of vessels in the brain that leads to a direct communication between the feeding arteries and the draining veins without transition through capillary network [3]. An illustration of AVM is shown in [Figure 2.3](#). Three main parts can be distinguished in this malformation:

- multiple feeding arteries
- enlarged draining veins
- tangle of vessels or nidus between them

Due to this direct connection, the enlarged draining veins connected to nidus endure a higher pressure than normal. However, it is unknown if this flow is a cause or an effect of the abnormal vessels, or both. One hypothesis is that high-pressure blood uses the path of least resistance. Another is that the AVM itself uses blood vessels. In any case, the blood goes through the AVM and not through available capillary beds. This redirection is called a shunt. Due to the shunting, the AVM dilates with time. This dilation weakens veins and makes them susceptible to haemorrhage. Feeding arteries become susceptible to aneurysms. A haemorrhage in the brain is a type of stroke where a blood vessel ruptures and bleeds into the brain. This results in loss of temporary or permanent normal function. The amount of damage depends on how much blood was leaked.

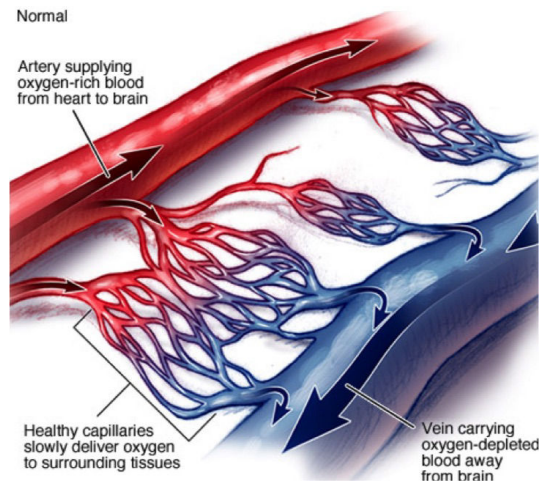


Figure 2.1: The vessel connections in normal brain: the arteries and the veins are connected by capillaries. Source: Mayo Clinic.

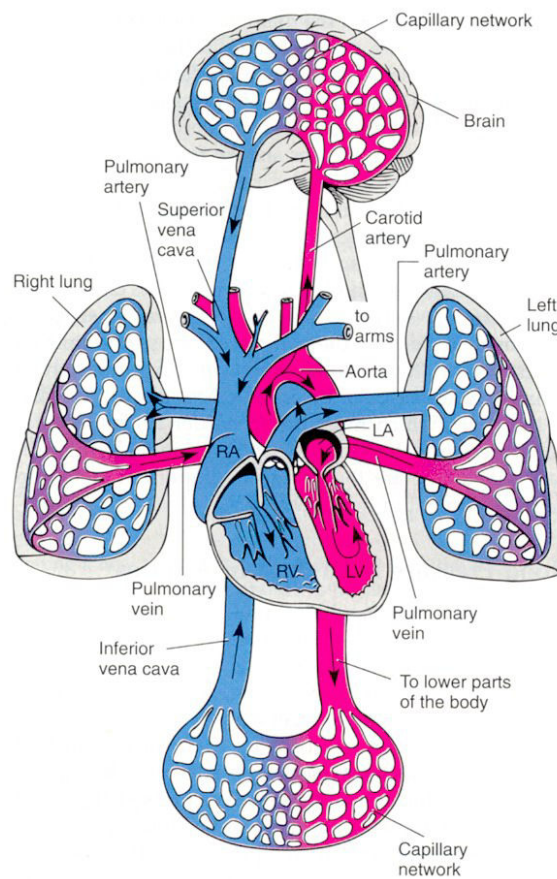


Figure 2.2: The blood circulation in human body, source unknown.

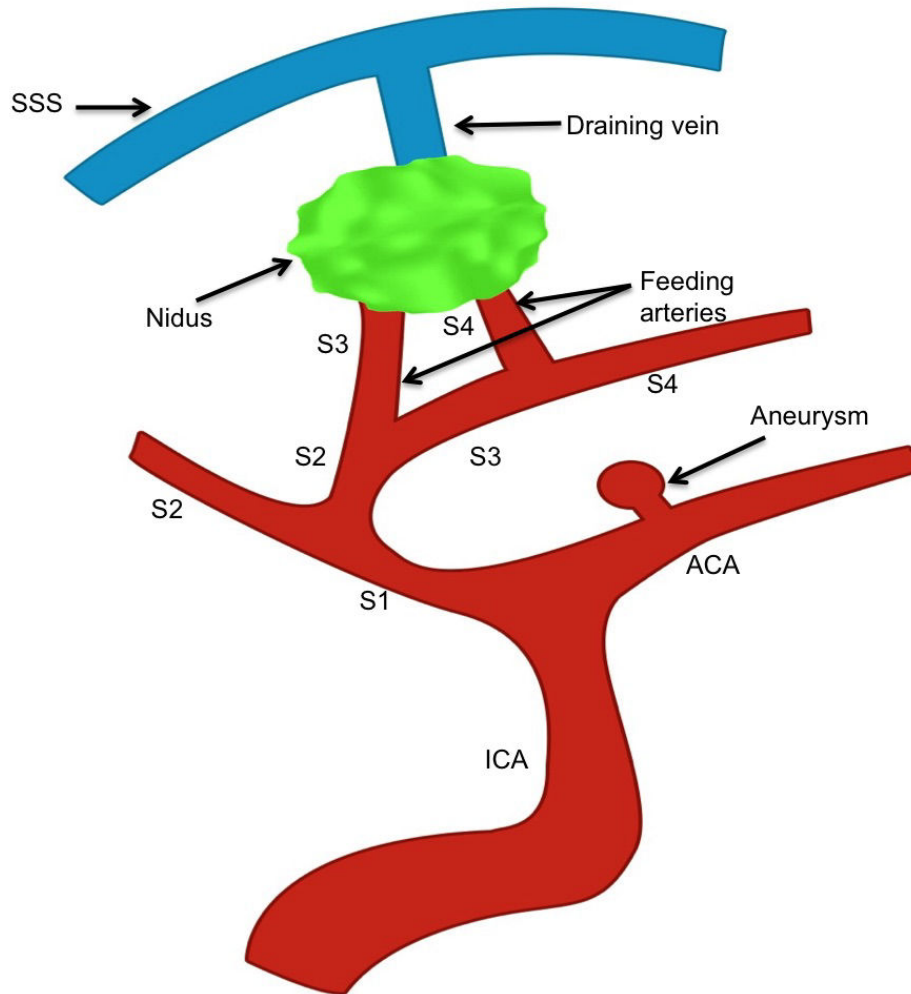


Figure 2.3: **Sketch of different features of Brain ArterioVenous Malformation**

This figure demonstrates the diagrammatic sketch for most brain AVM cases: the lesion of malformation is formed by one or several feeding arteries, draining veins and the nidus between them. The blood is shunted from feeding arteries to draining veins through the nidus. The feeding arteries are normally segment branches derived from the ICA of the Willis Circle. The draining veins are connected to SSS directly or indirectly. ICA=Internal Carotid Artery. ACA=Anterior Cerebral Artery. S1, S2, S3, S4=first, second, third, fourth segment of middle cerebral artery. SSS=Superior Sagittal Sinus.

### 2.1.2 Pathogenesis

The brain AVMs are generally considered to be congenital. The malformations are too small to be detected in foetal development and the pathogenesis for particular case is uncertain. Some people suggested that brain AVM is a consistent congenital vascular plexus since in the embryonic stage [4], while others proposed that they resulted from some disturbances in the dynamic remodelling process such as venous occlusion, venous stenosis and the flow-related differentiation of vasculature [5]. From all these speculations, we mention the work of Lasjaunias [6]. He drew the conclusion that the growth of nidus did not occur, the large AVMs resulted from mutations in embryogenesis and small AVMs were due to a later event of biological dysfunction.

### 2.1.3 Epidemiology

The Cooperative Study of Intracranial Aneurysms and Subarachnoid Haemorrhage is a long-term study on brain AVMs and aneurysms. According to their report, the prevalence effected at 140 – 500 in per 100000 unselected populations [7]. We can say that the incidence of brain AVMs is approximately 0.14 – 0.50% and in which 12% experience relative symptoms [8]. In another review from 1289 brain AVM patients, Hofmeister recorded that the mean diagnosis age was 31.2 years, and that 55% of patients were men [9]. This confirms that AVMs affect both men and women at the same rate in any age, but more likely to occur in young adults [10].

### 2.1.4 Symptoms

The most common symptom of AVMs is haemorrhage, which occurs in nearly half patients [11, 12]. The other presenting symptoms include headache, focal symptoms, seizures, stroke and even risk of morbidity or mortality. Most symptoms of AVMs are not revealed until the first time a bleed emerges. The risk of re-haemorrhage is 6% per year after the initial haemorrhage and other symptoms have obvious increasing presentation rates with the haemorrhagic occurrences [13]. These symptoms are caused in three ways:

- The bleed and rupture in the brain. This haemorrhagic damage is more common in small AVMs and can result in stroke. According to the rup-

ture location we can divide the *Intra-Cerebral Haemorrhage* (ICH) when the bleeding occurs in the brain and *Sub-Arachnoid Haemorrhage* (SAH) when it occurs in the space between the brain and skull. The brain AVMs account for 2% – 4% of all haemorrhagic strokes per year [14]. The following equations is clinically considered to predict the lifetime bleeding risk [15]:

$$\textit{lifetime bleeding risk}(\%) = 105 - \textit{Patient age}, \quad (2.1)$$

- The pressure of nidus against the surrounding tissue, especially in the cases of large AVMs. It may lead to several symptoms such as seizures, focal symptoms and hydrocephalus. For untreated AVMs, the risk of developing seizures is around 1% per year [8].
- The lack of oxygen in brain cells. Since the oxygen in the arterial blood was directly delivered to draining veins, the brain tissue cells surrounding the nidus hardly obtain enough oxygen from capillaries, which likely results in headaches in AVM patients.

### 2.1.5 Classifications

The brain AVMs can form anywhere in the cerebral vessel network. They can be simply divided into the following five types based on morphology and nidus locations [16] :

- Arteriovenous shunting malformations
- Arterial malformations (angiodyplasia and aneurysm)
- Venous malformations
- Carvernous malformations (cavernoma)
- Capillary malformations (telangiectasia)

The arteriovenous shunting malformations consist of an abnormal tangle of vessels where the blood shunt flows directly from feeding arteries into the draining veins without any intervening capillary bed. The arterial malformations and venous malformations form separately an abnormal vessel cluster of arteries and

Table 2.1: The Spetzler-Martin grading system for AVMs

Features	Score Assigned
Size of AVMs	
Small(< 3 cm)	1
Medium(3-6 cm)	2
Large(>6 cm)	3
Eloquence of adjacent brain	
Eloquent	0
Non-Eloquent	1
Pattern of venous drainage	
Superficial only	0
Deep	1

veins. Carvenoma and telangiectasia represent the malformations of enlarged capillary regions but no significant feeding arteries and draining veins can be observed in carvenoma. This classification can aid to measure blood pressure of malformations. Generally the pressure in the arteriovenous shunting malformations and arterial malformations is high, whereas the pressure in the nidus is low in other malformations types.

Another classification was introduced by Spetzler thirty years ago [17] and has been widely accepted in clinical experiments. In this 5-tiers classification, each AVM falls into one grade depending on three criteria: size of AVM, site of the lesion and pattern of venous drainage. The grades of AVMs are obtained by summing the scores assigned for each criteria in Table 2.1. This grading system can serve as a guide to estimate the pretreatment risk and assist in the decision-making of an appropriate treatment planning.

In order to improve this grading, some authors proposed some expansions by considering additional factors such as the patient's age [11], haemorrhagic presentation and nidal diffuseness [18], while some specialists propose to include subgroups for each grade and thus achieve a better outcome with nature history [19].

## 2.2 DIAGNOSIS AND TREATMENTS

AVMs are usually diagnosed as a result of bleeding or a scan for an unrelated disease. To ensure the diagnosis, the patients are suggested to undergo cerebral angiogram and other imaging tests such as MRA, CTA and 3DRA. These different imaging techniques are discussed in [Section 2.3](#).

Treatment issues and modalities may be single or multimodal therapy, and depend on a number of factors such as age and health condition of the patient, AVMs location, size, bleeding history and overall medical conditions. In general, three types of treatment are available: microsurgical resection, stereotactic radiation and endovascular embolization.

### 2.2.1 *Microsurgical resection*

The first attempt of surgical elimination of AVM by ligating the feeding arteries was effectuated in early 20th century without great success [20], it tended to be widely accepted after 1976 when Yasargil proved that the microsurgical resection could be safe, with non-mortality and minimal morbidity on experiment of 10 patients [21]. Afterwards the microsurgical resection remains the gold standard treatment, especially for small brain AVMs [22]. A recent study showed that the efficacy of surgery can reach as high as 94% – 100% for small malformations [23, 24]. To deal with large malformations, the microsurgical resection is applied before embolization procedure.

### 2.2.2 *Stereotactic radiosurgery*

The stereotactic radiosurgery is relatively a new method of treatment that involves targeting and obliterating the nidus of the AVMs using highly concentrated radiation. The most common method among these radiotherapies is called Gamma Knife [25, 26]. The success rate of obliteration for one single therapy ranges from 19% – 88% [27], depending on several factors such as radiation dose, the nidus volume, density and location [28]. Karlsson concluded that the probability of nidus obliteration was directly related to the radiation dose at the periphery of the arteriovenous malformation only, independent of arteriovenous malformation volume [29], and a strong radiation achieved a better obliteration of nidus however it may lead to side-effects on the patient and even resulted in re-haemorrhage.

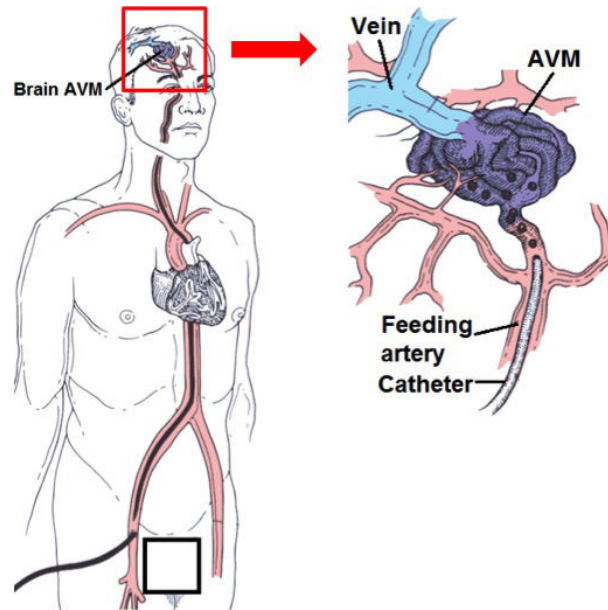


Figure 2.4: Illustration of embolization procedure. Source unknown

This method is mainly chosen when the malformation is small and located in critical location [22].

### 2.2.3 Endovascular embolization

There exists a high bleeding risk in microsurgical resection, while radiotherapy needs a large radiation dose and the AVM cannot be eliminated immediately. Embolization is usually considered as a compromise and efficient way to realize the intervention [30]. This kind of treatment is attractive because it is not very invasive, there is no open surgery and no scar. The embolization procedure is carried out by experienced practitioners and consists in navigating with a microcatheter from the groin throughout the intracranial arterial feeders until the nidus and injecting a glue-like material to occlude one or more vessels, to prevent blood flow and isolate the nidus from both the feeding arteries and draining veins (see Figure 2.4). The study of Henkes reported that embolization could achieve 10% – 95% size reduction [31], Gobin showed that embolization cured only 11% of patients with brain AVMs, but reduced the size of the lesions and thus allowed radiosurgery to cure 76% of patients [32].

Table 2.2: Recommended treatment option order of AVMs

Size	Non-critical locaton	Critical locaton
Small (< 3 cm)	1. Surgical resection	1. Stereotactic radiosurgery
	2. Stereotactic radiosurgery	2. Surgical resection
	3. Occasionally embolization	3. Embolization for more than one haemorrhage
Large (> 3 cm)	1. Embolization+Surgical resection	1. Embolization+Stereotactic radiosurgery
	2. Embolization+Stereotactic radiosurgery	2. Embolization+Surgical resection

#### 2.2.4 Treatment choice

Indeed, each intervention method has its advantages and limitations. In 2001, the American Stroke Association presented some recommendations of treatments strategies based on Spetzler Grading [33]. For example, the lesions in grade 1 were small, a single surgical excision was suggested as the first choice. For the grade 5, the lesions were large, deep, and situated in neurologically critical areas, a conservative treatment or a combined interventional strategy was more suitable such as embolization followed by microsurgery. In a review of AVMs, Fleetwood *et al.* [22] proposed the management approach based on the lesions size and location, which is described in Table 2.2. Although excellent methods have been developed and different recommendations have been suggested to assess AVMs treatment safety, the strategy remains highly individualized. Much does, and should depend on the preferences of neurosurgeons.

### 2.3 IMAGING TECHNIQUES OF BRAIN ARTERIOVENOUS MALFORMATIONS

The medical imaging techniques enable the neuroradiologists to determine the nature of potential and actual vascular problems, providing a clear and direct view to assess the vessel disease when monitoring treatment interventions.

#### 2.3.1 Angiography and digital subtraction angiography images

The first cerebral angiographic experiment was introduced by Moniz in 1927 [34], but it was until in 1953 when the angiographic method was widely used in clinical practice, when Seldinger introduced his catheterization method [35]. This technique navigates a catheter from the femoral artery through the abdominal aorta and into the carotid artery. An iodine-based intravascular contrast material is then injected into the feeding arteries. A sequence of X-ray images is recorded

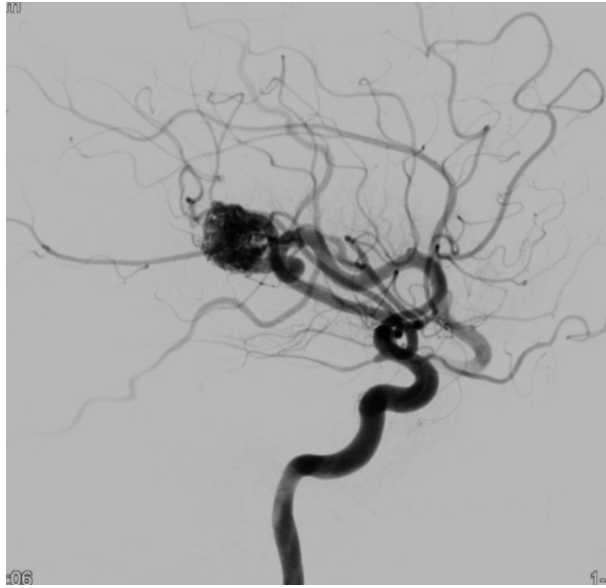


Figure 2.5: An example of brain AVM DSA image.

after a few seconds when the contrast agent has spread the whole segment of vessel network to be examined. As the contrast agent has a higher attenuation than other anatomic structures, the vessel network form can be clearly distinguished on the X-ray images.

By comparing the X-ray images with and without contrast agent, the subtraction results easily filter the blood vessel from bones, which is called *Digital Subtraction Angiography* (DSA). An example of DSA image is shown in [Figure 2.5](#). DSA involves a  $1024 \times 1024$  matrix with a quite high spatial resolution ( $0.15 \text{ mm} - 0.30 \text{ mm}$ ). With these advantages, DSA has long been considered as the gold standard for the detection of aneurysm and AVMs [36]. However, the main limitations are the requirement of the experience of the operator, the necessity of repeated injections of contrast agent and repeated radiation dose. Furthermore, the limited DSA projections are not capable to provide full three dimensional information.

### 2.3.2 *Computed tomography angiography images*

*Computed Tomography Angiography* (CTA) has been developed in the 70's. This technique uses an X-ray beam, like conventional radiology, but the photographic film is replaced by a sensor which transforms the received radiation into electric signal. The principle consists of choosing a slice plane, and to carry out multiple projections under different angles in order to know the attenuation coefficient in every point of the plane. This information is then automatically processed to ob-

tain an image where all the tissues are visible [37, 38]. In CTA imaging procedure, the contrast agent is injected into cephalic veins instead of femoral arteries, which lowers the morbidity of patients [39]. The amount of contrast agents determines, in particular, the degree of intensity of the visualized vessels. An example of a CTA image with the presence of aneurysm is shown in Figure 2.6(a).

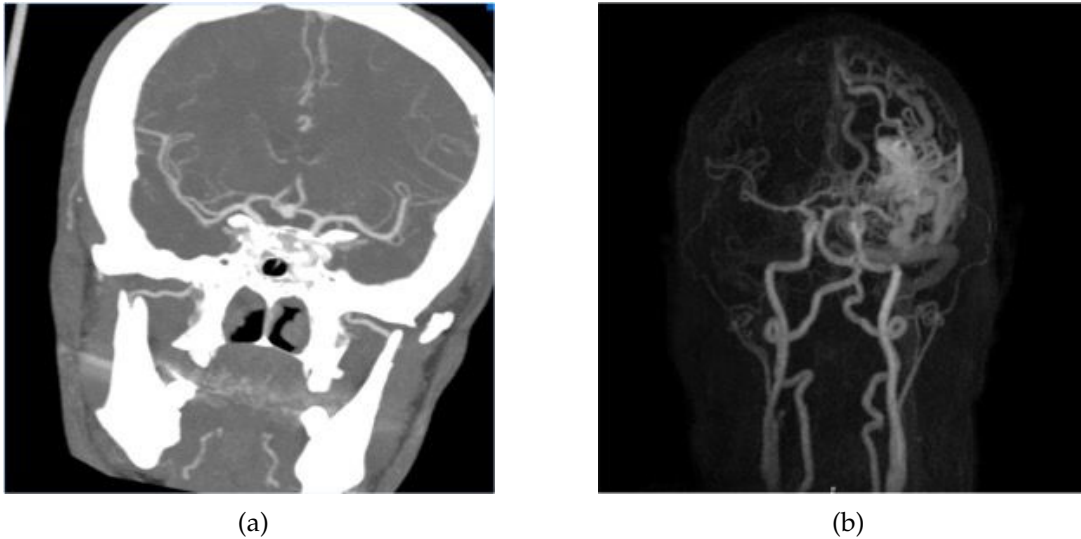


Figure 2.6: Examples of CTA (a) and MRA (b) brain images.

### 2.3.3 *Magnetic resonance angiography images*

*Magnetic Resonance Angiography* (MRA) techniques were developed in order to explore the vascular networks in a non-invasive and non-irradiating manner. These techniques rely on the magnetic properties of tissues. Indeed, a tissue modifies its magnetic state, when excited by repeated radio frequency pulse. These potentially tiny variations induce the generation of different signals which can be encoded to finally create images. The modifications of the tissues magnetic state being linked not only to the pulse, but also to the molecular structure of the tissue, the identification of magnetic properties makes it possible to accurately determine tissue composition [40].

Recent progress in MRA have led to image quality improvement, by increasing their spatial resolution, and thus the anatomic rendering. However, although these last advances emphasise the actual therapeutic usefulness of MRA, spatial resolution remains globally insufficient for lesions related to vascular structures

of a diameter smaller than 1 *mm*. In particular, these techniques still need to be improved in order to become a relevant alternative to the digital subtraction angiography, which is still the gold standard in vascular imaging.

Practically, four different techniques are generally used for the exploration of vessels: *Time-Of-Flight* (TOF) MRA, *Phase-Contrast* (PC) MRA, *Contrast-Enhanced* (CE) MRA, and more recently, *dynamic Contrast-Enhanced* (dCE, or 4D-CE) MRA, which enables a dynamic analysis of the flow.

The MRA is less invasive than CTA since it does not need any iodinated contrast material while providing cerebral vessels images. Like CTA, MRA can provide 3D images as well but they possess a lower spatial resolution than DSA and CTA. For example, a typical MRA image involves a  $256 \times 256$  matrix with pixel size 0.78 *mm*-1.25 *mm* and 0.7 *mm* - 1.6 *mm* slice thickness [41], which results in the failure of small vessel detection [42]. An example of a MRA with the presence of AVMs is illustrated in [Figure 2.6\(b\)](#).

#### 2.3.4 3D rotational angiography images

The *3D Rotational Angiography* (3DRA) imaging technique first appeared 20 years ago [43]. In recent few years it has become the reference imaging modality in neuro-vascular interventions for vessels visualization. [Figure 2.7](#) shows the Philips Allura angiographic system which is used to obtain and reconstruct 3DRA images. Like other angiographic images, the acquisition of 3DRA is carried out during angiographic experiment. The C-arm is first fixed while the patient's head being immobilized in the isocenter between the X-ray tube and the detector. Then the catheter is introduced into the carotid via the femoral route, a 28  $cm^3$  dose of the non-ionic contrast agent is injected at 4  $cm^3$ /second to enhance the vessels. With a delay of 3 seconds that allows the contrast infusion, the C-arm is rotated at 210 degrees around the isocenter in order to acquire the entire brain images. The rotation takes between 10 and 20 seconds, hundreds slices of 2D gray-scale images are transferred to the angiographic system. The collection of 2 dimensional slices images constitute a 3 dimensional image (see [Figure 2.8\(a\)](#)). An initial 3D reconstruction can be delivered a few minutes after the acquisition, based on the 3D images (see [Figure 2.8\(b\)](#)).

3DRA has been regarded as a promising imaging technique, as it offers a compromise among the conventional angiographic images. In comparison to biplanar DSA, 3DRA needs lower radiation dose [44] and less contrast dose to patients [44, 45], which is a more confident choice to conduct an embolization interven-



Figure 2.7: Philips Allura 3DRA Centron. Source: philips.dk

tion. In comparison to CTA and MRA, 3DRA provides a higher resolution:  $128^3$  to  $512^3$  pixels with voxel size of  $0.29\text{ mm}$  to  $0.49\text{ mm}$ , which is essential to visualize small vessels. The other advantages include that 3DRA imaging are more stable and accurate, with lower sensitivity to technical factors [46].

For brain AVM delineation, 3DRA was proved to be the most suitable modality [47, 48]. Specifically, 3DRA images provide the possibility to reconstruct the 3D cerebral vascular network. This permits having a direct volumetric and geometric assessment of intracranial AVMs. Recent studies demonstrated that 3DRA imaging technique is more preferable than CTA and MRA for determining the angio-architecture of brain AVM [3]. With 3DRA, the volumetric estimation is more accurate and precise. The extraction of arterial feeders and draining veins can be less difficult. Some improvements can be shown for the 3D conformation and vascular densities of nidus. Moreover, 3DRA images have greater chance to detect weakness points such as aneurysms and venous lesions [3]. Nowadays, it is widely used during the planning of endovascular procedures, that allows characterizing the feeding arteries of nidus and can also facilitate the multiple hyper selective catheterization [49, 50].

In clinical practice, different modalities provide the neurologists and surgeons a full insight to the vascular structure in diagnosis and treatment phase. For example, Weiler *et al.* suggested that the multimodal visualization allows a neurosurgeon to intuitively grasp the three-dimensional architecture of an AVM nidus, along with its extent and spatial relation to functionally critical structures [51].

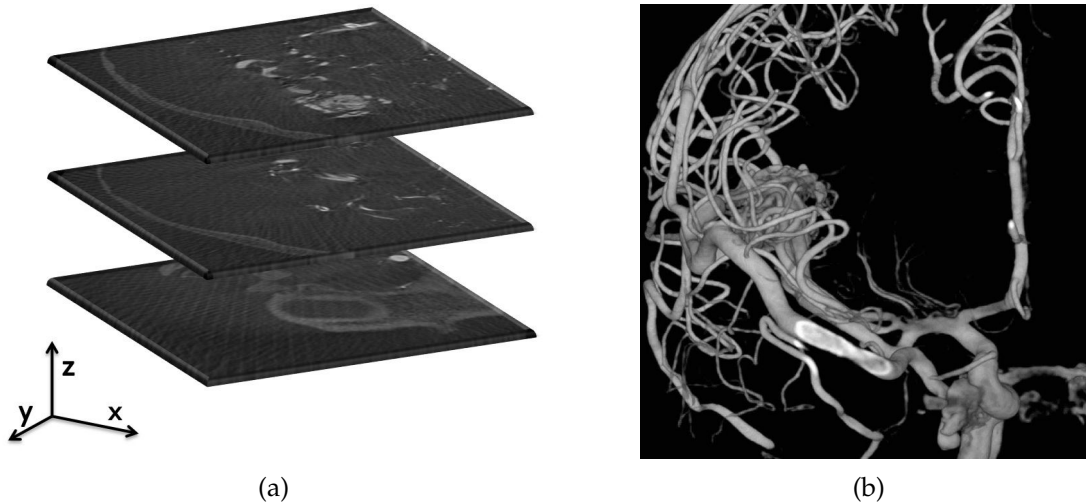


Figure 2.8: 3DRA images and its reconstruction image. (a) Three slices of 3DRA image obtained from Philips Allura Centron. (b) Reconstruction result from Philips Allura Station.

For example, in [Figure 2.9](#), DSA and MRA are combined to delineate the nidus size and position.

#### 2.4 CONCLUSION

In this chapter, we gave a brief introduction about the brain arteriovenous malformations, the main treatments and relative imaging techniques for diagnosis and neuroradiological interventions. A successful embolization intervention management is challenging since it should be carefully prepared by experienced neuroradiologists with the analyses of different imaging modalities like MRA, CTA, 3DRA and DSA. We have highlighted that the endovascular embolization is an important intervention method for the treatment of brain AVMs. To perform this intervention, an accurate description of cerebral vascular network is of great importance, from which the neuroradiologists could identify the principal feeders supplying the nidus and determine the navigation paths.

Among all the current imaging modalities, 3DRA remains a promising imaging technique having numerous advantages for brain AVMs analyses comparing to other conventional modalities. In this thesis, we elaborate our research on 3DRA images in order to offer neuroradiologists an accurate description of the cerebral vascular network and help them in embolization planning.

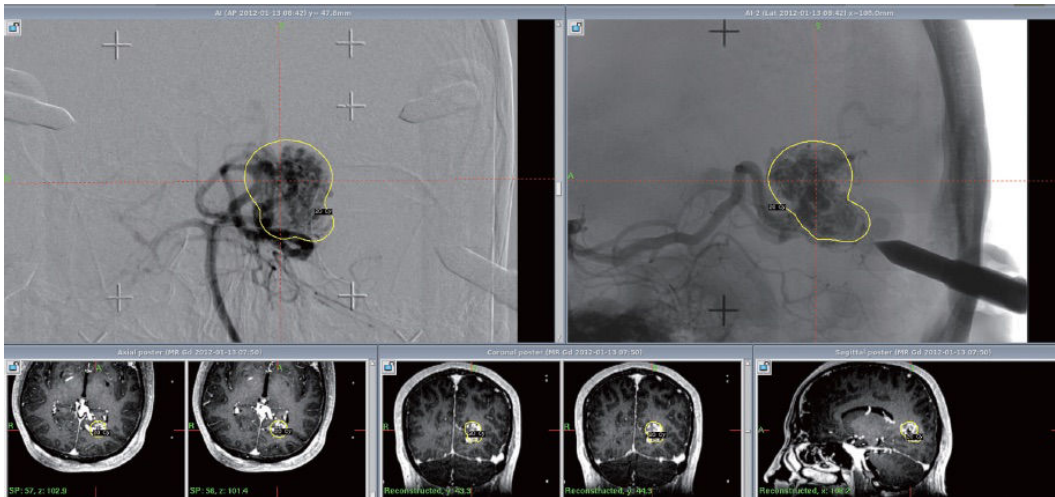


Figure 2.9: AVMs treatment plan using DSA and MRA [52].



## SEGMENTATION AND VISUALIZATION OF CEREBRAL VASCULAR NETWORK

---

### Contents

---

3.1	Introduction . . . . .	23
3.2	Classical methods and techniques for vessels segmentation . . . . .	24
3.2.1	Thresholding . . . . .	25
3.2.2	Statistical model analysis . . . . .	26
3.2.3	Deformable models . . . . .	27
3.2.4	Pattern recognition . . . . .	29
3.2.5	Region growing . . . . .	31
3.2.6	Mathematical morphology approaches . . . . .	35
3.3	Specific models based on vessel features . . . . .	37
3.3.1	Tube-like multi-scale filters . . . . .	37
3.3.2	Geometrical models . . . . .	39
3.3.3	Discussion . . . . .	40
3.4	Vessel reconstruction and 3D visualization . . . . .	42
3.4.1	Vessel reconstruction . . . . .	42
3.4.2	Vessel visualization . . . . .	42
3.5	Contributions . . . . .	47
3.5.1	2D slice-by-slice segmentation . . . . .	48
3.5.2	3D region growing segmentation . . . . .	52
3.5.3	3D vessels reconstruction . . . . .	57
3.5.4	Separation of the arteries, nidus and veins . . . . .	57
3.6	Results . . . . .	60
3.7	Conclusion . . . . .	74

---



### 3.1 INTRODUCTION

Vascular diseases are one of the most important health problems in the world. The growing number of patients suffering from coronary diseases, cerebral stroke and congenital vessel malformations lead to numerous research based on vascular imaging. Computational diagnosis assistance and aid for treatment planning are thus highly desirable.

In computer vision, image segmentation consists in assigning the same label to a set of neighbouring pixels that share one or several properties such as luminance, chrominance, texture, *etc.* It is typically employed to locate objects and regions with their boundaries. The segmentation of vascular structure is essential to the clinical analysis of vascular pathologies. It is usually required as the key step toward the accurate visualization, diagnosis and quantification of vascular structure. The following applications of segmented vascular structures are:

- Geometric modelling
- Multimodal registration
- Anatomical labelling
- Statistical analysis
- Quantitative measures

However, cerebral vessels are complex objects with different shape, size, tree organization and overlapping. Consequently, the extraction of the vascular network is not an easy task. The choice of the most suitable segmentation method depends on the imaging modality and on the intended application [53–55].

The first part of this work is devoted to the study of the different approaches used in segmentation of the vessels. In [Section 3.2](#) we present a state-of-the-art of vascular segmentation methods. Our interest is focused on the segmentation of cerebral vessels but the cited works are not limited to this domain. Indeed, the segmentation of the different vascular networks of the human body (cardiac, retinal, pulmonary, liver or ocular, for instance) is confronted with very similar problems.

We classify these methods into six categories, based on the following segmentation approach: 1) thresholding, 2) statistical model analysis, 3) deformable models, 4) pattern recognition, 5) region growing and 6) mathematical morphology.

In [Section 3.3](#), segmentation approaches exploiting a vessel model are presented. Afterwards, the main visualization methods are described in [Section 3.4](#).

Our approach to the segmentation of cerebral vessels in 3DRA images is presented in [Section 3.5](#). Two segmentation methods are proposed: a 2D slice by slice segmentation approach followed by a robust vessels tracking algorithm and a 3D region growing based segmentation method.

As post-processing step, the segmented vascular network is separated into three entities: arterial network, draining veins and nidus. The segmentation results are analyzed and discussed in [Section 3.6](#).

### 3.2 CLASSICAL METHODS AND TECHNIQUES FOR VESSELS SEGMENTATION

Several works were dedicated to the development of vessels extraction algorithms and techniques. Kirbas [\[54\]](#) proposed to classify the existing algorithms and techniques into six categories:

1. pattern recognition techniques
2. model-based approaches
3. tracking-based approaches
4. artificial intelligence
5. neural networks
6. tube-like objects determination

Lesage *et al.* [\[55\]](#) discussed the segmentation of angiographic images from three aspects:

1. the employed vessel models
2. the existing vessel-specific features
3. the extraction schemes

Both authors focused on the segmentation methods regardless of applications (cerebral, retinal, cardiac, pulmonary, *etc.*) or modalities (DSA, MRA, CTA, MIP, 2D or 3D *etc.*), while some reviews studied the work for one particular application or modality. For example, Suri *et al.* [\[56\]](#) focused on the pre-filtering techniques and segmentation algorithms from MRA images. Felkel *et al.* [\[57\]](#) dedicated to

the vessels segmentation and tracking algorithms in CTA datasets . A review of segmentation method for coronary and retinal vessels are separately presented in [58] and [59].

In this section, we have combined the two reviews given by Kirbas [54] and Lesage [55]. Moreover, we place great emphasis on some very recent works of three dimensional vascular segmentation and notably on the segmentation of 3DRA images.

### 3.2.1 Thresholding

Thresholding is a pixel-based procedure used for segmentation. It consists in considering current pixel disregarding its surroundings. If the assignment of pixel intensities is well known and constant for a type of tissue, static thresholding is applicable.

Globally adaptive thresholds result from analyzing each image entirely to choose a specific threshold exclusively. The principle of automated adaptive thresholding algorithms were discussed in [60], where six approaches were mentioned: iso-data, Otsu, minimum error, pun, moment-preserving and fuzzy. The well-known method of Otsu determines the optimal threshold from the histogram such that two resulting classes minimize the intra-class variance.

In cerebral angiographic images, the proportion of vascular structure is nearly 1% of the total volume, which is far below the other anatomical structures [61]. The image contrast between vascular objects and background is highly unbalanced. In the image histogram, the valley between the object peak and background peak is not deep and evident. For these reasons, the optimal threshold may not be precise if the Otsu method is directly applied. To deal with the problem, Zhang *et al.* [62] proposed to divide the MRA image into sub-blocks and determine the local thresholds with Otsu algorithm to extract vessels.

Kim *et al.* [63] used local adaptive thresholding with connectivity-based information to segment the carotid artery in 3D MRA images. For each slice, a local threshold was calculated from the histogram of a *Region Of Interest* (ROI) that became the new ROI of the next slice.

In a more recent work, Wang *et al.* [64] presented a threshold segmentation algorithm for the automatic extraction and volumetric quantification of cerebral vessels from brain MRA images. This algorithm determined the appropriate global threshold value by comparing the Gaussian and Unilateral Normal distributions. The *Probability Density Functions* (PDF) of the two statistical distributions are re-

spectively expressed in Equation 3.1 and Equation 3.2. The appropriate global threshold value  $x_i$  is determined when the condition Equation 3.3 is met where  $\omega \geq 2$ .

$$p_{Normal}(x_i|\mu, \sigma) = \frac{1}{\sqrt{2\pi}\sigma} \exp\left(-\frac{(x-\mu)^2}{2\sigma^2}\right) \quad (3.1)$$

$$p_{Gumbel}(x_i|\mu, \sigma) = \frac{1}{\sigma} \exp\left(-\frac{x-\mu}{\sigma} - \exp\left(-\frac{x-\mu}{\sigma}\right)\right) \quad (3.2)$$

$$p_{Gumbel}(x_i) = \omega \times p_{Normal}(x_i) \quad (3.3)$$

Some authors developed gradient-based algorithms, which compared the gradient of voxels with a global or local threshold. Wilkinson *et al.* [65] developed a new multi-scale moving-window method for local adaptive thresholding based on the *Robust Automatic Threshold Selection* (RATS) algorithm [66]. The proposed version was applied for the segmentation of cerebral vessels from MRA images and showed results dealing better with varying background and noise problems than earlier versions of RATS.

An extension of the RATS algorithm was proposed by Boegel *et al.* [67]. The threshold estimation condition was completed and the results of global/local adaptive thresholds were compared. With locally adaptive threshold method, the segmentation is closer to the ground truth. The main limitations of the RATS algorithm are the selection and parameters optimization, which strongly influence the segmentation result.

### 3.2.2 Statistical model analysis

The vascular segmentation with statistical models generally rely on the analysis of intensity distribution. It is usually assumed that the intensity distribution of an image is a finite mixture of statistical model distributions, where each anatomical structure can be approximated by a precise model. To facilitate the analysis, the number of the tissue families in the image has to be determined. Once the distribution number is defined, it is then possible to apply the *Expectation Maximization* (EM) and thus estimate the unknown parameters (weight, mean and standard de-

viation) of the distribution with an iteration procedure. Finally a global threshold value is selected to perform the segmentation based on classification rules.

Due to the variability of acquisitions and image modalities, the mixture distribution models are difficult to adopt on cerebral vascular images. Some mixture distribution models have been proposed to present the cerebral vascular distributions. Gan *et al.* [61] proposed the *Finite Mixture Model* (FMM) of Gaussian distributions from 3DRA and MIP images. Other authors suggested that sole Gaussian distribution can not totally fit the real distributions. Chuang *et al.* [68] applied a *Maxwell Uniform* (MU) / *Maxwell Gaussian Uniform* (MGU) mixture model to represent the distribution from PC-MRA images, Gao *et al.* [69] used Gaussian and Rayleigh mixture model to segment the cerebral vessels from TOF-MRA images. Wang *et al.* [64] adopted Gaussian and Gumbel distributions from MRA images, which we have previously presented in [Section 3.2.1](#).

The strengths and weaknesses of statistical methods globally inherit from the EM algorithm. The segmentation results heavily depend on the distribution models, the iteration procedure of EM may be time-consuming, which is determined by the initialisation. Moreover, attention must be paid to the convergence of the EM algorithm that is not always guaranteed, which requires a termination condition, for instance by a maximal number of iterations.

### 3.2.3 Deformable models

The Geodesic Active Contour was first introduced in 1997 [70]. Derived from a shape and a position, the initial contour is deformed until stopped on the frontiers of the structures to be segmented. Generally, the evolution of the contour is governed by 1) *internal forces*, which are defined within the initial object to preserve the geometry properties such as smoothness and regularity, and 2) *external forces*, which are related to image features such as intensity, homogeneity and gradient.

The deformable models are usually classified into two main categories: parametric and geometric models. On one hand parametric models have an explicit representation of the contours, which allows directly interacting and controlling the model. On the other hand, geometric models have an implicit representation with the level set of a higher dimensional scalar function. Unlike parametric models, the *level set* can better adapt to the object topology variation, such as splitting or merging during the deformation procedure.

Hernandez *et al.* [71] presented an automatic method using *Geodesic Active Regions* (GAR) for the segmentation of cerebral vascular structures. This method was

applied to segment aneurysms in 3DRA and CTA images. The minimized energy functional incorporates statistical region-based information and the process was implemented in a general framework suited to the segmentation of other organs on different imaging modalities.

Sanz-Requena *et al.* [72] also applied the GAR method in order to extract vessel contours and evaluate the vessel pathologies, from *IntraVascular UltraSound* (IVUS) imaging along with X-ray coronary angiography. Particularly, the *Gradient Vector Flow* (GVF) was considered as external force in this model. Based on the obtained contours with the GAR method, a knowledge-based approach was combined to estimate different vascular areas in IVUS imaging, such as lumen, intima and plaque.

Firouzian *et al.* [73] implemented a level set based approach to detect and segment aneurysm from CTA images. From a seed center selected inside the aneurysm, the initial zero level curve evolved toward the real contour, by taking into account the external forces derived from intensity, gradient magnitude and intensity variance. A pre-defined ROI was required to separate the aneurysm from adjacent vessels and connected bones.

Wu *et al.* [74] proposed to use level set for the extraction of different vascular trees in CTA images, such as cerebral, liver and aorta trees. Three kinds of forces were mentioned in their work: an advection force to push the contours toward the real vascular edges, a smoothing force to minimize the curvature of the contours and a balloon force to expand the contour within the vascular regions. A circle or ellipse fitting method was suggested to adjust the segmented contour for post processing of the cross sections.

Li *et al.* [75] introduced a new formulation of the level set method, which enabled the segmentation of the contours of regions from an initial area and automatically maintain the regularity of contours during the iterations of the deformation. This method eliminates the need to reset and proves to be more accurate and efficient. We tested this algorithm to extract the vascular structures from our 3DRA images. The results are presented in [Section 3.6](#).

Chang *et al.* [76] suggested a charged fluid model to extract brain vessels network and aneurysm in 3DRA images. In his model, the deformable contour obeys to electrostatic laws. From a pre-defined region of interest, electric forces guide the evolution of deformable contour which is governed by Poisson equation. An illustration of the evolution of the 3D charged fluid model is shown in [Figure 3.1](#). Compared to the level set segmentation method, this approach is more efficient to segment vessels images corrupted by blurring or high frequency noise.

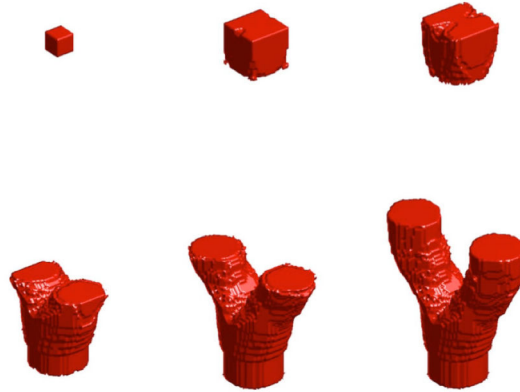


Figure 3.1: Illustration of the evolution of the 3D charged fluid model [76].

The major advantages of the level set are the topological adaptivity, the sub-pixelwise precision and the noise robustness. By incorporating prior shape information, they permit dealing with the boundary gaps problems. However, most deformable models are sensitive to initialization, especially the parametric models and often require an interaction with the user. The evolution of deformation can be a costly process, when the final object borders are not far from the initial ones. Integrated object features and forces in powerful optimization schemes help overcoming these problems.

#### 3.2.4 Pattern recognition

The pattern recognition is a branch of data mining and machine learning that analyses the pattern identification and processing. In many cases, the recognition of one instance is done by matching the most likely class among a set of samples. A method is regarded as *supervised learning* if each sample has been assigned a label in the training step, for instance the *K-Nearest Neighbour* (KNN) and *Support Vector Machines* (SVM). On the contrary, some methods are called *unsupervised learning* when the data patterns are unlabelled during the training step. The techniques of unsupervised learning include expectation maximization and clustering approaches (e.g. K-means and mixture models).

The *Support Vector Machines* (SVM) are techniques inspired from statistical learning theory. The goal of SVM is to find a limit to separate data and maximize the distance between two classes.

Caldairou *et al.* [77] introduced a segmentation method of cerebral vascular network from MRA images. This method combines SVM and connected component approach and follows two stages: supervised learning and classification. The supervised learning is performed by collecting all the nodes of sub-images, labelling them (vessels or artifacts) with a segmentation reference and thus create a SVM model. To achieve the classification, the images to segment are cut into cubes to construct trees of connected components. Each vascular tree is pruned by identifying its nodes with the obtained SVM model. The segmentation result is then constructed from these pruned trees.

Bogunovic *et al.* [78] proposed a SVM based approach to automatically identify the ICA bifurcation from 3DRA images. After segmentation step using GAR algorithm, the topology of the artery tree is constructed by computing the center-lines. This topology presentation allows the bifurcation study, the identification of parent vessel and branches of each bifurcation and the quantification of geometric features (bifurcation origin, mean vessel radius). A machine learning based approach is then applied, where a classifier has been trained to detect the ICA terminal bifurcation.

Vermandel *et al.* [79] used fuzzy logic theory to produce the segmentation of 3D vascular structures with MRA and MIP images. The authors introduced the assumption of fuzzy area defined from an initial contour of vascular region. The membership degree of each voxel in the fuzzy area was obtained by considering the distribution of the gray levels, in order to determine whether this voxel belongs to the vascular structure or not. The results are satisfactory although some vessels have disconnected branches which requires a post-processing step.

Forkert *et al.* [80, 81] also presented a fuzzy-based algorithm to perform the vessel enhancement, segmentation and structure separation from TOF-MRA images. The general process is illustrated in [Figure 3.2](#). A histogram matching technique and skull-stripping for TOF images approach were applied in the pre-processing. Afterwards, the vesselness image and maximum parameter image were separately calculated with corresponding filter. An initial segmentation was obtained by combining all these different images with fuzzy-logic fusion. The results were finally optimized with a threshold and level set segmentation.

Some applications with EM and mixture models approaches are introduced in [Section 3.2.2](#).

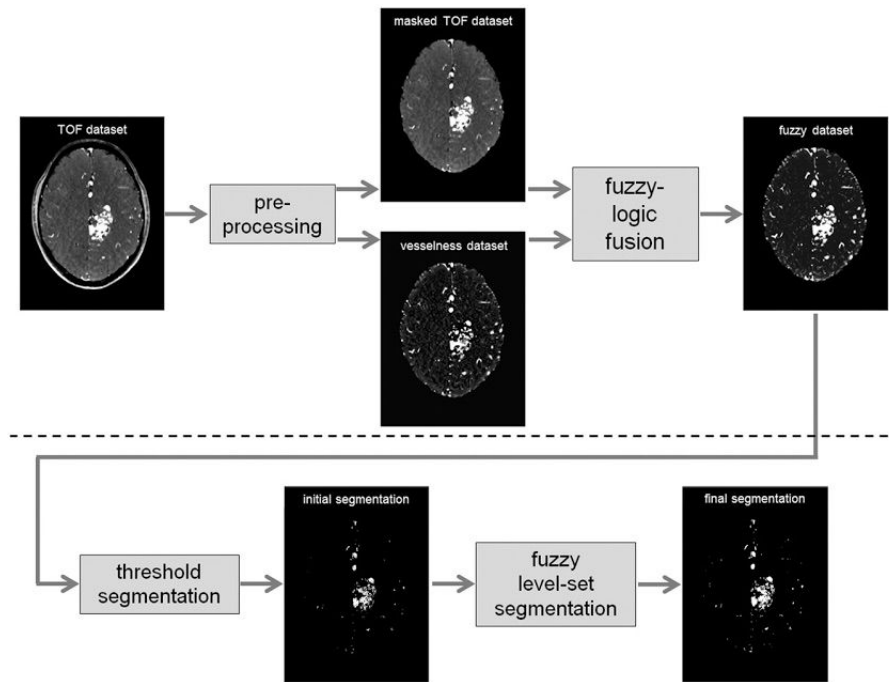


Figure 3.2: Illustration of fuzzy-based segmentation [80].

### 3.2.5 Region growing

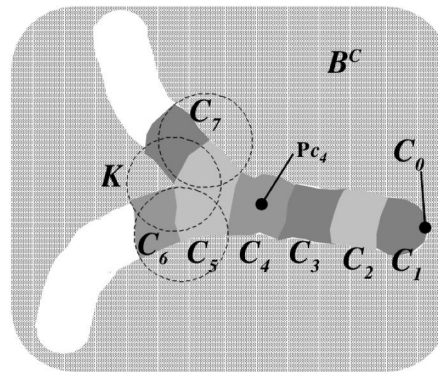
Starting from selected seeds belonging to the structures to be extracted, the *region growing* technique consists in incrementally including neighboring pixels/ voxels based on a pre-defined criterion. The segmentation result relies on two important elements: the initialization of the seed points and the inclusion criterion.

Usually, in case of cerebral vessel segmentation, seed points are defined at the root of the vascular tree. These seeds can be selected interactively or located automatically. The inclusion criterion is usually based on the spatial proximity and the homogeneity of adjacent pixels [82]. Thanks to the injected contrast agent, the intensity of vascular regions is brighter and more homogeneous than the surrounding background structures [83]. This allows defining robust inclusion criteria for pixels or voxels belonging to the blood vessels.

Due to existing noise or intensity variability on the image, some post-processing procedures such as filtering are sometimes necessary to guarantee the segmentation accuracy. In the following, we present some works combining the region growing segmentation with other processes in the aim of accurately segmenting the vessels from medical images.

### 3.2.5.1 Shape-based region growing model

Early in 1998, Masutani *et al.* [84] has introduced the concept of shape-based region growing model. This model is shown in Figure 3.3. In the proposed algorithm, a simple thresholding is first performed to obtain an initial binary shape. The seed is then manually defined and the cluster grows generation by generation with mathematical morphological elements. The propagation iterates with a closing and smoothing process to fill the holes in the segmentation result. Owing to chosen structuring elements, the propagation enables detecting the bifurcations and the disconnections of vessel segments.



$C_i$  :  $i$ -th cluster

$P_{c_i}$  : cluster's center of gravity

Figure 3.3: Shape-based region growing [84]

Similar to the work of Masutani, Sekiguchi *et al.* [85] proposed a branch based region growing strategy for cerebral vascular segmentation in MRA images. In the first step, the connectivity of the new neighbour points is verified in each growing cycle. The branch bifurcations are identified if the new added points were not connected. Then the region grows to only one branch until it reaches the extremity. All the points in this branch are recorded and the propagation continues toward the other branch of the bifurcation. The extraction order can be seen in Figure 3.4. This method enables a direct analysis of vascular network branch by branch.

Jiang *et al.* [86] has recently developed the work of Sekiguchi *et al.* [85]. In their approach, a vessel enhancement based on Hessian matrix was applied and followed by spectrum analysis. An initial detection of vascular structure was thus obtained. The point that possessed the highest gray value was picked as the seed for the following branch-based region growing method process [85]. The proposed approach achieved good results experimented on 2D retinal vascular

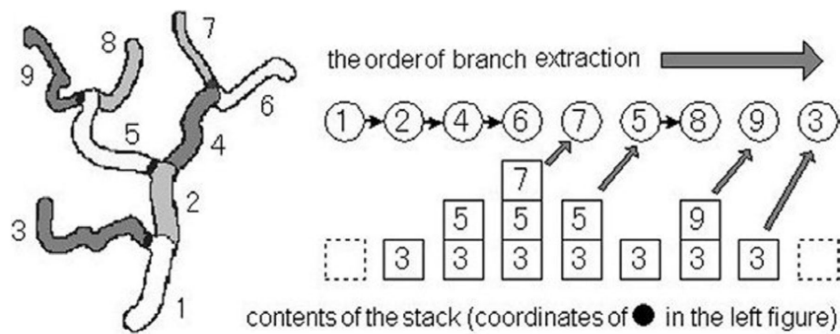


Figure 3.4: Branch-based region growing [85]

images. As for 3D CT liver images, the tiny bifurcation vessels are not clearly segmented.

### 3.2.5.2 Classical region growing model

Boskamp *et al.* [87] suggested the classical region growing approach to extract vessels in 3D CTA and MRA images. Their criterion was based on a threshold value, that all neighboring voxels are included in the region if their gray value is above this threshold. The threshold was determined by analyzing the threshold-volume diagram. A post-processing was carried out by pre-masking method to isolate the vessel network from adjacent, interfering structures (bones and skull for instance). The mask boundary was delineated by watershed approach from two markers located in the vessels and interfering structures. The proposed method has been tested and validated for single arteries such as intracranial, coronary and abdominal arteries. The principle limitation is the requirement of a pre-masking, which is hard to be determined for complex vascular network.

### 3.2.5.3 ATLAS and region growing

Passat *et al.* [88] applied the region growing on a brain atlas created from MRA images. This atlas was constructed by registering several segmentation results of the same image. In an attempt to store vascular anatomical knowledge, the atlas divided the initial image into four principal regions: arteries, veins, both arterial and venous vessels, or no vascular structures. The region growing was used separately with adaptive threshold values to build the arterial and venous trees. To preserve the topology of the vessel trees, only simple points were allowed to

be added in the growing process. The results confirmed that atlas-based region growing could efficiently improve the segmentation result.

#### 3.2.5.4 *Filtering based region growing*

Cao *et al.* [89] and Chen *et al.* [90] suggested a *Minimum Path based Region Growing* (MP-RG) method to segment 3D coronary vessels in CTA images. This algorithm consists of carrying out the region growing by searching the path that minimizes a pre-defined energy function. The potential function was built based on the convexity information of orientated 1D vessel profiles.

To extract coronary tree from 2D angiogram images, Wang *et al.* [91] and Li *et al.* [92] have proposed a similar algorithm. Wang used a multi-scale filter based on Hessian matrix while Li chose the *vesselness filter* in [93] as a pre-process tool before the region growing. With the enhancing filters, the small vessels are particularly enhanced and more vessels can be detected. Very recently, Kulathilake *et al.* [94] presented another approach to deal with the same application based on region growing. Median-filtering and normalization operation are firstly employed to enhance the image quality. The novelty of their work was the creation of a mask image which depicted the possible vascular structure regions. The mask image was obtained by iteratively comparing two consecutive image frames, with the assumption that, in the angiograms, the vessels are slightly moving while the background structures remain motionless. The introduced mask image allowed minimizing the segmentation of non-vessel regions.

Almiani *et al.* [95] described a modified region growing based technique to extract vessels in MRA images. First, in order to detect isolated points, image enhancement methods were applied by a "power-law" transformation and a specific filtering. After having selected a point on the center of a ROI, the average of its pixel intensity was calculated and an homogeneity criterion was deduced from the difference between the intensity of the center point and the average. The region growing was performed and a finally filling operation was conducted to ensure the segmentation continuity.

Recently, Orkisz *et al.* [96] proposed to segment pulmonary vascular trees from CT images. In this work, a delineation of pulmonary vessel tree was first carried out with adaptive multi-scale morphological operations. Then a vessel-enhancement process was performed by vesselness functions. The maximum intensity pixel in the vesselness image was selected as the seed point to launch the *Variational Region Growing* (VRG). The proposed algorithm is suitable for the in-



Figure 3.5: From left to right: original image and segmentation resulting from an iterative adding of pixels belonging to the neighbourhood of an initial seed [98].

tended application. It succeeded to segment most vessel trees around bronchial walls.

#### 3.2.5.5 Hybrid region growing and level set

Chang *et al.* [41] proposed an algorithm for cerebral aneurysm segmentation in 3DRA images. They applied the 2D region growing algorithm followed by 3D deformable contour based on a charged fluid model. Starting from one chosen seed, the region growing permitted obtaining an initial 2D segmentation with a specified homogeneity criterion. The segmentation result was used to compute the mass center, the bound and the size of the vessel. Based on all the information, the 3D deformable contour model was then processed to give accurate segmentation results.

Martinez *et al.* [97] presented an hybrid level set and region growing algorithm to segment the thoracic aorta from CTA images. The rather simple shape of the thoracic aorta enabled using the *Hough-transformation* to locate the ellipse-like vascular region on the first slice of image. The region center was then chosen as the seed point to segment the 3D image volume. The level set was applied after the region growing in order to obtain a precise segmentation result.

As a brief conclusion, the region-growing based segmentation is a classical method that is widely used for the extraction of vessels, particularly coronary, lung and retinal vessels. Few works have been suggested to extract cerebral vascular network using the region growing method, even less for the 3DRA images [41]. Our contributions for the segmentation of the cerebral vascular network from 3DRA images are presented in [Section 3.5](#).

#### 3.2.6 Mathematical morphology approaches

Mathematical morphology provides a set of mathematical tools for creating particularly useful operators to filter, segment and quantify images according to their

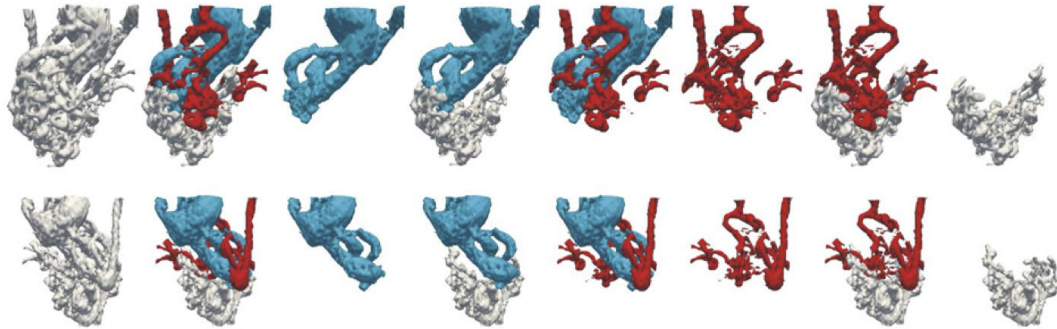


Figure 3.6: The AVM is “broken up” into its most important parts: draining vein in blue, feeding arteries in red and nidus in white. The delineation is done by radius 3D calculation in the segmented AVM data and thresholded at different radius size [101].

intensity and shape. The simplest tools are those based on thresholding. Other tools can be built from the dilation and erosion. These include the opening, closing or more advanced methods such as watershed segmentation and *hit-or-miss* transformation. These morphological operators are commonly constructed with a *Structuring Element* (SE) of a certain shape and size.

Passat contributed to the state of the art with mathematical morphology based segmentation method of brain vascular structures in 3D MRA images. He proposed four useful methods. Two of them are devoted to the segmentation of global cerebral vascular structures: combination of region growing with an adaptive thresholding and hit-or-miss in grayscale method [99]. The other two methods are dedicated to the segmentation of local vascular structures of the brain: with watershed and the topological reconstruction based on homotopy reduction tools [100].

Babin *et al.* [101, 102] presented a novel method of 3D angiography AVM segmentation suitable even for low resolution images and high variability of pixel intensity. This method is based on a generalization of morphological profiles [103, 104] that is carried out with varying differential structuring elements, which are especially adapted for different size and contrast vessels. This automatic method also give good results in segmenting the inner structure of the AVM, clearly delineating between feeding arteries, draining vein and nidus (see Figure 3.6).

Dufour *et al.* [105] proposed a complete vessel filtering and segmentation method, relying on mathematical morphology. For filtering, the variant mathematical morphology combined with differential vessel descriptors [93] was used

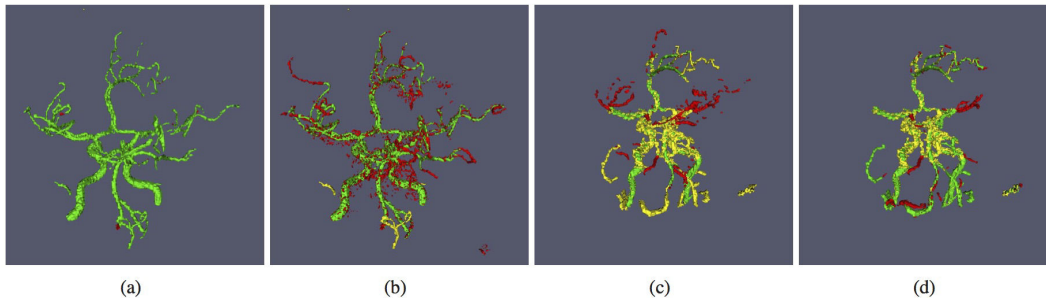


Figure 3.7: Segmentation results in an intra-patient case [105]. In green: true positives. In yellow: false negatives. In red: false positives. (a) TOF MRA (TOF 1) segmentation using the TOF MRA ground-truth as example. (b) TOF MRA segmentation using the PC MRA ground-truth as example. (c) PC MRA (PC 1) segmentation using the TOF MRA ground-truth as example. (d) PC MRA segmentation using the PC MRA ground-truth as example.

[106]. For segmentation, connected filtering were carried out to modelize characteristics of a grey-level image by using its binary level set obtained from a sequence of thresholding (see Figure 3.7). Moreover, the method requires a little of user interaction and a pre-segmented image that has to be registered with the image to segment. This method is particularly useful in case of cerebral atlas creation and for atlas-based segmentation.

### 3.3 SPECIFIC MODELS BASED ON VESSEL FEATURES

Passat *et al.* [100] developed a segmentation approach using a geometric model. The first step is the development of a model consisting of voxels that have a probability of belonging to the vessels. Then, this model is repositioned on the examination to be segmented in successive transformations. Only voxels that have a probability strictly greater than zero are taken into account for the ultimate adaptive thresholding step. Although this type of model is attractive, it should be noted that as it is purely geometric, it has difficulty taking into account the very diverse pathological expressions.

#### 3.3.1 Tube-like multi-scale filters

From a geometric point of view, the vascular structures in 3D volumes can be considered as tube-like objects. In principle, these tubular objects are elongated in one main direction (which varies) and are thin in the other two perpendicular

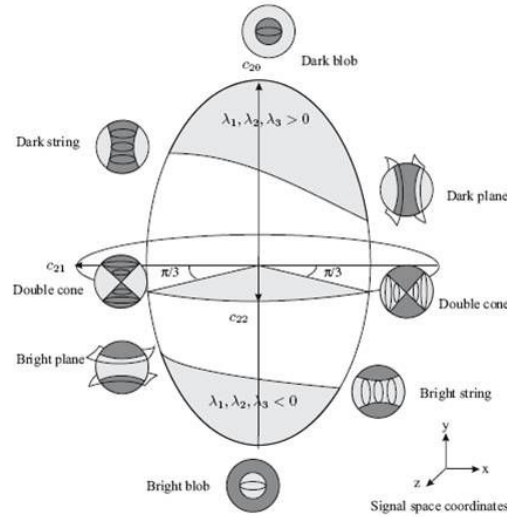


Figure 3.8: Hessian eigenvalues shape-space.  $\lambda_1, \lambda_2, \lambda_3$  are the eigenvalues of the Hessian matrix [107].

directions [108]. To capture this feature, several filters were introduced to enhance the tubular structures (vessels) while attenuating the background. Here we highlight the Hessian filtering method proposed by Frangi [93].

The *Hessian matrix* is calculated when one image is convoluted with second-order Gaussian derivatives. The eigenvectors of multiscale Hessian matrices and their associated eigenvalues are then analysed, to capture different shapes such as blob, thin planar and tubular structures. For the vessel points, the second derivatives are expected to be close to 0 in the direction of the axis, and strongly negative in the plane perpendicular to this axis. Consequently, the three eigenvalues ( $|\lambda_1| \leq |\lambda_2| \leq |\lambda_3|$ ) of the Hessian matrix should meet the following conditions:  $\lambda_3 \approx \lambda_2 \ll \lambda_1 \approx 0$ , as illustrated in Figure 3.8. To cope with different vessel diameters, multi-scales techniques are applied to separately determine the maximum response.

Sato *et al.* [109] proposed a filter which was based on a combination of the eigenvalues of 3D Hessian matrix. Such combinations were designed by taking the maximum among single-filter response. This so-called *vesselness function* was widely used to detect and enhance line-shape structure.

Krissian *et al.* [110] applied multi-scale approach for the detection and reconstruction of cerebral vessels in 3DRA images. He also designed a cylindrical model whose intensity varied according to a Gaussian distribution. The response at a given scale was obtained by integrating the first derivative of the intensity in the radial direction along a circle in the cross section of vessel. After normal-

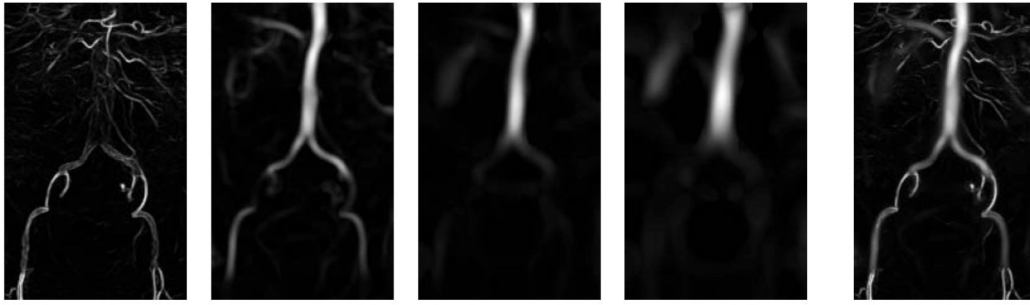


Figure 3.9: From left to right: (a) the original MRA image, (b,c,d) separate images depicting vessels of various widths, obtained using four enhancement filters of increasing scales, (e) the final image [93].

ization of the model, the authors deduced the relationship between the radius of a vessel and the scale at which it is detected. The multi-scale response thus allows extracting the skeleton of vessels and rebuilding the network from axes and associated rays.

The drawbacks of Hessian filtering are time-consuming and failure of detecting bifurcations. Orłowski and Orkisz [111] proposed a method to ameliorate the calculate efficiency of multi-filtering. By checking the sign of the matrix trace (the sum of the elements on its diagonal), some voxels unlikely belonging to vessels are discarded, prior to the calculation of the Hessian eigenvalues. This optimization can save half computation time. To eliminate the interference of soft tissues similar shape, Yang [112] added an image gray-scale factor to enhance the vascular structure and attenuate other tissues. The results have been experimented on brain MRA and CTA data.

### 3.3.2 Geometrical models

#### 3.3.2.1 Centerline models

Regardless of complex 3D surface information, a skeleton-based assumption is that the vessel tree can be simply reduced to a 1D curve, defined as *centerlines*. Some methods require extracting the centerlines from segmentation, which we consider as a thinning technique (detailed in Section 4.2.2). Other methods permit obtaining the centerline information and further constrain an accurate segmentation of the contours. Among the second type of centerline extraction algorithm, most of them consist of semi-automatic approaches, that track the center point along the vessel from a root point. The tracking procedure includes two steps: prediction and correction.

The prediction of successive point positions in the centerline is basically performed with the evaluation of the vessel direction. The methods of direction estimation include Hessian-based techniques [113], moments of inertia [114] and gradient vector distribution [115].

The predicted center position is corrected in the second step. The most common method is to segment the 2D cross section around the prediction and refine the mass center of the cross section region [116].

Other approaches have been developed when the starting and arrival points of the vessel are known. For example, the minimal path techniques (Dijkstra-like path) are widely used to extract the vascular skeleton [117, 118]. Besides, Lacoste *et al.* [119] suggested adopting the Markov marked point processes for the segmentation of coronary arteries from 2D angiograms. However, his method is limited to 2D image analysis.

### 3.3.2.2 3D generalized cylinder models

Generalized cylinder models are used to represent cylindrical objects. This consists of 2D cross-sectional contours sweeping along the centerline which is a space curve. Classical cross-sectional forms include circles, ellipses and parametric curves.

Flasque *et al.* [120] proposed a tubular structures detection method applied on 3D angiographic images of cerebral arteries. Their model consisted of a cylinder center line and a set of 2D sections. A non-intensity geometric model was constructed to locate the centerline with a high accuracy.

Kumar *et al.* [121] described an algorithm of vessel segmentation and centerline extraction. In this algorithm, the tracking direction is obtained with the analysis of Hessian matrix and the two-dimensional segmentation is realised by applying a Canny edge detection filter.

The centerline and cylinder models are based on two main assumptions: vessels have a very good contrast and are connected by a rather simple tree structure. For this reason, most contributions have been made on MIP and angiogram images.

### 3.3.3 Discussion

From all the works mentioned above, we have summarized several points below. First of all, only few work have been devoted for the segmentation of cerebral vascular structures in 3DRA images, even fewer for the image study with cerebral AVM [47, 61, 102, 123, 124]. Until now, there does not exist a standard method

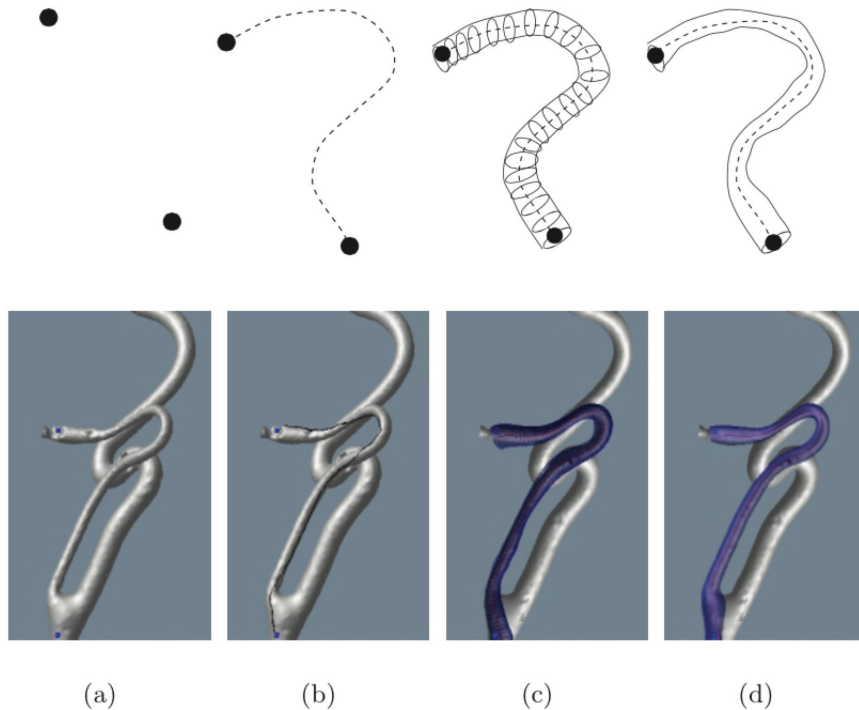


Figure 3.10: An illustration of generalized cylinder model. (a) Two points are initialized as start and end point. (b) A geodesic path is computed between the two points. (c) The circular cross-sections are estimated and swept along the axis. (d) The vessel wall and the vessel axis [122].

for this kind of application and most proposed methods require quite a lot user interactions [47, 124].

Second, for our application area the choice of the segmentation method is very difficult. The position and the size of nidus vary in each patient. Image quality depends of numerous parameters such as acquisition time, image resolution or presence of other anatomical structures in the neighbourhood of the vascular system. These reasons make it extremely difficult to design a model for the segmentation of vascular network with AVM. Therefore, statistical and pattern recognition approaches seem unsuitable for our problem. The segmentation with deformable models for 3D images is very time-consuming and its parametrization is not trivial, while small vessels risk to be neglected.

In our work we prefer to segment the cerebral vessels from the 3DRA images using the region growing approach. As presented above, the region growing segmentation method has proved its efficiency in extracting blood vessels, even when they are of small sizes. This approach also offers numerous qualities such as simplicity, reproducibility and computing time rapidity. Another aspect that

guided our choice is the ability of this method to be easily and well implemented in three dimensions, allowing benefiting from the high resolution of our images. Another reason to employ this approach is that the AVM is considered as one connected component. Therefore, the region growing method can extract the whole vascular structure from any seed point located in it. The main difficulty of this method, which is common to several segmentation problems, is that it is sometimes difficult to guarantee the segmentation accuracy due to noise and intensity variability. As a consequence, it may lead to leakage of holes in vessel regions or over-segmentation of non-vessel points. We showed that many post-processing filtering methods were consequently proposed to improve the initial formulation of the algorithm and to deal with segmentation accuracy improving.

### 3.4 VESSEL RECONSTRUCTION AND 3D VISUALIZATION

#### 3.4.1 *Vessel reconstruction*

To visualize the vessels surface, several methods have been proposed according both to the segmentation outcome and to mesh generation methods. For example, model based reconstruction techniques use assumptions such as circularity of the cross-section and generally require the knowledge of the centerline of vessels provided by segmentation and a choice of geometric primitives (cylinders for instance) [125]. However, the accuracy of the generated surfaces which present a low visual quality might not be sufficient for the diagnosis of pathologic structures. The model-free surface representations require no assumptions and exploit the segmentation results to construct a set of points from which smooth surfaces are obtained [126]. A higher accuracy can thus be achieved with the Marching Cubes or the Constrained Elastic Surface Nets methods [127].

#### 3.4.2 *Vessel visualization*

The accurate visualization of cerebral vessel is essential to guarantee the precise analysis of the vessels angiostructure and the detection of abnormalities. Another requirement is to improve the 2D data visualization in 3D information, so that there is a reliable and complementary information between the two.

Four volume visualization techniques have proven useful over the years for clinical angiographic practice: *Multi Planar Reconstruction (MPR)*, *Maximum Intensity Projection (MIP)*, *Surface Rendering (SR)* and *Volume Rendering (VR)*.

#### 3.4.2.1 *Multi-planar reconstruction*

In *Multi-Planar Reconstruction* (MPR), from a 3D volume, 2D slices are shown on the screen. These slices are the intersections of the volume by planes, either orthogonal to the original acquisition frame, or oriented arbitrarily. In the latter case, interpolation of the original data is required to produce the grayscale values of the intersected pixels. As MPR displays the original, possibly interpolated, grey-level values, it is always the reference visualization method in case of doubt. It is also possible to display the intersection of the data volume with any surface: the technique is called *Curved Planar Reformation* (CPR). It is particularly useful in the context of angiography, where the intersecting surface can be chosen to include the centerline of the vessel of interest, thus showing a cut of the vessel lumen along the vessel course. This technique can produce visual renderings of the lumen of a whole arterial tree in one image [128].

#### 3.4.2.2 *Maximum intensity projection*

*Maximum Intensity Projection* (MIP) is the most common visualization technique aside from MPR. It consists of projecting a set of rays through the volume in the same direction and building a 2D image composed with the highest value of each ray. The MIP has the following advantages and drawbacks:

1. It looks like a conventional, X-Ray angiogram, therefore, it allows experienced radiologists to interpret MIP images without additional training.
2. The distribution of gray levels in the MIP is close to the one observed from the original volume.
3. The objects of interest can be overlapped by others.
4. It over-estimates the vessel diameter.
5. This basic strategy fails if contrast-enhanced vessels and skeletal structures that also exhibit high intensity values, are close to each other.

The removal of bony structures is a necessary preprocessing step in such cases since static MIP images do not provide any depth perception, they are either interactively explored or presented as animation sequences. However, small vascular structures are often suppressed since they are primarily represented by border voxels, which are visually biased by the partial volume effect. Those voxels appear less bright than the center voxels of large vessels. This method called either

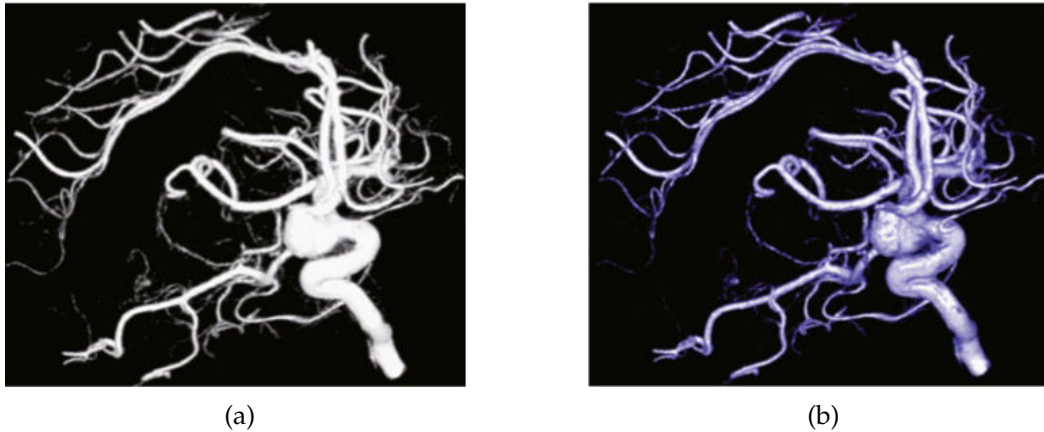


Figure 3.11: (a) Maximum intensity projection of brain vasculature. (b) Shape-enhanced maximum intensity projection [130].

*local MIP* or *Closest Vessel Projection (CVP)* [129] can provide good results but requires a robust algorithm to determine the local thresholds.

Another novel method [130] is a shape-enhanced MIP that can fast render internal structures with shape cues and local context information. Depth-based colour cues based on the HSV (*Hue Saturation Value*) colour model are also used to improve the visual perception of structures, especially depth perception (see Figure 3.11).

### 3.4.2.3 Surface visualization

There are two main types of surface visualization methods: the data-based and the model-based methods.

In *surface rendering*, first, in the slice images, the objects of interest are segmented by thresholding. The boundary of the binary volume is then first-order approximated by a set of polygons, typically using the "marching cubes" method [131]. For the perception of the three-dimensional structure it is helpful to dynamically move the viewpoint. However, with this method, the quality of surface rendering is relatively low due to inhomogeneities in the contrast agent distribution and to linear interpolation.

Another drawback of the binary segmentation is aliasing artifacts which could be reduced by a classical smoothing but this operation often brings modifications in the vascular topology. Better results can be achieved with error-controlled smoothing approaches, such as low-pass filtering [132] and the improved Laplacian smoothing introduced in [129]. Figure 3.12 gives an example of smoothed surface rendering.

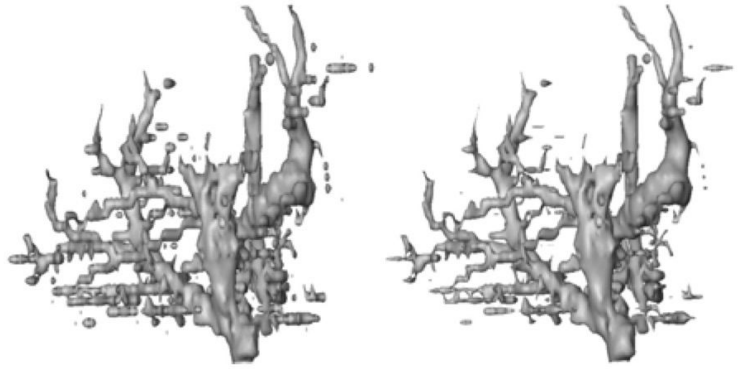


Figure 3.12: General mesh smoothing techniques are not appropriate to post-process vascular structures created with Marching cubes (left). The Low-pass filter was carefully adjusted (10 iterations, weighting factor 0.5) but no parameter adjustment lead to satisfying results (right). The quality of the visualization is very low [126].

When it comes to the visualization of small vascular structures, due to their size and limited spatial resolution of medical image data, these structures are represented with only a few pixels per slice. Therefore, a straightforward surface mapping of vessels in 3D leads to noisy visualizations. This makes the study of their topology very complicated from such visual presentations.

For therapy planning and educational purposes, the *model-based techniques* are appropriate. They allow reducing noise, and on each slice, performing vessels segmentation and extracting their centerlines and diameters. The often used models include cylinders [133] and truncated cones [134]. The truncated cones represent well how the diameter decreases toward the peripheral parts. The quality depends on the number of vertices used to approximate the circular cross-section as well as on the number of graphical primitives attached along the skeleton. Though explicit methods create artifacts in branchings which are especially well seen in close-up views. The major advantage of these methods is their speed (see Figure 3.13).

#### 3.4.2.4 Volume rendering

*Volume rendering* does not require any preliminary segmentation step. This is an extension of the MIP principle, which takes into account edge information such as gradient value for instance. In contrast to projection methods, direct volume rendering provides realistic depth-cues by blending data considering the “in-front-of” position.

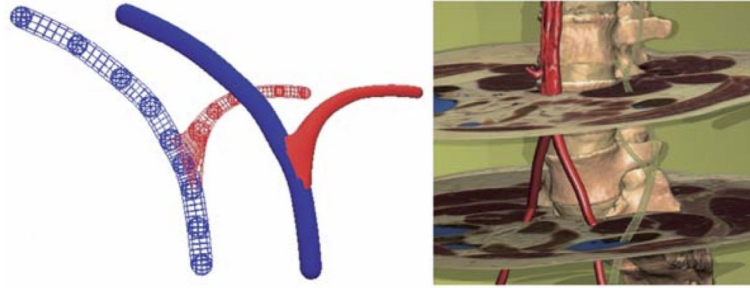


Figure 3.13: Small anatomic tree structures are modelled by placing ball-shaped markers and represented as a special variant of splines [126].

As a drawback, the direct application of general volume visualization algorithms to rather small vascular structures leads to aliasing artifacts. In addition, in 3D it is not trivial to recognize the objects. They might seem smaller, or might be occluded by other objects. Change (rotation, translation) of the point of view and the opacity of the object surfaces can facilitate the task. However, it might not satisfy the user and it may distract him. When applying transparency, it is often not enough due to possible numerous occluding objects. The very nature of transparency represents less of information, therefore being less recognizable. In addition to a quality visualization, for therapy planning, other vascular characteristics are useful and can facilitate their exploration. In particular, the centerline together with vessel radius and the branching graph are highly desirable for the visual exploration [126, 135]. Provided this information, subtrees may be visualized selectively based on the branching graph and/or the vessel geometric criteria. Visual exploration and quantitative analysis techniques can be distinguished. One of the early benefits of curve-skeletons was for virtual navigation, viewing its centeredness to generate collision-free paths through a scene or through an object. With a scene composed of 3D objects, the skeleton of the background gives a free path through the scene. The centered, thin, homotopic to the original image skeleton, which is fitted inside the vessel, can be used to assist visualization and study of vascular trees.

The example of such vessel visualization can be seen in Figure 3.14. According to [1], this method has been developed and refined in fruitful discussions with radiologists and is a good comprise between precise and easy-to-interpret visualizations.

Visual exploration techniques permit selecting subtrees or subregions, *e.g.*, regions close to a AMV, tumor or other diseased area. Subtrees may be shown

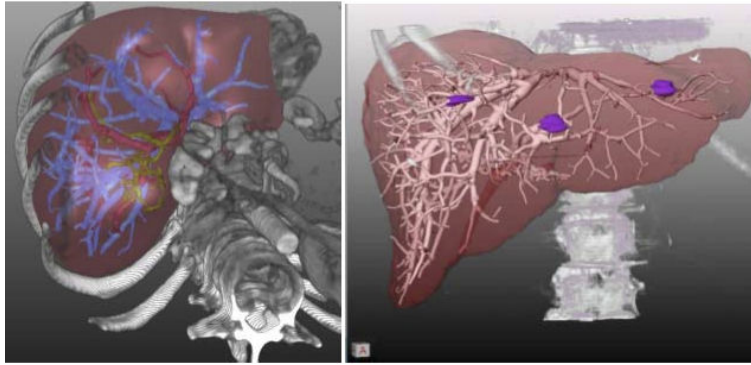


Figure 3.14: Hybrid combination of the direct volume rendering of bone structures and surface rendering of intra-hepatic structures (liver, vascular systems, tumours in the right view). The bone structures serve as anatomic reference for the intra-hepatic structures [1].

using a hierarchy measure or a criterion which relates to the vessel radius. We will further discuss such approaches in [Chapter 4](#).

In vascular structure visualization, accuracy and removal of discretization artifacts are two major and conflicting goals. For diagnostic procedures, accuracy is more important, as it gives rise to techniques without model-assumptions. For therapy planning, minor deviations are usually acceptable and therefore model-based techniques are appropriate.

### 3.5 CONTRIBUTIONS

In this section our contributions of cerebral vascular segmentation from 3DRA images are presented. First, we developed an algorithm that extracts the vascular structure slice by slice. Several approaches were tested, including geodesic reconstruction [136] from mathematical morphology approach and a level set based method [75]. A tracking method is then proposed after 2D segmentation in order to follow the trajectory of a selected vessel.

The evaluation of the 2D algorithm led us to design a new 3D algorithm that use the geodesic reconstruction method for initialization but region-growing is preferred to level set edge detection which is time consuming and imprecise. A 3D region growing based technique is presented to efficiently segment the whole 3DRA image. In the following step, we applied Delaunay triangulation to visualize the reconstruction result. In the last part, a mathematical morphology

approach is employed to separate AVM into three components: the arterial and venous trees and nidus.

### 3.5.1 2D slice-by-slice segmentation

To extract the cerebral vessels from the 3DRA images, our first approach was to segment the datasets slice by slice. First, the pixels intensity distribution within the images was analyzed. [Figure 3.15](#) shows the logarithmic histogram of pixels intensities of a 3DRA image, normalized between 0 and 255. Pixels intensity distribution can be divided into two classes: vessels and background, including soft tissue and bones [\[61\]](#). We can see that the intensities of the different brain structures are not clearly separated on the histogram. So, it is difficult to precisely determine the optimal threshold. Consequently we attempted to segment vessels by using geodesic reconstruction (see [Section A.1](#)) and level set approaches (see [Section A.2](#)).

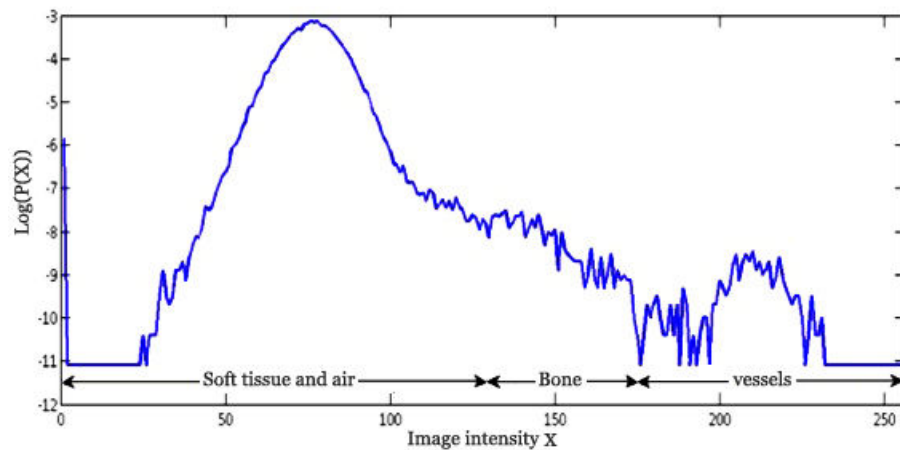


Figure 3.15: Logarithmic histogram of pixels intensities of a 3DRA image, normalized between 0 and 255.

#### 3.5.1.1 Tracking

After the segmentation of the cerebral vessels from each slice of the 3DRA dataset, the next step is to follow the trajectory of a given vessel, particularly the suspicious feeding arteries. We propose a tracking method, which performs slice by slice and requires a simple user interaction to select the vessel to follow. It is capable of

detecting a bifurcation and following independently the detected branches. The scheme of this tracking algorithm is presented in [Figure 3.16](#).

In this algorithm, let  $C_n$  and  $P_n$  denote respectively the contour and the centroid (barycenter) of the vessel to follow in image  $Im_n$ . During the passage from  $Im_n$  to  $Im_{n+1}$ , we identify the centroid  $P_i$ , the equivalent radius  $R_i$  of the corresponding region, as well as the distance between  $P_i$  and  $P_n$ , named  $D(P_i, P_n)$ . Afterwards, the algorithm selects the two objects which are most proximate to the  $C_n$ , determined by the distance  $D(P_i, P_n)$ . In terms of the nearest object, the satisfaction of the condition  $D(P_i, P_n) < R_n$  represents the continuity of the vessel on the image  $Im_{n+1}$ , where  $R_n$  signifies the equivalent radius of  $C_n$ . Otherwise, we say the algorithm reaches the end of the tracking vessel if the condition is not matched.

Moreover, to detect the presence of an additional branch, *i.e.*, the bifurcation,  $R_1$  and  $R_2$ , the equivalent radius of the two nearest objects of  $C_n$  must also verify the following condition, where the two thresholds are selected experimentally.

$$0.75 < \frac{|R_1^2 + R_2^2|}{R_i^2} < 1.2 \quad (3.4)$$

### 3.5.1.2 Results of 2D segmentation and discussion

To facilitate various processing and implementations of our programs, an interactive interface was created with *Matlab* (see [Figure 3.17](#)). Some parameters have been defined by default after making several experimental tests and based on the observation of the histogram. In addition, we have given the user the ability to change the values of these parameters and view results in real time.

A 2D segmentation result based on a geodesic reconstruction method is shown on [Figure 3.18](#). We note that by varying the value of the low threshold, the size of regions in the segmentation result is changing. The higher threshold controls the number of extracted regions. The more one increases the value of the high threshold, the less regions will be obtained in the final segmented image.

The [Figure 3.19](#) illustrates the propagation process with level set. A rectangular curve is positioned in the image. It includes vessels to be segmented and it is deformed under the effect of forces described in [Equation A.8](#). As the evolution force is much more important at the beginning because of a high elasticity of the curve and a low gradient of intensities in the image (homogeneous area), the displacement of the curve is quick. Then we notice that the shape changes slower as we approach the limits of the objects to be segmented. The evolution becomes stable and stops when all components have been detected and that the curve

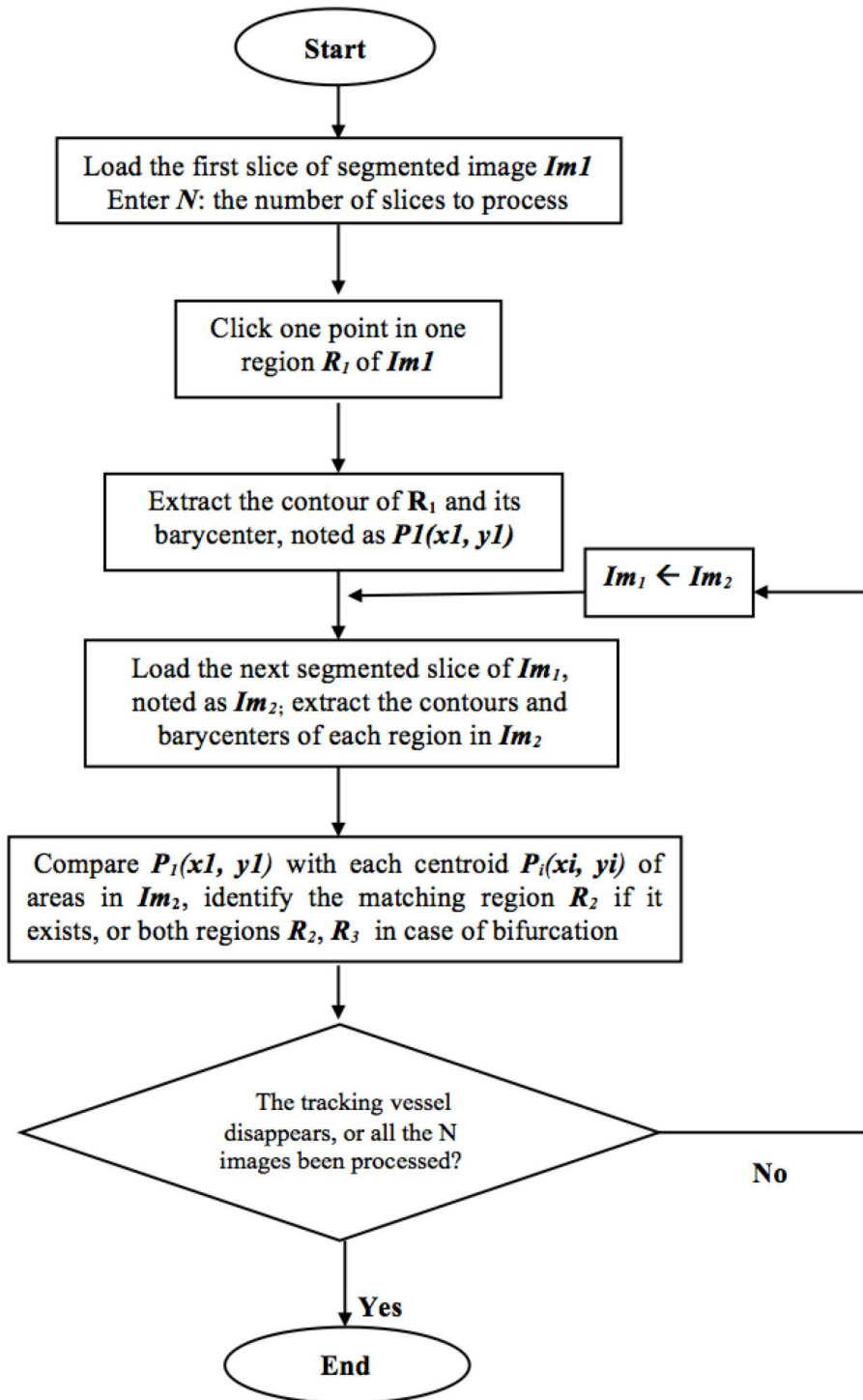


Figure 3.16: The schema of our tracking algorithm

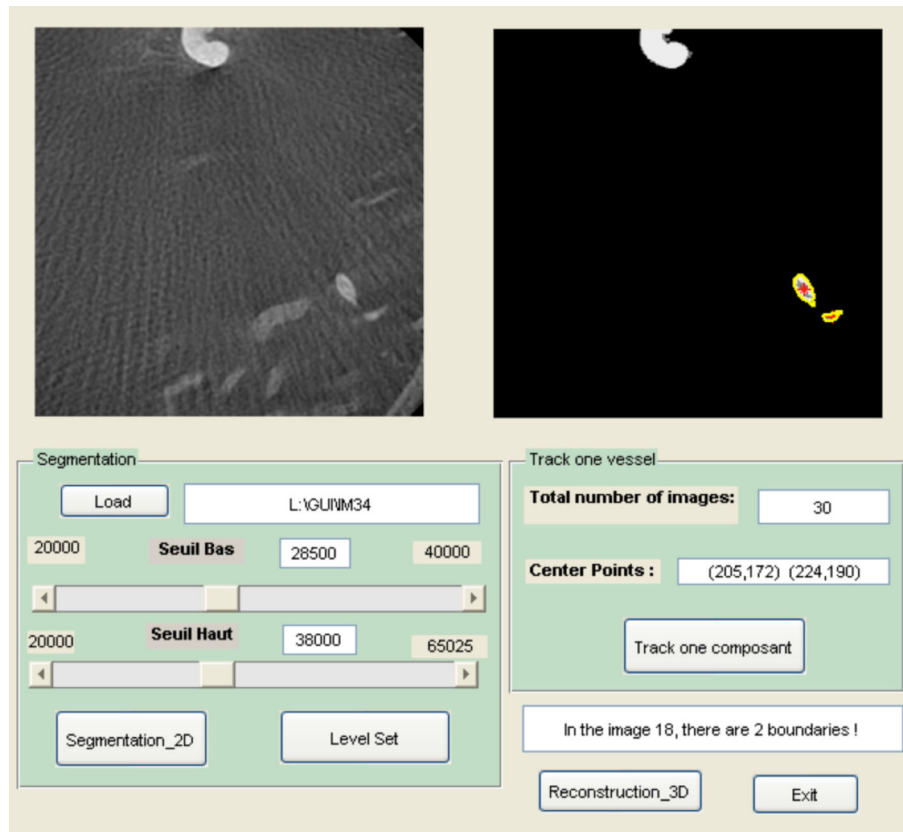


Figure 3.17: The interactive interface of our segmentation algorithm.

coincides precisely with the contours of the segmented objects. In [Figure 3.19\(f\)](#) we see that the expected result is obtained at the end of the segmentation process. Indeed, the contours of the two vessels in the region of interest are detected.

The segmentation tests with level set give satisfactory results on our 3DRA images. This method automatically takes into account the topological changes of the image is thus well adapted to the segmentation of several vessels of the same image. However, the process requires the use of multiple iterations for segmenting each image slice separately and is very time consuming. Furthermore, it can only extract the large size vessels because tiny ones are considered as noise by the algorithm.

[Figure 3.20](#) shows some results obtained by our tracking method. The shape and position of the vessel change, we get to detect the bifurcation and follow the two sub-branches simultaneously. Other tests were performed to validate our method of tracking. In its current state, the tracking method of a vessel depends greatly on the position of center of gravity of the region, which is a limitation of our algorithm. Indeed, when the vessel shape is modified or when several vessels appear close to the tracked ones, the algorithm can turn to a neighbouring branch.

To solve this problem, we could add a criterion based on the similarity between the shapes of the regions.

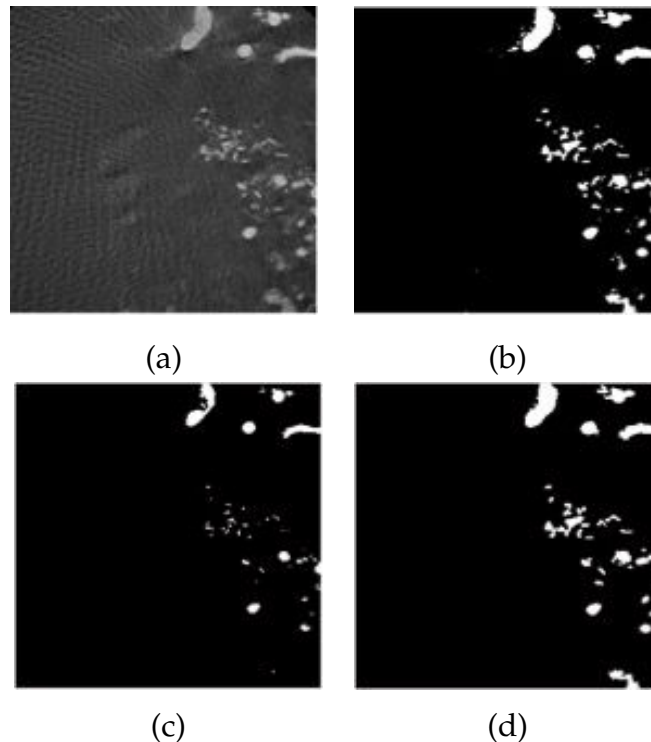


Figure 3.18: Segmentation results using the geodesic reconstruction with a couple of thresholdings. (a) Original image. (b) Binary image with a lower thresholding (0.45). (c) Binary image with a upper thresholding (0.7). (d) Geodesic reconstruction result with these two thresholds.

### 3.5.2 3D region growing segmentation

The 2D segmentation of 3DRA images demonstrates that geodesic reconstruction gives good results while level set method is sensitive to the setting of parameters and very time consuming. Consequently we chose to perform 3D segmentation by region-growing which is initialized by seed points automatically detected by a geodesic reconstruction.

#### 3.5.2.1 Principle

The aim of the segmentation is to find regions of homogeneous behavior [137]. The segmentation by region growing precisely exploits this homogeneity property of the objects to be segmented. It is based on the two proprieties of similarity and proximity points. The growing process starts from one or more initialization

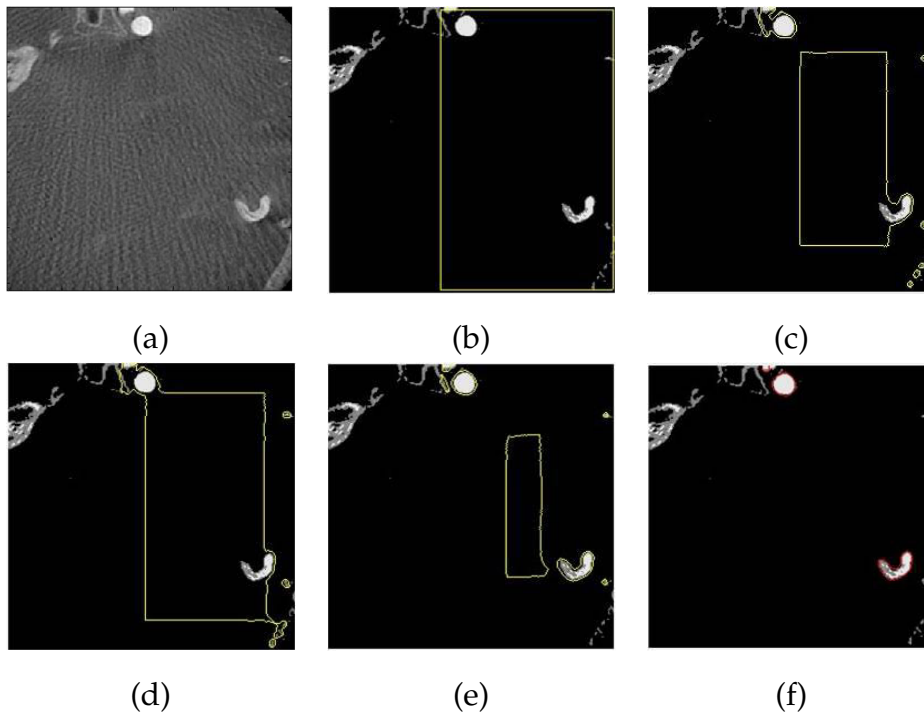


Figure 3.19: Illustration of different stages of the evolution of the curve during the segmentation of 3DRA image using the level set. Initialization of a rectangular shape around the region of interest (a), the different phases of the evolution of the curve (b) - (e) and the final result (f).

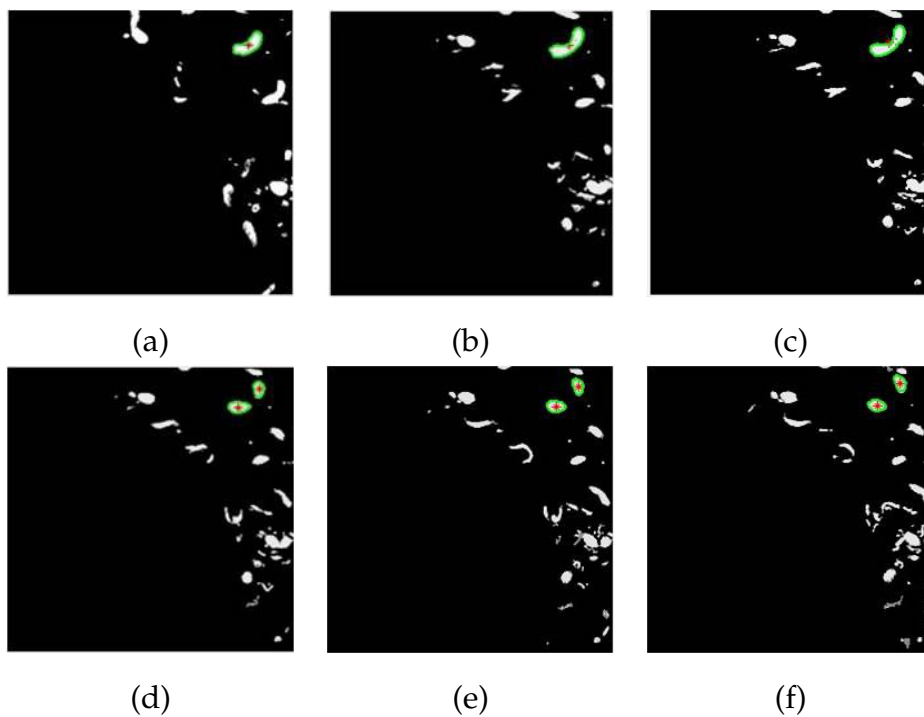


Figure 3.20: An illustration of vessel-tracking with the proposed method.

points called *seeds points*. The seeds can be manually or automatically defined. So, the first problem to resolve is determining the location of these seeds in the image.

Starting from the selected seeds, the algorithm analyzes the immediate neighbouring pixels searching for those sharing some common similarity criteria (colors, intensity, texture *etc.*). The pixels satisfying this condition are labelled and added to the same region as the initial seed. The process is repeated for each new agglomerated pixel and the region grows progressively. The segmentation process stops when no new pixel being added between two iterations.

The final result can be improved by introducing pre or post-processing techniques allowing the image contrast enhancement or the regularization of the extracted regions frontiers. The general region growing segmentation algorithm can be summarized in three steps:

- Initialization step: define the start partition, depending on the image information.
- Growing step: define the homogeneity criterion for the segmentation.
- Optimization step: include pre or post-processing techniques to improve the segmentation result.

### 3.5.2.2 Neighbourhoods and connectivities

An early definition of digital topology can be found in [138]. When considering discrete space, a digital image is described as a set of  $\mathbb{Z}^3$ , where each point  $x \in \mathbb{Z}^3$  is called a *voxel* and defined by its space coordinates  $(p_x, p_y, p_z)$ . Each voxel can be considered as a cube which is composed of 6 faces, 12 edges and 8 corners. We commonly use three types of neighbourhood for two voxels depending on their adjacent relationships. Two voxels  $p$  and  $q$  are 6-connected if they share a common face. Similarly, 18-connectivity is established if two voxels share either a face or edge, while 26-connectivity is established if they have a common edge, face or corner. In addition, we say that two voxels  $p, q$  are *adjacent* if  $p \cap q \neq \emptyset$ . For each voxel  $p$ , we have  $p \in N(p)$  and we denote set  $N^*(p) = N(p) \setminus \{p\}$ .

An *n-path* denotes a sequence of voxels  $(p_1, p_2, \dots, p_j)$  in which  $p_i$  n-adjacent to  $p_{i+1}$ . An object is defined as an *n-connected component* if any two voxels in that component are connected by an n-path.

An illustration of these neighborhoods is demonstrated in [Figure 3.21](#). The definitions of the neighborhoods are as follows:

*6-neighborhood:* We note  $N_6(x) = V_1^1(x)$  and  $N_6^*(x) = N_6(x) \setminus \{x\}$ ,

*18-neighborhood:* We note  $N_{18}(x) = V_\infty^1(x) \cap V_1^2(x)$  and  $N_{18}^*(x) = N_{18}(x) \setminus \{x\}$ ,

*26-neighborhood:* We note  $N_{26}(x) = V_\infty^1(x)$  and  $N_{26}^*(x) = N_{26}(x) \setminus \{x\}$ .

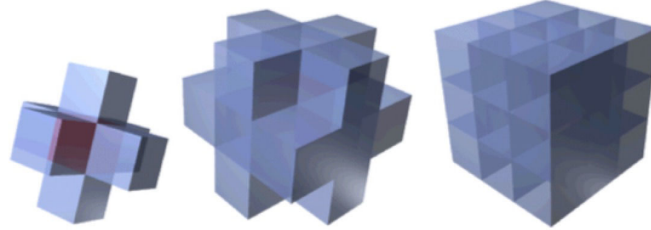


Figure 3.21: 3D neighborhoods. From left to right: 6-connectivity, 18-connectivity, 26-connectivity.

### 3.5.2.3 Automated seed selection

One essential criterion for the success of the region growing segmentation is the initialization of the seeds points. To this purpose and for each region to be segmented, we propose to automatically define a seed point in image position corresponding to a structure of interest. To reduce user intervention, we propose to automatically define the seeds on the first slice of the 3DRA volume.

An example of a 3DRA axial slice is given in [Figure 3.24\(a\)](#). In order to obtain markers of the vessels and to locate these structures of interest, a thresholding by morphological geodesic reconstruction ([Section A.1](#)) is applied. This resulted in a binary image where the small structures are removed by considering a size parameter  $S$ , to preserve only pixels belonging to the vessels.

### 3.5.2.4 Location of region growing seed points

The centers of the extracted regions are then defined as the seeds. The center of mass was usually considered as the seed [\[41\]](#). Nevertheless, the forms of vessels are not always convex and the center of mass may be located outside the region. For that reason, we considered a center which should be strictly inside the region. In a binary image  $I$ , let  $R$  be one region of interest which contains  $n$  pixels  $p_i$

( $i = 1, 2, \dots, n$ ). For each pixel  $p_i$  in  $R$ , the sum of all the distances  $D(p_i)$  from this point to all the other pixels  $p_j$  is defined as follows:

$$D(p_i) = \sum_{j=1}^n (|x_i - x_j| + |y_i - y_j|) \quad (3.5)$$

where  $(x_i, y_i)$  and  $(x_j, y_j)$  denote the  $p_i$  and  $p_j$  coordinates. The central point  $p_{center}$  is obtained such as:

$$p_{center} = \text{Argmin} D_{p_i} \mid i = 1, 2, \dots, n \quad (3.6)$$

### 3.5.2.5 Growing criterion

The idea of the region growing segmentation is to incorporate the pixels that satisfy a homogeneity criterion. Once the seed markers are successfully selected on the first slice, we apply the 3D region growing method to segment a given vessel with its branches. The region growing algorithm starts from the corresponding seed point and propagates through the 3D volume in order to carry out the vessel segmentation. If the prior step of locating the seed points is performed on the adequate image, that is the first image of the 3DRA volume, where the ICA is visible, the growing process evolves and extracts the entire vascular tree. Otherwise, one can choose the vessel to reconstruct by selecting one seed from all the defined markers.

Because of the uniformity of the vascular voxels intensity on the 3DRA images, a voxel intensity criterion is used. Let  $I_{max}$  and  $I_{min}$  denote separately the greatest and the lowest gray level of voxels in the whole volume. Let the voxel  $p_i(x_i, y_i, z_i)$  be the initial seed point,  $I(p_i)$  be the intensity value of  $p_i$ . Each 6-connected neighbour  $p_j$  of  $p_i$  is labelled as the same vessel as  $p_i$  if the following condition is satisfied:

$$|I(p_i) - I(p_j)| < p * |I_{max} - I_{min}| \quad (3.7)$$

with  $I(p_j)$  the intensity of  $p_j$  and  $p$  a weighting parameter. When the [Equation 3.7](#) is verified for a neighbour  $p_j$  of  $p_i$ , the process is iterated for the 26 neighbours of the voxel  $p_j$ . The segmentation results obtained by the proposed method above are presented and analysed in [Section 3.6](#).

### 3.5.3 3D vessels reconstruction

After the 3D region-growing process is completed, the 2D contours of the segmented vascular structures are extracted slice by slice. They will be exploited, to reconstruct the 3D mesh and provide a useful visualization of the entire vascular tree.

As our region growing based algorithm provided high-quality segmentation results, we propose to simply reconstruct the vessels surface by converting the set of 2D vessels contours resulting from the segmentation, to a 3D mesh using the *Constrained Delaunay Triangulation* (CDT) method [139]. This algorithm that tightly fits the external surface of the vessels converts the set of 2D vessel contours resulting from segmentation to a 3D mesh, constituted of non-overlapping triangles that represent the surface of the vessels.

This algorithm establishes a correspondence between selected points from each two successive contours, belonging to the same vessel (see [Figure 3.24\(b\)](#)). Since the vessels sections are not always convex, the triangulation is constrained by the contours to avoid problems of external triangles construction. The implemented algorithm is able to reconstruct vessels with various forms and sizes and also to identify vessels divisions into two or more branches (bifurcations).

### 3.5.4 Separation of the arteries, nidus and veins

This section deals with an important step in our work. Indeed, distinguishing the three principal components of the cerebral vascular network with an AVM, that are the feeding arteries, the draining veins and the nidus is a challenging and complex task. Such visualization using different colours can help clinicians to understand the angio-architecture of complex vascular malformations.

Until very recently, only few authors proposed to semi-automatically or automatically separate the arteries and veins from the nidus. Forkert *et al.* [80, 81] suggested extracting the nidus volume from TOF MRA images with a classification method, by analyzing the segmentation, vesselness measure, blobness measure and other results. The arteries and veins were identified with the help of *Time-To-Peak* (TTP) parameter map that was calculated from the 4D MRA image sequence. After registration, the mean TTP of the segmented nidus can be calculated. If the TTP of a voxel is shorter than the mean TTP of the nidus, it is defined as a feeding artery, otherwise it is defined as a draining vein.

Clarencon *et al.* [123] distinguished the three kinds of structures by manually tagging different vessels in 3DRA images and then propagated the labelled voxel with region growing algorithm. To obtain an accurate and promising result, the method requires to be attempted several times, multiple arteries and veins should be tagged (10 – 50), and it takes a few hours to complete the segmentation and calculations. Due to these reasons, it may not be realistic to implement this method as a standard clinical solution.

Here, we propose a morphological method to isolate the nidus, arterial and venous networks, which is illustrated in Algorithm 1. We consider that the nidus is the largest ball-like component after the vascular network segmentation.

In the first step, the segmentation result is processed with closing and opening operations by a big sphere-shaped structuring element. This allows detecting the nidus approximately when the radius of the sphere is appropriately chosen (Figure 3.22(a)). When removing the approximate nidus from the segmentation result, the vascular network can be "broken" (Figure 3.22(b)), from which the arterial and the venous networks are isolated according to the connected component sizes (the arterial network is greater than the venous one) (Figure 3.22(c)). In the last step, the nidus is precisely isolated by subtracting the other two components from the segmentation image (Figure 3.22(d)).

---

**Algorithm 1** Separation the feeding artery network, veins and nidus

---

- (1) Detection the approximate form of nidus.
    - (i) Operation "closing" with a sphere.
    - (ii) Operation "opening" with the same sphere (Figure 3.22(a)).
  - (2) Extraction of the veins and the artery network.
    - (i) Removing the approximate nidus from vascular network (Figure 3.22(b)).
    - (ii) Identifying the artery network and the veins by the sizes of connected-components (Figure 3.22(c)).
  - (3) Extraction precisely the nidus (Figure 3.22(d)).
-

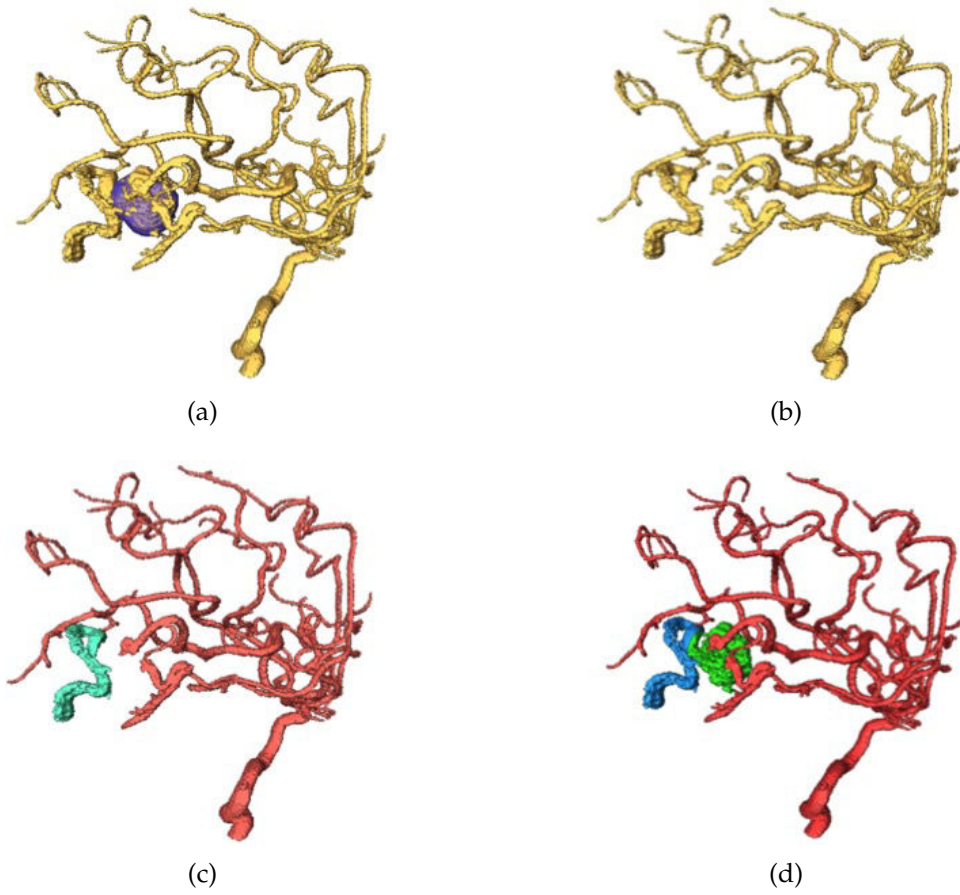


Figure 3.22: Separation of the three components: arterial tree, the veins and the nidus.

### 3.6 RESULTS

Ten patients with age range from 20 to 62 years old, mean age of 44 years, and 30% of women, with brain AVM, underwent 3DRA imaging. Acquisitions were performed with a Philips Allura angiographic unit (Philips Healthcare, Netherlands). The size of the resulted images was  $256 \times 256 \times 256$  pixels/image with cubic voxel size varying from  $0.29 \text{ mm}$  to  $0.49 \text{ mm}$ . The Philips Allura angiographic unit delivers initial reconstructions in 4 seconds.

Our segmentation algorithm was applied on both a region of interest and the whole volume of each 3DRA image of dataset.

For a portion of 3DRA image, the seeds were automatically selected from the first slice of the considered stack of slices. The user was suggested to choose the vessel to reconstruct. As for the segmentation of the entire 3D image, only one region is normally found in the first slice, *i.e.*, the ICA. Then, the region-growing algorithm starts from the corresponding seed point and propagates through the 3D volume in order to carry out the vessel segmentation. Blood vessels with different sizes and shapes as well as multiple bifurcations have been successfully reconstructed. Furthermore, the exploration of the voxel neighborhood in the three spatial directions allows the automated detection of vessels bifurcations, which is very important for the complete visualization of a given vessel with all its branches. For each processed dataset, the analysis of the logarithmic histogram of the 3D image allows the determination of the suitable  $Thres_{low}$  and  $Thres_{high}$  values used in the first step for automated seeds selection. The filtering process enables the detection of all the vascular structures and removes most of noise components (see [Figure 3.24\(c\)](#)).

The remaining noise is simply filtered by eliminating the structures smaller than a given size  $S$ . The  $S$  parameter represents the total number of pixels over the small region and allows computing the area of the smallest vessel section that can be segmented. In the example of [Figure 3.24](#), the image resolution was of  $0.35 \text{ mm}$  and the size parameter  $S$  which controls noise filtering was fixed to 6 pixels. Consequently, vessels with a small diameter of  $0.96 \text{ mm}$  were successfully segmented. The finest reconstructed vessel diameter that was reached by our algorithm, on all datasets was  $0.7 \text{ mm}$ .

The segmentation result of a portion 3DRA image is firstly studied. In [Figure 3.25](#), the ICA is segmented and reconstructed by Denaulay triangulation from a set of 60 3DRA slices. The obtained result shown by [Figure 3.25\(c\)](#), which is visually compared to the reconstruction obtained with the angiographic unit ([Fig-](#)

ure 3.25(a)) by a neuroradiologist. We can easily see that this part of vessel was successfully reconstructed. Another example shows the reconstruction of the two branches of the *Anterior Cerebral Artery* (ACA) from 120 3DRA slices (Figure 3.27). Different viewing angles allow for a greater visualization of the vessels bifurcations. We also show on Figure 3.27(a)-Figure 3.27(f) vessel reconstruction results obtained with our algorithm in comparison with the corresponding DSA images. Thus, the whole process including the 3D segmentation followed by the Delaunay reconstruction was able to automatically reconstruct a vessel in 3 or 4 seconds.

To evaluate the sensitivity of the proposed segmentation algorithm to the single parameter  $p$ , which presents the similarity tolerance, the percentage of segmented voxels to the whole volume was calculated on several patients as  $p$  varied from 0% to 100%. The results were nearly identical when  $p$  was located in a wide range; otherwise there existed an obvious under-segmentation or over-segmentation. One example is shown in Figure 3.26, the curve is stable as  $p$  changes from 22% to 35% (in the red block), the segmented vascular region occupies a proportion around 1% of the entire image volume and this rate matches well with [61]. The value of  $p$  was determined as the segmentation results became stable while the user was changing the  $p$  in real time.

The surface reconstructions were consequently obtained from the segmentation. As it is demonstrated in Figure 3.23, the reconstruction results were in good agreement with the conventional reconstructions delivered by Philips Xtravision. Besides, our study can detect some additional vessels segments (pointed out with arrows). Moreover, all the 10 reconstructed vessel networks presented very little noise.

For all the images of the 10 patients, we have compared the surface construction of segmentation results with the construction provided by Osirix (a commercial software) and by Philips Xtravision. The comparisons can be seen from Figure 3.28 to Figure 3.35 and are validated by two expert neuro-radiologists. It should be addressed that the segmentation results are only evaluated visually in this work as no real ground-truth knowledges are available for this purpose.

The proposed segmentation algorithm is implemented with *Matlab* on the desktop computer with two cores 2.4GHz processors, 8GB internal memory, for one clinical image (Figure 4.24) it takes around 1 minute. For the separation on the AVM and vascular networks, the operation on itself is instant, however it takes a few tries to choose the right size of the structuring element.

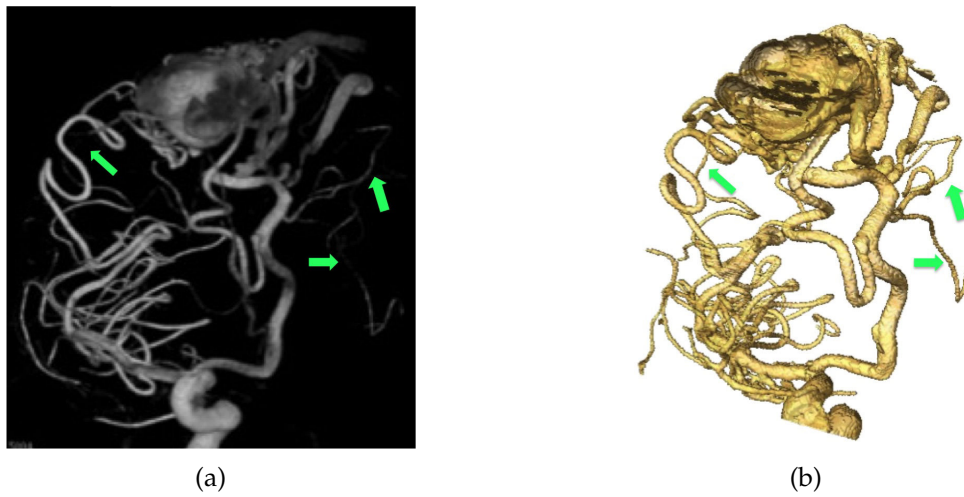


Figure 3.23: Comparison of reconstruction by (a) Xtravision and (b) our region growing segmentation results. The arrows point out the additional segmented vessels detected by our method.

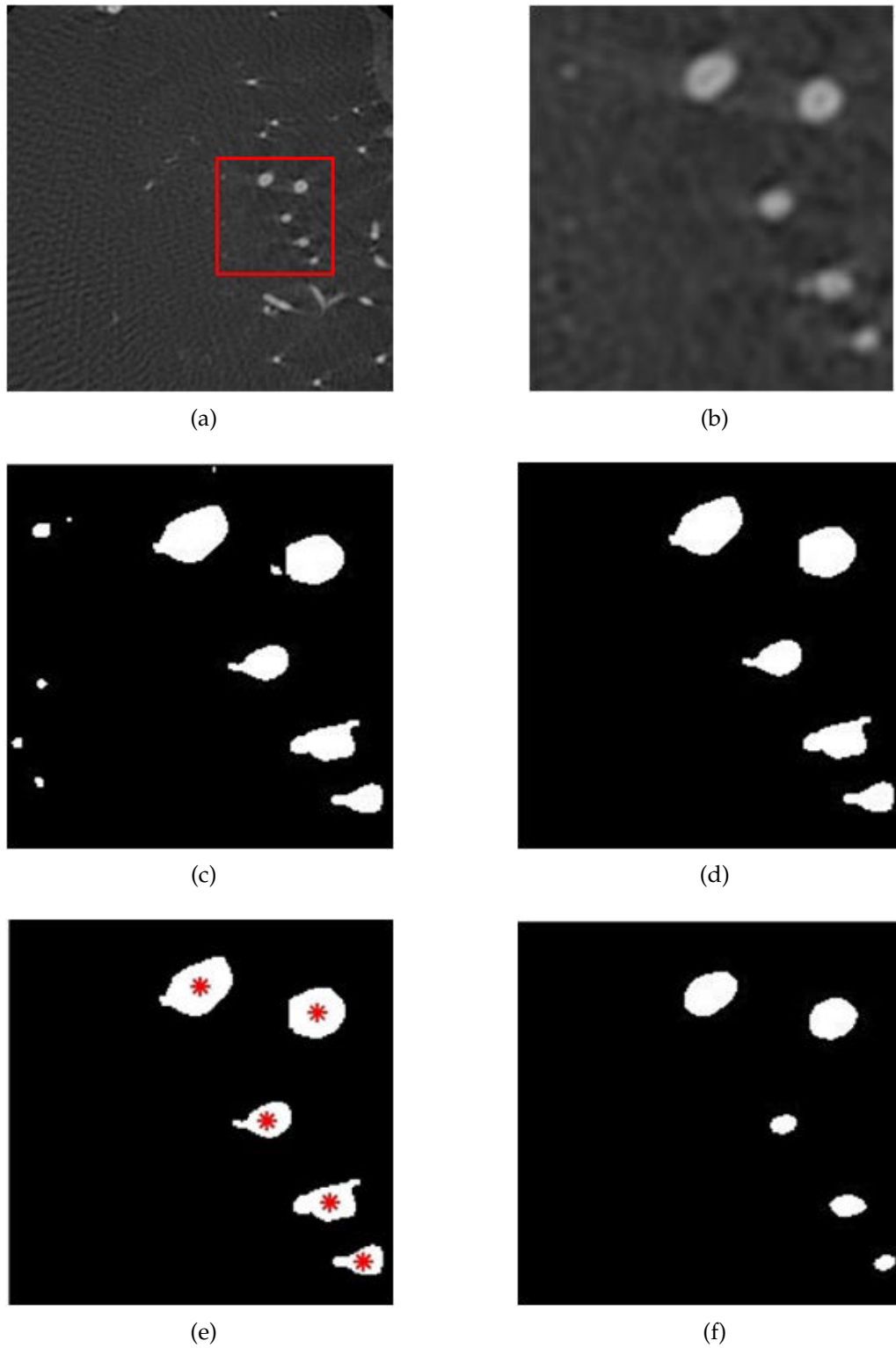


Figure 3.24: Segmentation results after the binarization and filtering steps for a 3DRA image. (a) A 3DRA slice. (b) A zoom-in on a region of interest containing vascular structures. (c) The obtained binary image for the normalized threshold values  $Thres_{low} = 0.28$  and  $Thres_{high} = 0.43$ . (d) The filtered binary image with  $S = 6$ . (e) The detected seeds points (f) The final region-growing segmented vascular structures from the seed points.

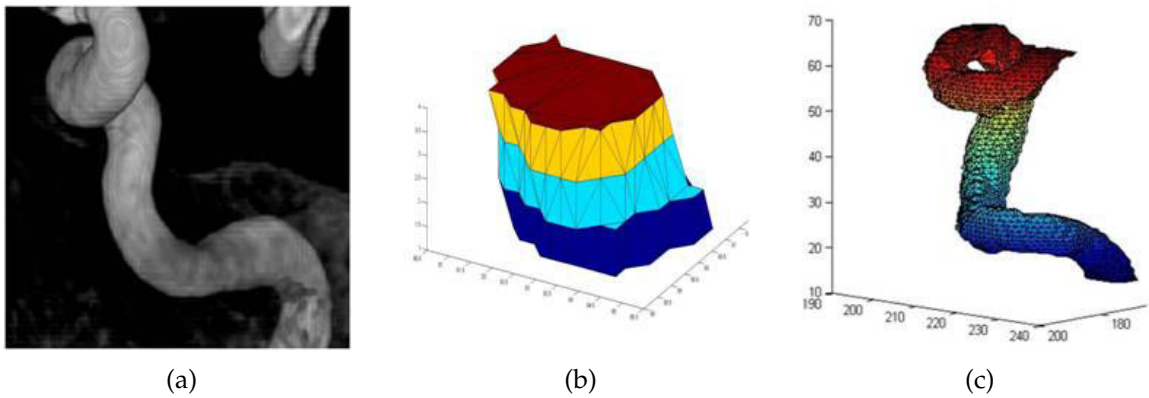


Figure 3.25: (a) Part of the internal carotid artery reconstructed from 60 3DRA slices with the Philips Allura unit. (b) An example of a 3D mesh obtained after the 2D to 3D Delaunay reconstruction of four successive contours. (c) The obtained 3D constrained Delaunay reconstruction result for this vessel.

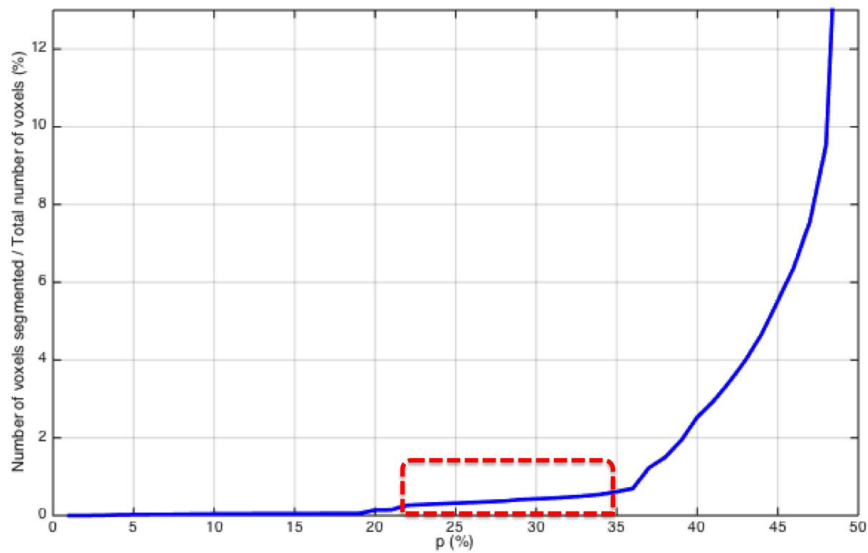


Figure 3.26: The sensitivity of segmentation to parameter  $p$ .

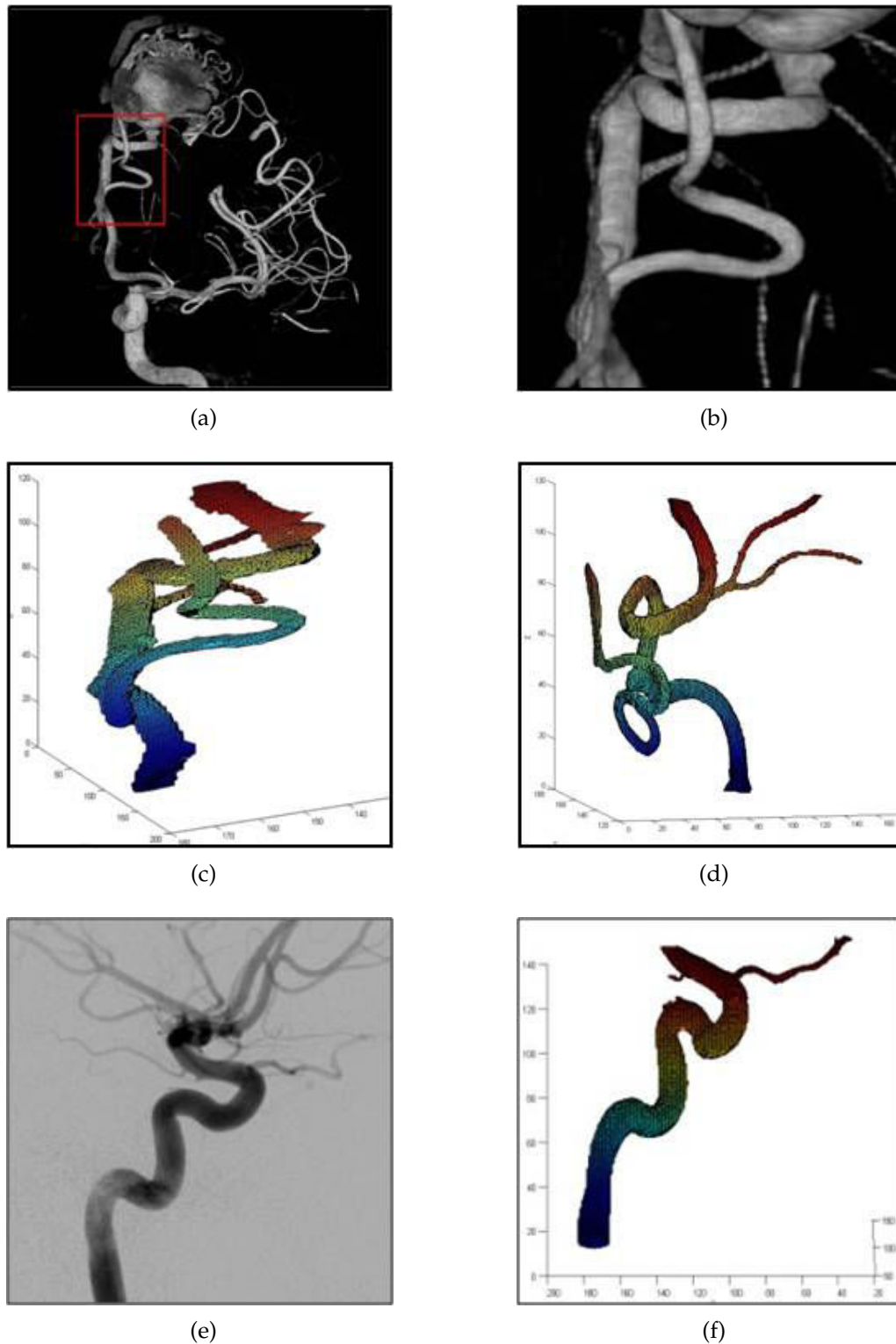


Figure 3.27: Examples of vessels reconstruction. (a) The reconstructed vessel tree with the Philips Allura unit, (b) zoom-in of the Anterior Cerebral Artery (ACA). (c) ACA reconstruction from 120 3DRA slices using the proposed method with the same view angle. (d) Visualization from another angle of view. (e) An example of vessel reconstruction using our algorithm (f) the corresponding DSA image.

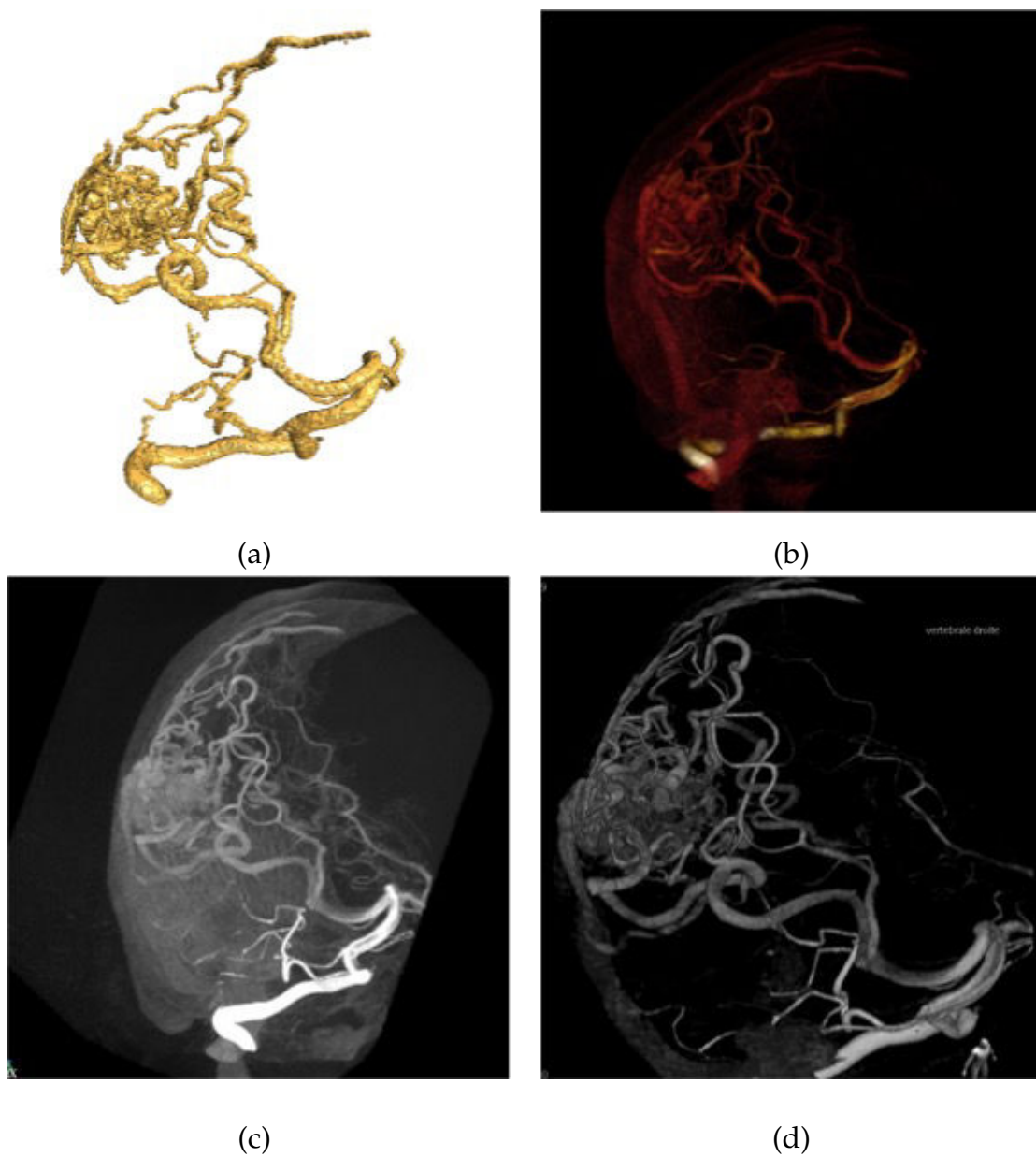


Figure 3.28: Comparison of the segmentation results of clinical data (Patient 1). (a) is the visualization of segmentation results obtained by our method, (b) and (c) are the visualization of volume rendering and 3D MIP rendering proposed by Osirix. (d) The visualization provided by Philips.

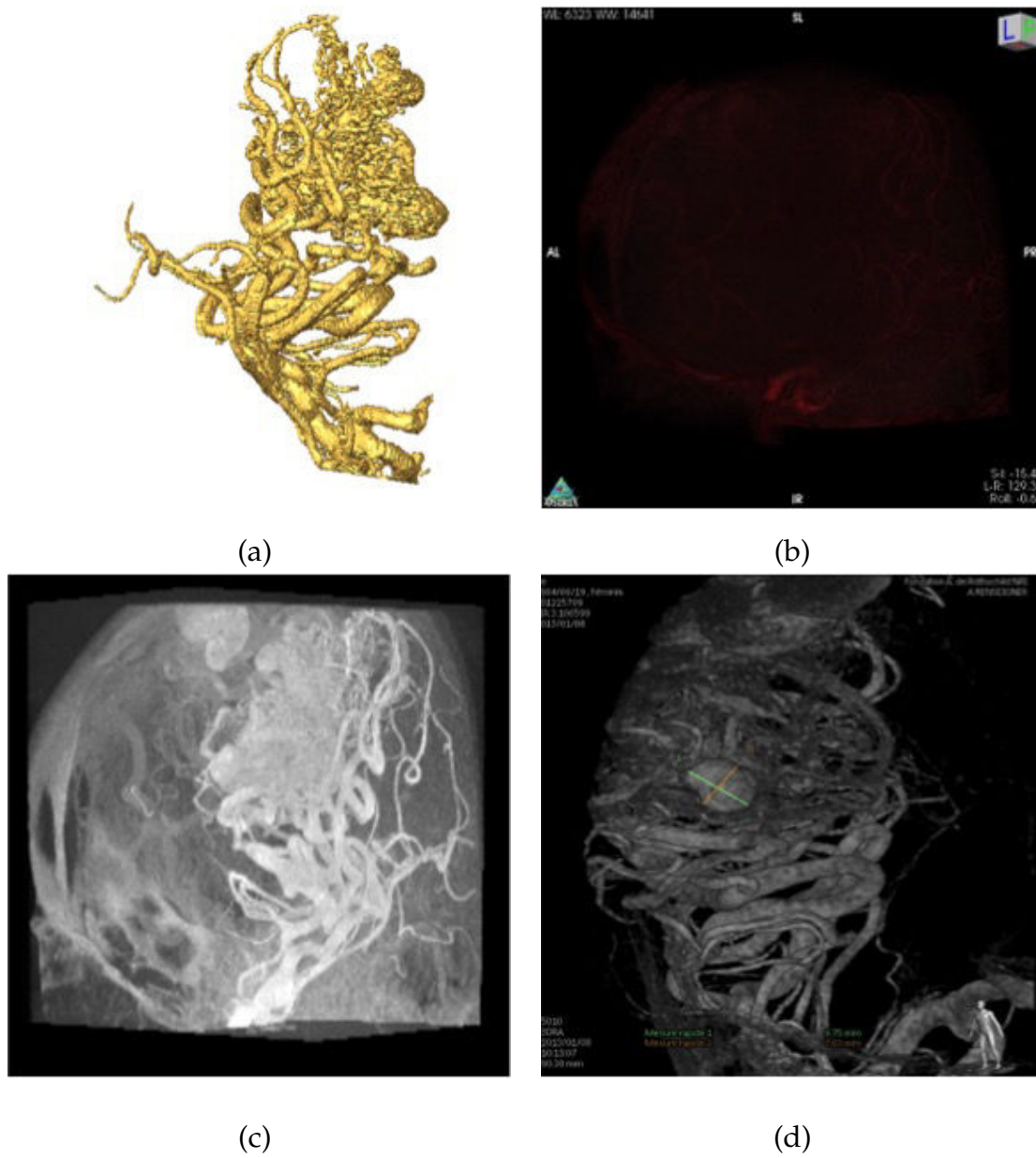


Figure 3.29: Comparison of the segmentation results of clinical data (Patient 2). (a) is the visualization of segmentation results obtained by our method, (b) and (c) are the visualization of volume rendering and 3D MIP rendering proposed by Osirix. (d) is the visualization provided by Philips.

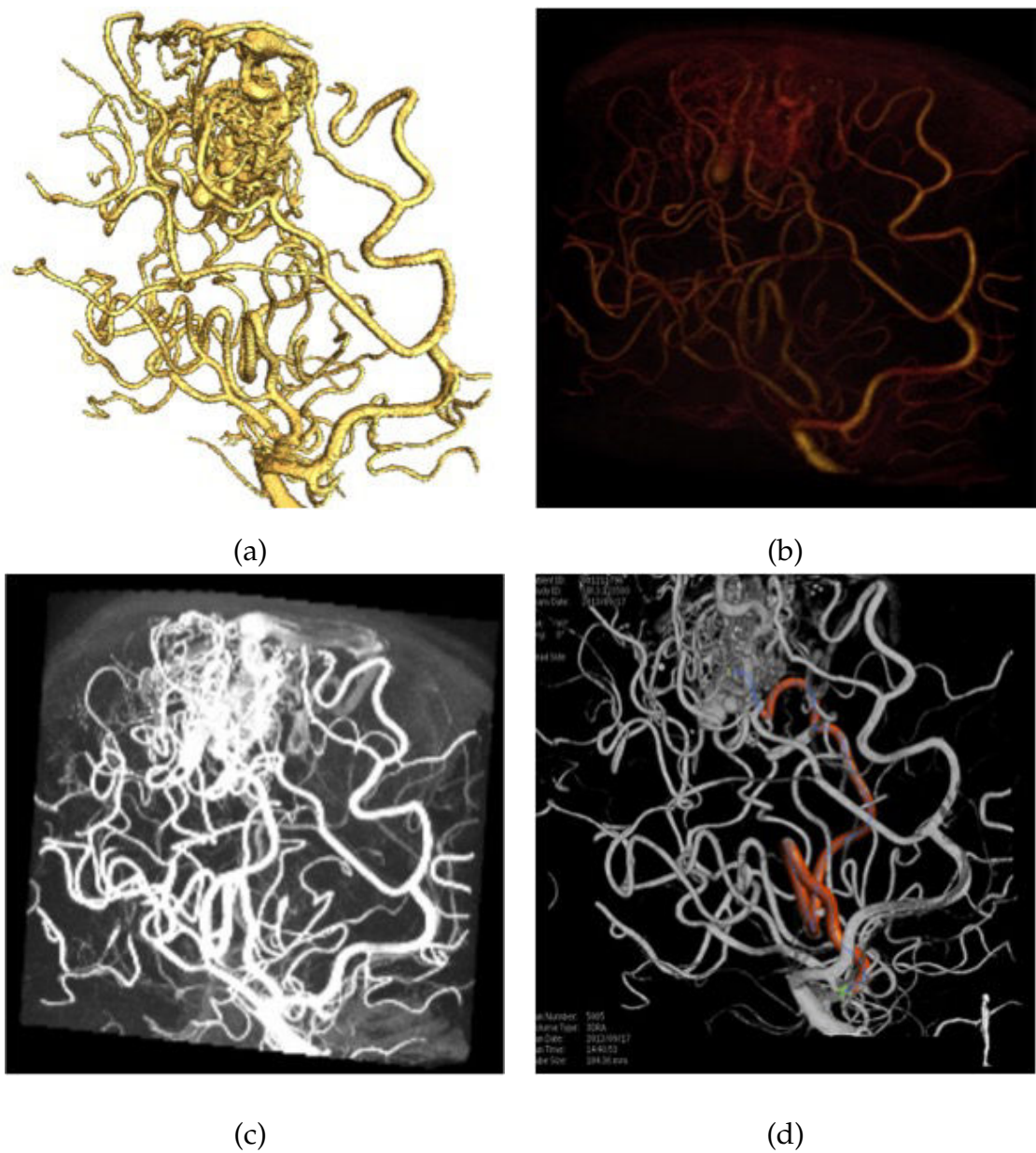


Figure 3.30: Comparison of the segmentation results of clinical data (Patient 3). (a) is the visualization of segmentation results obtained by our method, (b) and (c) are the visualization of volume rendering and 3D MIP rendering proposed by Osirix. (d) is the visualization provided by Philips. The red vessels are obtained by Roadmap, a commercial software.

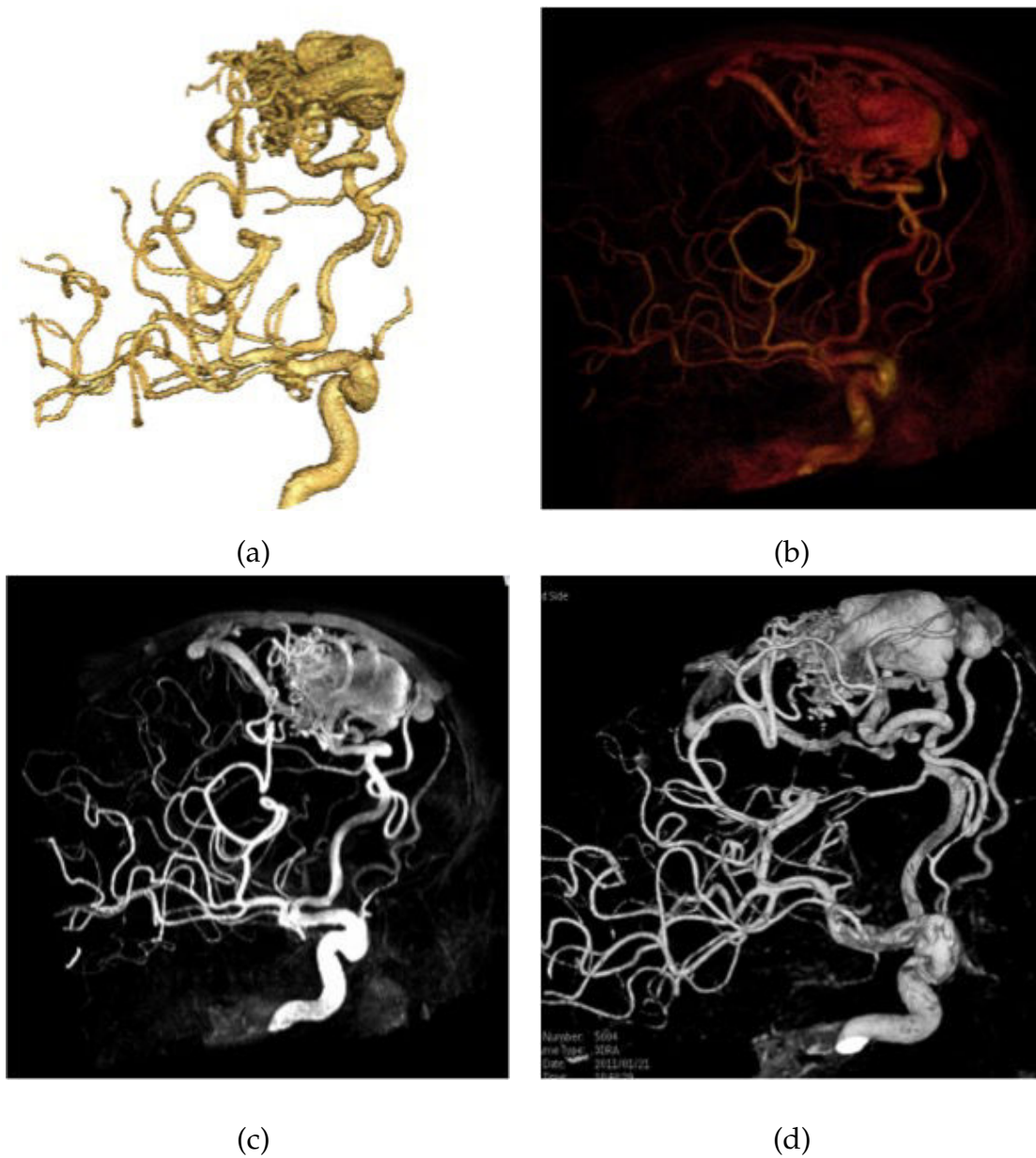


Figure 3.31: Comparison of the segmentation results of clinical data (Patient 4). (a) is the visualization of segmentation results obtained by our method, (b) and (c) are the visualization of volume rendering and 3D MIP rendering proposed by Osirix. (d) is the visualization provided by Philips.

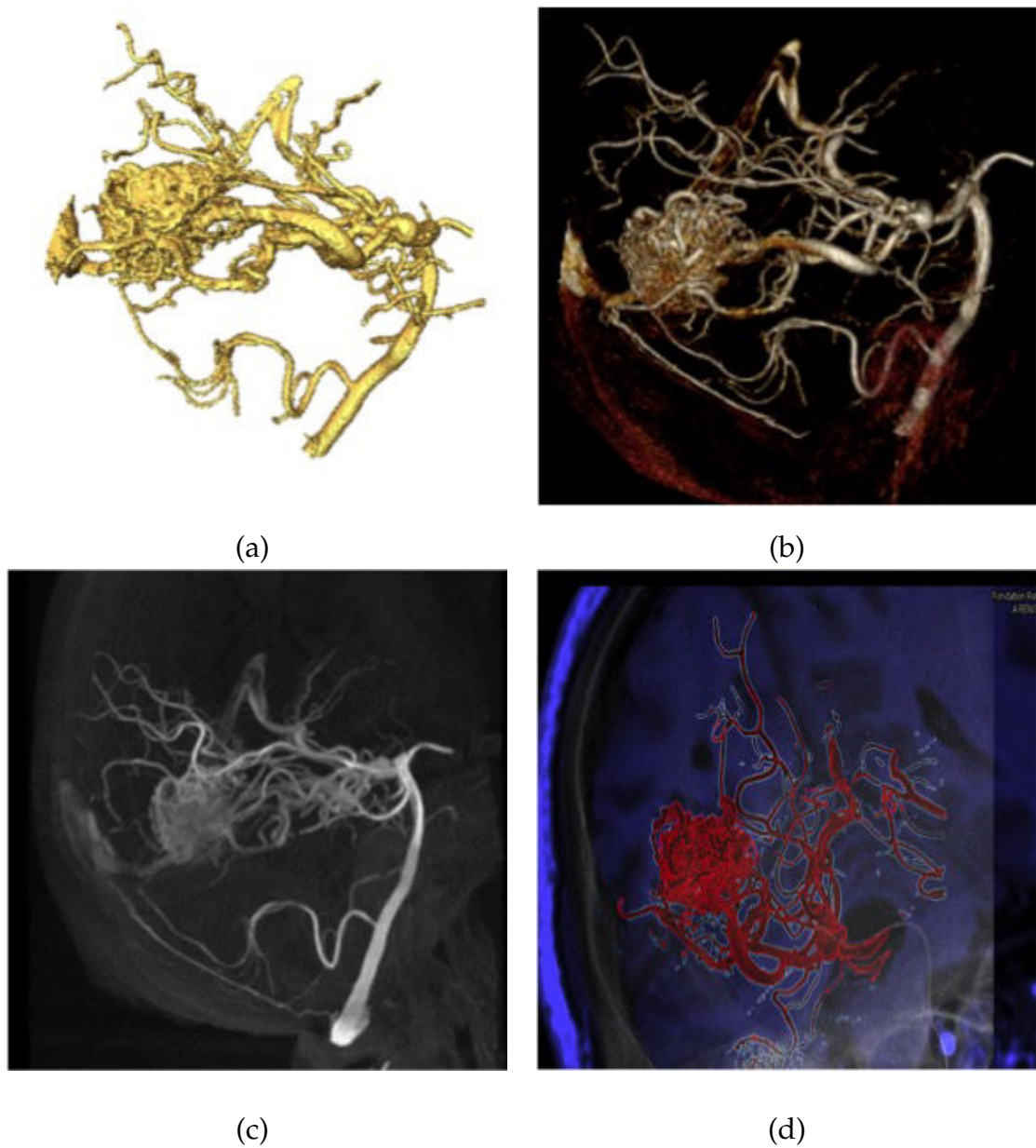


Figure 3.32: Comparison of the segmentation results of clinical data (Patient 5). (a) is the visualization of segmentation results obtained by our method, (b) and (c) are the visualization of volume rendering and 3D MIP rendering proposed by Osirix. (d) is the visualization provided by Philips, registered in MRA images

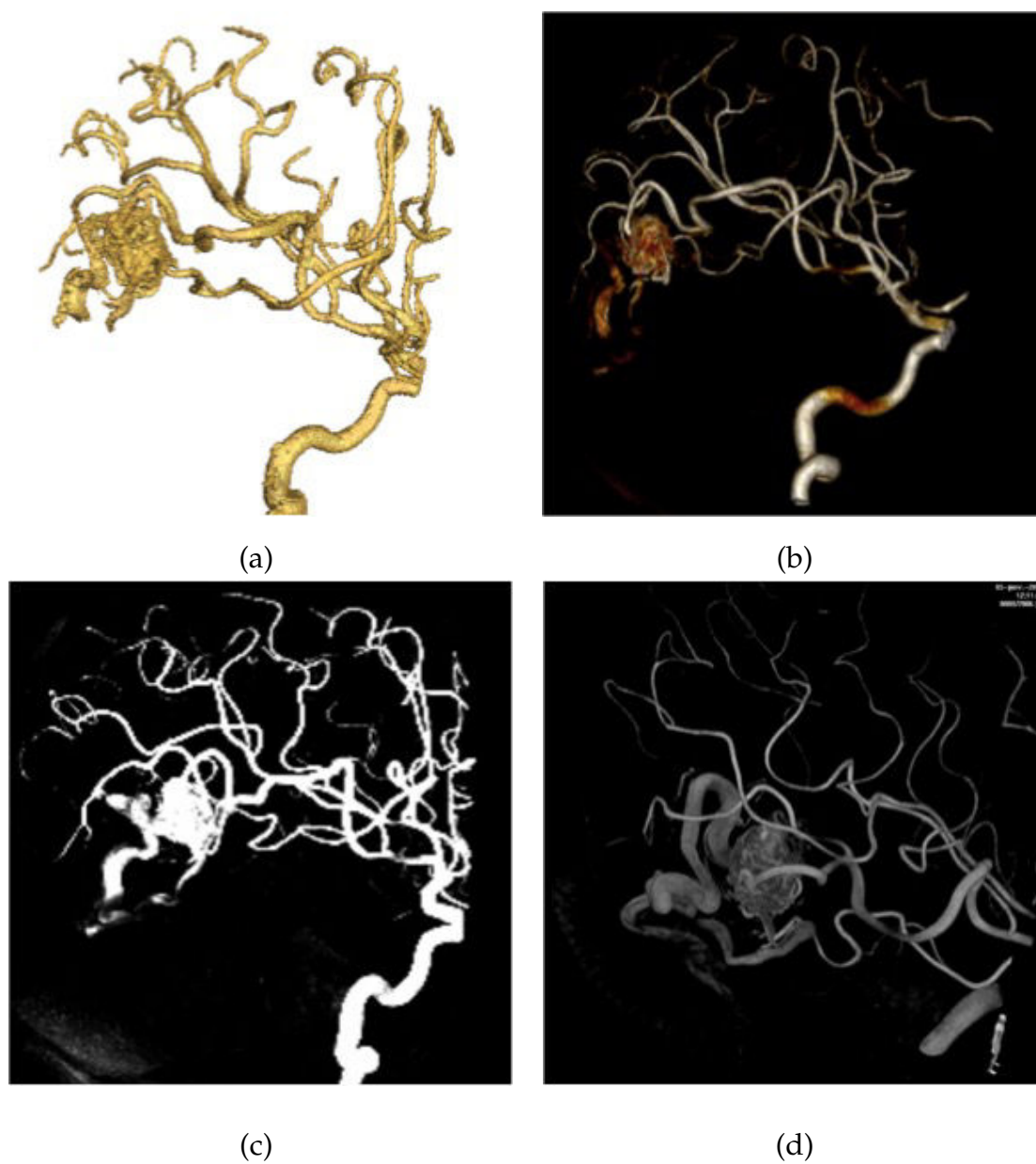


Figure 3.33: Comparison of the segmentation results of clinical data (Patient 6, series 1). (a) is the visualization of segmentation results obtained by our method, (b) and (c) are the visualization of volume rendering and 3D MIP rendering proposed by Osirix. (d) is the visualization provided by Philips.

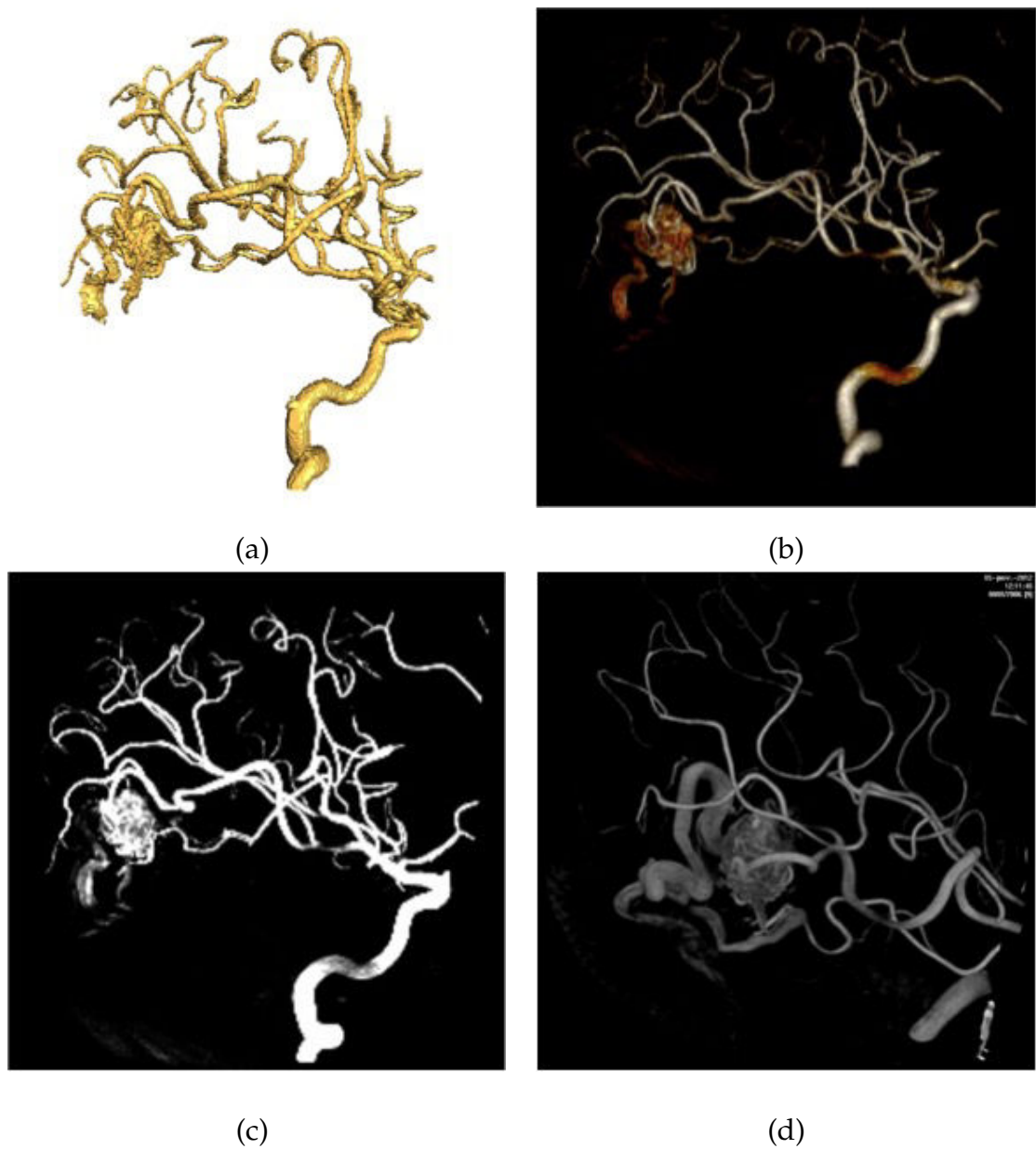


Figure 3.34: Comparison of the segmentation results of clinical data (Patient 6, series 2). (a) is the visualization of segmentation results obtained by our method, (b) and (c) are the visualization of volume rendering and 3D MIP rendering proposed by Osirix. (d) is the visualization provided by Philips.

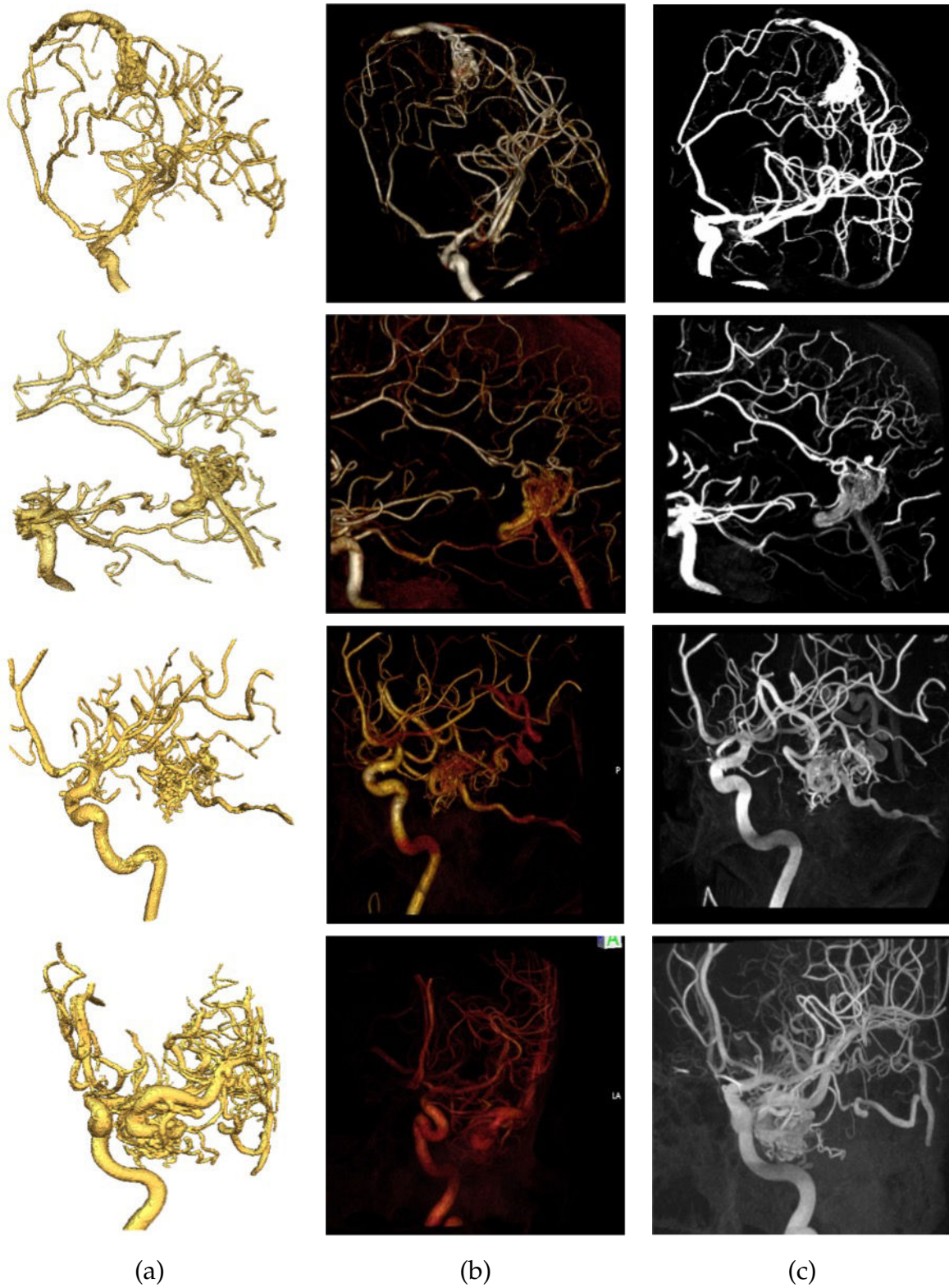


Figure 3.35: Comparison of the segmentation results of clinical data (Patient 7, 8, 9, 10). (a) is the visualization of segmentation results obtained by our method, (b) and (c) are the visualization of volume rendering and 3D MIP rendering proposed by Osirix.

### 3.7 CONCLUSION

In this chapter, we devoted to the segmentation of cerebral vessels in 3DRA images. Two segmentation methods are proposed. Firstly, a 2D slice by slice segmentation approach is developed, followed by a robust vessel tracking algorithm which can detect bifurcations and follow the trajectory of several branches derived from the same vessel. Secondly, an automated 3D vascular network segmentation method is proposed. This region growing based method has the advantage of being faster and allows three-dimensional segmentation of the whole 3DRA volume.

The obtained results on ten patients with AVM demonstrate the efficiency of our method that allows the reconstruction of a given vascular structure with a high precision. After that, we proposed a novel technique for the separation of arteries and venous networks from the the nidus. which is a new approach for assisting the clinician in understanding and treating of AVM.

Nevertheless, it is difficult to avoid the kissing vessel issue with a region growing based method, especially when the propagation criterion is an intensity-based condition. This issue hinders the further topology analysis. For this reason, more propagation criteria are expected, for instance, distance-based condition, or a local combination with level-sets [140].

To provide a good visualization and skeleton, a post-processing smoothing operation is necessary after the segmentation, such as in [141], where the topology is preserved.

## SYMBOLIC REPRESENTATION OF BRAIN VASCULAR NETWORK

---

### Contents

---

4.1	Introduction . . . . .	77
4.2	State of the art . . . . .	79
4.2.1	Topology study . . . . .	79
4.2.2	Skeletonization . . . . .	80
4.2.3	Conversion from skeleton to graph . . . . .	84
4.2.4	Topological and hierarchical analysis . . . . .	87
4.3	Proposed method . . . . .	91
4.3.1	Skeletonization . . . . .	91
4.3.2	Conversion from skeleton to graph . . . . .	91
4.3.3	Geometrical measurements . . . . .	98
4.4	Results . . . . .	99
4.4.1	Results of the synthetic vascular network . . . . .	99
4.4.2	Results of the clinical vascular network . . . . .	104
4.5	Discussion . . . . .	110

---



## 4.1 INTRODUCTION

The human intra-cerebral vasculature is complex, vast and varies greatly in human population. In addition, the entire vascular network segmentation is complicated and possesses too much information. Visualization for further analysis and interpretation of such a network is not trivial. Moreover, without post-processing, it is extremely difficult to directly extract a local part of vascular network.

Moreover, in AVM therapy planning or reporting, changes may happen between therapies. Therefore, it is highly desirable for neurosurgeons to have anatomical, geometrical, topological and haemodynamic descriptors of the vasculature. In order to obtain such descriptors, once the angiography image is segmented, the result can be used in multiple ways: visualized in 2D or 3D in order to observe only the structure of interest, analyzed as a whole or locally with geometrical, statistical, topological, and other measurements, or studied in other ways. One of the interesting ways to use the vascular network segmentation results is to create their *symbolic representation*. This representation can make an abstraction from the unnecessary local visual information and use a more global model consisting of local descriptors and identify the relationships between them. It then permits exploring the subject in a structural way through this information. A clinical method that can describe AVM in a standardized way with symbolic vocabularies and diagrams can facilitate communication between specialists and patients [142–144]. This is a very innovative and promising approach for AVM treatments as well as for clinical reporting (see [Figure 4.1](#)).

In this chapter, we describe this novel approach, which consists of transformation from segmented vascular network to a related graph representing it with different topological and geometrical descriptors. Multiple advantages can then be addressed for employing symbolic representation as a post-processing technique.

Firstly, our proposed approach provides the possibility to distinguish solely the selected part of vascular sub-trees by depiction from its graph representation. This gives us a better visualization of the structure information, thus, the information is much more simplified and obvious, and exactly what the clinicians require.

The second reason to use the proposed approach is that it allows revealing the vascular parent-child relationship. By means of topology analysis, each vessel segment in the topology model is attributed hierarchical level. The parent-child relationship is essential for both surgical planning and for guidance of endovascular procedures, allowing the surgeon to visualize the vessels connected to nidus, and thus identify the vessels that can be safely occluded. In addition, we can de-

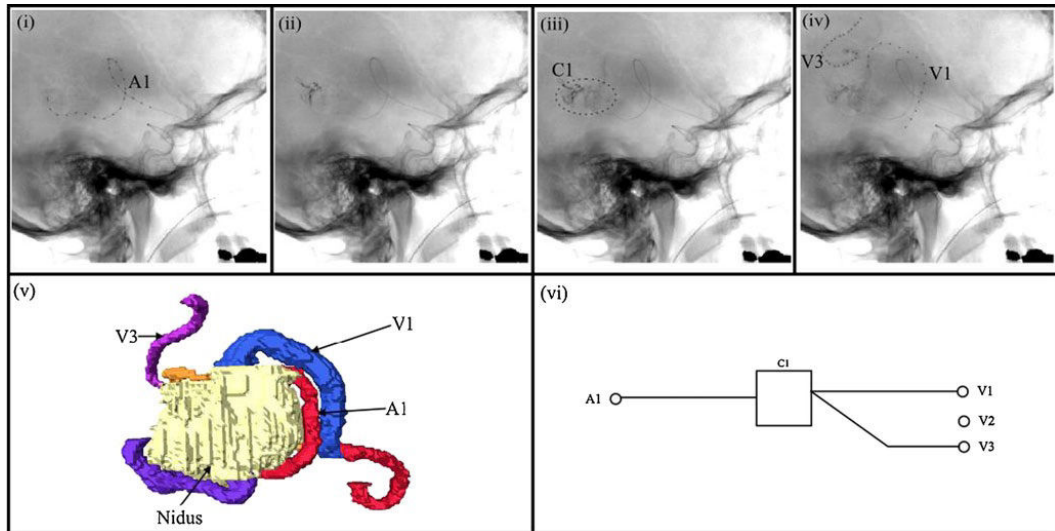


Figure 4.1: (i)-(iv) A feeding artery and two draining veins are labelled and annotated in angiography images. (v) The annotated vessels are labelled in the segmentation. (vi) The vessels and nidus are represented by the relevant component symbols and transformed into schematic diagram [143].

termine the possible navigation path between two junction points, provide their geometric properties and eventually simulate catheter motion through a 3D vascular tree, from one feeding artery to the safe occlusion points.

Thirdly, geometry features of each vascular segment are calculated by our approach, such as length, radius, volume, local direction and tortuousness. Obviously, a good knowledge of vascular parameters is of great interests for the intervention planning. In clinical practice, the features could only be measured manually on medical images, whereas the accuracy is not always guaranteed due to problem of projection overlapping and human bias. In our approach, the geometry properties are obtained automatically by combining the segmentation results, the skeleton and the corresponding graph.

To obtain the symbolic graph, our method comprises several steps:

1. skeleton extraction,
2. skeleton points classification,
3. skeleton conversion to graph,
4. reference between segmentation - skeleton - graph, both directions,
5. graph analysis and measurement.

This chapter is organized as follows: a state of the art of the related work is reviewed in [Section 4.2](#). We begin by defining the notion of topology study and present its basic properties. Then various skeletonization methods are discussed, with their strengths and shortcomings. We finally review the work of conversion from vascular skeleton to graph, addressing its necessities and advantages.

In [Section 4.3](#), we present the scheme of our approach. This technique includes a robust skeletonization method, the conversion from skeleton to graph with connectivity information, and finally the analysis of hierarchical and geometrical information.

The proposed scheme is tested on several synthetic and clinical images of vascular network. The results are evaluated in [Section 4.4](#). Finally, in [Section 4.5](#), we discuss the advantages and limitations of our approach.

## 4.2 STATE OF THE ART

### 4.2.1 *Topology study*

#### 4.2.1.1 *Digital topological classification*

According to a topological classification introduced by Bertrand [[145](#), [146](#)], each 3D point is labelled with a topological type using two descriptors in a small neighborhood, except for some junction points which need a local approach for extracting them. A brief introduction about neighbourhoods and connectivities has been presented in [Section 3.5.2.2](#).

Let us consider an object  $X$  in the real space  $\mathbb{R}^3$ , and let  $x \in X$ ,  $V(x)$  be an arbitrarily small neighbourhood of  $x$ . Two descriptors are defined as follows [[145](#)]:

$C = NC_a [X \cap N_{26}^*(x)]$ , which is the number of 26-connected components of  $X \cap N_{26}^*(x)$  26-adjacent to  $x$ .

$\bar{C} = NC_a [\bar{X} \cap N_{18}^*(x)]$ , which is the number of 6-connected components of  $\bar{X} \cap N_{18}^*(x)$  6-adjacent to  $x$ .

The topology of 3D points is proposed to be classified according to these two descriptors, which is shown in [Table 4.1](#).

This classification allows identifying the characterization of a point such as an interior, isolated, simple point and also different kinds of junctions. With this classification, some thinning algorithms are used in the following steps.

Table 4.1: Topological classification of 3D points according to the values of  $C$  and  $\bar{C}$  [145].

Type A	interior point	$\bar{C} = 0$
Type B	isolated point	$C = 0$
Type C	border point	$\bar{C} = 1, C = 1$
Type D	curves point	$\bar{C} = 1, C = 2$
Type E	curve junction	$\bar{C} = 1, C > 2$
Type F	surface point	$\bar{C} = 2, C = 1$
Type G	surface - curve junction	$\bar{C} = 2, C > 2$
Type H	surface junction	$\bar{C} > 2, C = 1$
Type H	surfaces - curve junction	$\bar{C} > 2, C \geq 2$

#### 4.2.2 Skeletonization

Skeletonization refers to a continuous process which consists in reducing objects in binary volume to a curve skeleton while preserving its topology and form. It addresses this fundamental problem by providing a synthetic representation of the object that allows, for example, greatly reducing the time of calculation in the previous analysis. It serves character recognition, study and geometry property analyses.

For vascular imaging applications, vascular tree extraction is essential for automated detection of possible pathologies. It enables neurosurgeons to pay attention to the feature details of vascular structures and makes huge datasets analysis more efficient.

The extraction of vascular skeletons can be generally grouped into two categories: (1) methods that search the optimal path between two given vessel points while minimising a cost function and (2) approaches that use thinning of segmentation results by iteratively removing simple points [147–150].

A minimal path approach is widely used to extract the centerlines [118, 151, 152]. For this, a *potential* or *step-cost function* is usually pre-defined, as well as the original point  $p_1$  and the destination point  $p_2$ . The minimal path between these two points is then derived from image related factors (intensity value, gradient) and geometry related factors (length, curvature) [87, 153]. Such methods have been turned out to be robust in the presence of noise, but it is necessary to provide the source and end points interactively, which is difficult for brain vascular networks. Therefore we concentrate in this work on thinning-based algorithm.

#### 4.2.2.1 Simple points and thinning process

As mentioned in [Section 4.2.1.1](#), a 6-face of  $\mathbb{Z}^3$  is called a *voxel*. We consider a finite set of voxels as *voxel complex* and  $\mathbb{V}^3$  the collection space of all voxel complexes [138].

Let a voxel  $x \in X$ , we call  $x$  a *simple point*, or a *simple voxel*, if its removal from or insertion to  $X$  does not alter the topology of  $X$ . The definition of this notion was introduced in [146, 154].

**Definition 1.** Let  $X \in \mathbb{V}^3$ ,  $X$  is reducible if either:

- 1)  $X$  is composed of a single voxel; or
- 2) there exists  $x \in X$ , such that  $N^*(x) \cap X$  is reducible and  $X \setminus \{x\}$  is reducible.

**Definition 2.** Let  $X \in \mathbb{V}^3$ . A voxel  $x \in X$  is simple for  $X$  if  $N^*(x) \cap X$  is reducible. If  $x \in X$  is simple for  $X$ , we say that  $X \setminus \{x\}$  is an elementary thinning of  $X$ .

The notion of a simple point permits defining thinning of a complex object. An example of thinning by removing simple voxels is presented in [Figure 4.2](#). With the [Definition 1](#) and [Definition 2](#), we can conclude that for  $x \in \{a, c, e, g\}$ ,  $x$  is a simple point for  $X$ , as  $N^*(x) \cap X$  is reducible. For example, voxel  $d$  is not a simple point for  $X$  as  $N^*(d) \cap X = \{b, c, e, g, f\}$ , the result contains two connected components ( $\{b, c\}$  and  $\{e, g, f\}$ ) and thus the topology is changed. However, voxel  $c$  is simple for  $X$  since  $N^*(c) \cap X = \{b, d\}$ , which is reducible. For this case, we say that [Figure 4.2\(b\)](#) is a thinning of [Figure 4.2\(a\)](#), or [Figure 4.2\(a\)](#) is reducible to [Figure 4.2\(b\)](#).

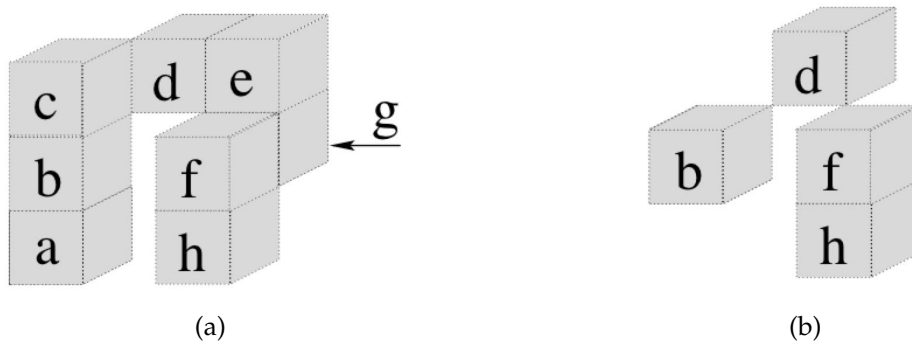


Figure 4.2: (a) A voxel complex  $X$  containing 8 voxels. (b) The thinning result by iteratively removing the simple points from  $X$  [155].

#### 4.2.2.2 Sequential thinning algorithms

Concerning the computational efficiency, thinning algorithms can be classified into (1) sequential and (2) parallel. A detailed review of thinning methods has been recently presented in [150].

In traditional sequential thinning algorithms, each iterated step consists of detecting, choosing and removing the simple voxels one by one [156–158]. Such sequential process depends on arbitrary choice and the results may not exist. To guarantee the final skeleton located in center position, the simple points have to be removed in a correct order.

Some strategies have also been proposed to remove the simple points iteratively from outside to inside. Arcelli *et al.* [156] introduced the notion of *Distance Transform (DT)* to define the erosion sequence in order to obtain a centered skeleton. Later this approach has been developed by Borgfors *et al.* [159] that determined a suitable distance metric in a DT-based voxel erosion strategy. This method makes the skeletons more robust under image rotation. Jin and Saha [160] used a fuzzy DT where a set of points are eroded during each step and therefore the computation becomes faster and more efficient.

#### 4.2.2.3 Parallel thinning algorithms

Unlike sequential thinning methods, the *parallel thinning* approach [161] allows removing a set of simple points simultaneously. It has to be noticed that removing a set of simple points in parallel adds risk to change the topology of the object. For example, the voxels  $g$  and  $f$  are both simple points for complex  $X$  in Figure 4.2. However, when removing  $g$  and  $f$  together, the complex  $X$  will be separated into 2 connected components, thus this kind of operation is not acceptable.

According to [150], the parallel thinning algorithms can be classified into three categories. The first class was introduced by Ronse *et al.* [162] in 2D with the notion of *minimal non-simple sets*. A number of conditions are designed in order to produce a set of *co-deletable* points. Other authors have developed their methods in 3D, 4D [163, 164] to perform a *fully parallel* skeletonization strategy [165]. In a similar manner, these thinning methods consist of identification, selection, and eventually elimination a set of simple voxels, independently of orientation or position in space.

The second approach is defined as *subiterative parallelization*, in which each iteration step is divided into substeps. The order of substeps is determined beforehand by either direction [161, 166] or space coordinates [167, 168]. Each subdivision

step is then devoted to the detection and elimination of one voxel that belongs to a certain direction or subfield.

The *minimal non-simple sets* strategy ensures to obtain a unique result regardless of the thinning process. The obtained skeleton remains unchanged under 90 degrees rotations, thus this method is called as *symmetric algorithm*. Symmetric algorithms produce a result that is uniquely defined: no arbitrary choice is needed. On the negative side, they give thicker skeletons.

Subiterative parallelization, also known as *asymmetric algorithm*, on the other hand, needs arbitrary choices and produces different skeleton results. An obvious advantage of asymmetric algorithms is to provide thinner skeleton. A comparison of thinning results is shown in [Figure 4.3](#).

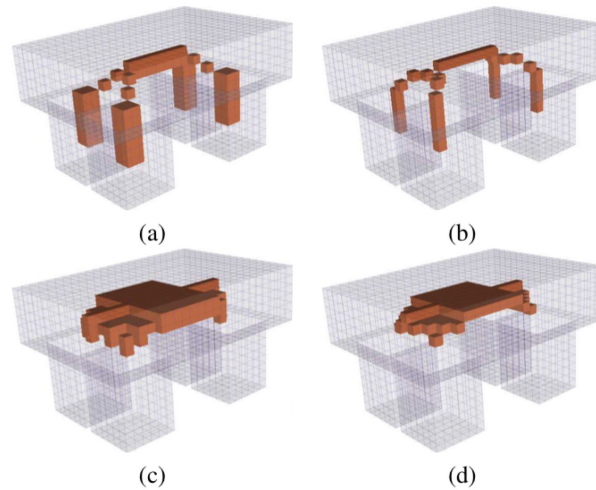


Figure 4.3: Comparison of symmetric and asymmetric results. (a) Curve skeleton, symmetric. (b) Curve skeleton, asymmetric. (c) Surface skeleton, symmetric. (d) Surface skeleton, asymmetric [155].

Apart from these two approaches, Bertrand [169] proposed the notion of *P-simple points*, which ensures topology preservation even under parallel elimination. This scheme is presented in two steps. Firstly, a set of voxels  $D$  is detected that may be considered for deletion based on geometric conditions. Secondly, all the *P-simple voxels* of  $D$  are deleted in parallel. Depending upon the propagation strategy, the proposed algorithm could be either symmetric or asymmetric. Lately, Bertrand and Couprie [155, 170] introduced the notion of *critical kernel* to perform parallel skeletonization while preserving topology. *1D isthmus-based asymmetric thinning* method [155] produces an asymmetric skeleton that is one pixel wide at all points except junctions. Moreover, this approach aims to preserve the curves

more precisely, voxels that belong to 1D *isthmuses* (meaning "piece of curve") producing a curvilinear skeleton. In order to compute curve skeleton, other voxels than the ones that are necessary for the topology preservation should be conserved. In this thinning method, the constraint set corresponds to a set of features that we want to preserve, *e.g.* curves.

#### 4.2.3 Conversion from skeleton to graph

For objects with many junctions and branches, it can be of great interest to capture the global structure (not necessarily the geometry) of the object with a graph representation by a composition of nodes and edges. In this case, for some applications, nodes of the graph can correspond to end vertices and junctions, and edges to a whole set of line segments belonging to the same branch. For other applications, an edge could be identical to a maximal straight center line segment in order to represent the geometric structure. Nodes and edges can for instance correspond to the object radius or a more sophisticated geometric measure. In any case, once a set of center lines is obtained, it should be straightforward to build a graph-based representation from it. This basically requires a mapping from centerlines to edges, and from vertices to nodes.

However, what is probably less trivial is the ability to distinguish the different components of the skeleton, *i.e.*, junction and branch points. This decomposition will draw inference to the corresponding part structure of the original object (see [Figure 4.4](#)).

Some skeleton algorithms directly classify junctions, either during thinning or as a post-processing step [145]. From the geometric algorithm class, level set methods directly identify the joints as the centroids of level-sets. Joint locations depend on the function used to define the level sets.

Here, a segment is assumed to be a piece of vasculature connecting two vessel junctions. Vessel endpoints are considered as junctions. This mapping of segments and junctions can be represented by a mathematical graph.

A graph in this context is defined as a tuple  $(V, E)$ , where  $V$  is a set of vertices and  $E$  a set of pairs of vertices forming edges. In a directed graph, the two vertices of an edge are ordered, the first vertex called the source, the second being the target. The degree of a vertex is defined as the number of edges associated with that vertex. A vascular network may be represented as a segment graph by associating each junction and each vessel end point with a vertex and each

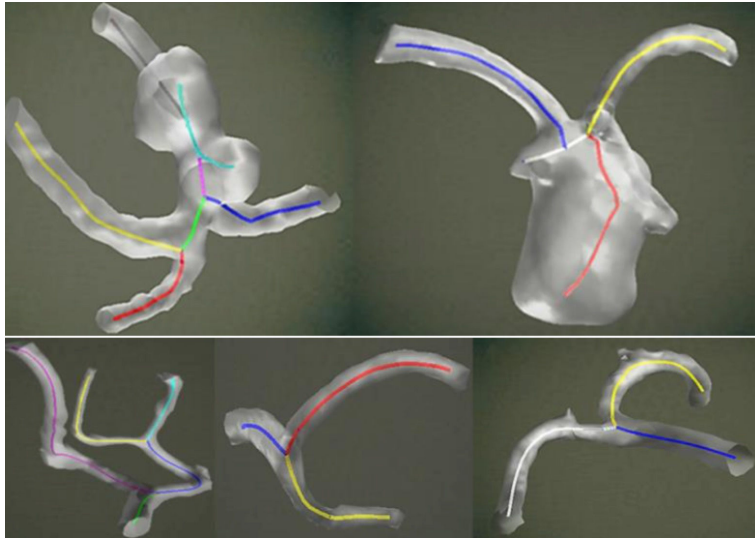


Figure 4.4: Decomposition of skeleton branches with the analysis of skeleton connectivity information [153].

segment with an edge in the graph. In Figure 4.5 an example of such a graph is illustrated.

In 1999, Bullitt *et al.* [135] introduced the notion of *symbolic representation* to analyze 3D intracerebral vascular network. They described the *minimum spanning tree* algorithm to produce directed graphs of the intracerebral vasculature from segmented MRA data. The vascular network was presumed to be composed of several "trees". From selected seed points, each tree-creation was realized by progressively attaching segmentation points that meet both distance and intensity conditions. Later, Bullitt *et al.* [113] employed this technique on the images of AVMs patients. In this work, the nidus was extracted interactively or through an automatic software tool. A visualization result is shown in Figure 4.6, in which several subtrees are extracted and are colour-coded. The results provide novel visualizations and depict the relationship of the nidus to feeding and draining vessels in three dimensions. One limitation of this work is that it is very time-consuming and requires user interaction for each step. Another drawback is that the graph information is not exploited.

Later, Grass *et al.* [171] continued to build a symbolic model to represent the vessel trees from 3DRA images. From the aspect of hierarchical relation, one structure can be separated by three levels: generations, clusters and voxels. This model is applied to determine the contrast agent propagation and calculate the *Bolus Arrival Time* (BAT) in the presence of AVM or aneurysm.

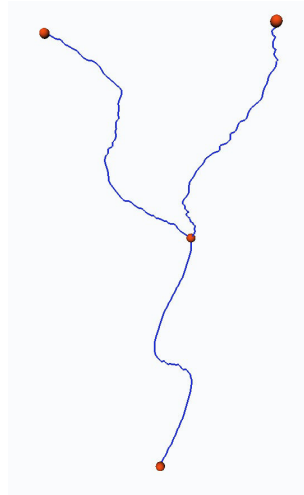


Figure 4.5: A graph based on the skeleton.

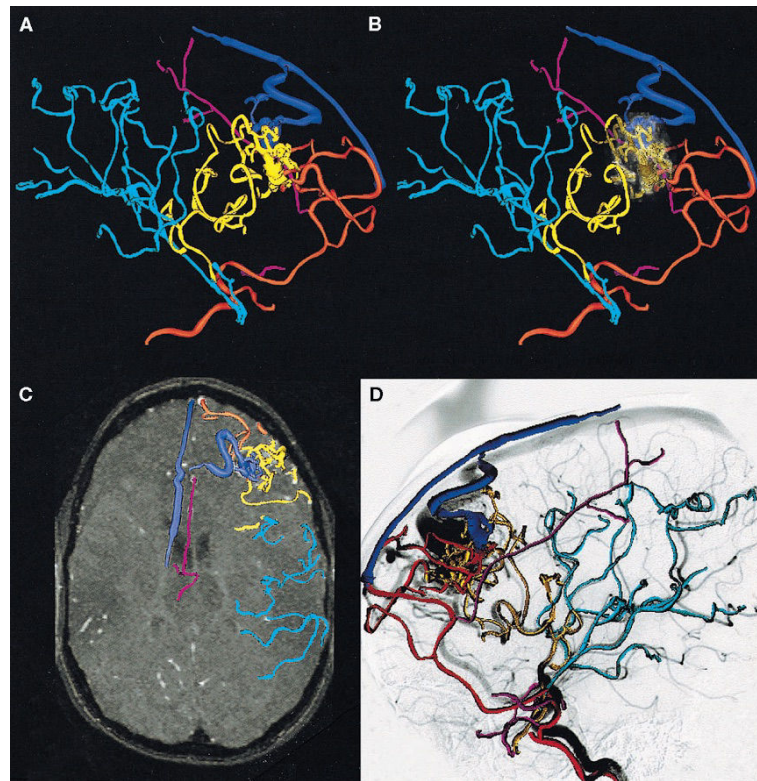


Figure 4.6: Visualization of different subtrees of intra-cerebral vasculature with AVM [113]. (A) Carotid artery circulation that supplies the AVM, with user-defined color such that supplying arteries are red or gold, veins are blue, and other subtrees are purple or cyan. (B) The same vessel tree as shown in A, with the nidus volume rendered at partial opacity. (C) Partial projection of the 3D vessel tree on an MRA slice. (D) Projection of the 3D vessel tree on a DSA image obtained from the same patient.

Subsequently, other authors completed the scheme, by preferring to employ the skeletonization before establishing the graph-based representation. For example, Qin *et al.* [172] used a direction-based parallel thinning method to obtain skeleton with one voxel width, in order to analyze cerebral vascular structure. Boskamp *et al.* [87] applied *Distance Transform* based technique to extract the skeleton of coronary arteries. Selle *et al.* [173] applied a sequential thinning algorithm to analyze liver vascular structures from CT images. By using structural properties, two directed acyclic graphs were identified which separately represented portal and hepatic vein trees. An approximation of liver segments was finally realized.

More recently, works have extended the approach of *symbolic representation* on the study of graph and quantitative description. Sankowski *et al.* [174] focused on the estimations of vascular parameters: diameter, local direction, location of terminal points and bifurcation points. Some authors show interest in the related radius to each center point [175], as well as the vessel length [117].

#### 4.2.4 Topological and hierarchical analysis

With the obtained skeleton and its graph, a hierarchy of vascular network can be created. For this purpose, a number of ordering methods have been proposed to modelize vascular network. Most of them were developed and applied to river systems. By analogy they can also be applied to vascular networks. However, the flow direction is the same for the venous network, but the arterial network it is reversed but the principles of these methods are easily applicable.

In fact, during the intervention procedure, the clinician requires determining the vessels that are connected to the AVM in order to identify the embolization path from the occlusion points to the ICA artery. This identification can be simplified and greatly aided if the vessels connected to the AVM are viewed locally by presenting at first only the closest connected branches till the first junction point (see [Figure 4.7\(b\)](#)). Then, by showing the further connected vessels to the first junction can be added till the next junction or end-points (see [Figure 4.7\(c\)](#)). The propagation can be continued so on and so forth revealing in this manner more and more of the vascular network connected to the AVM by the selected in the departure vessels (see [Figure 4.7\(d\)](#)). Additionally, the hierarchy relationship of this model allows presenting and using some other properties of vascular network information, such as blood pressure and vessel thickness.

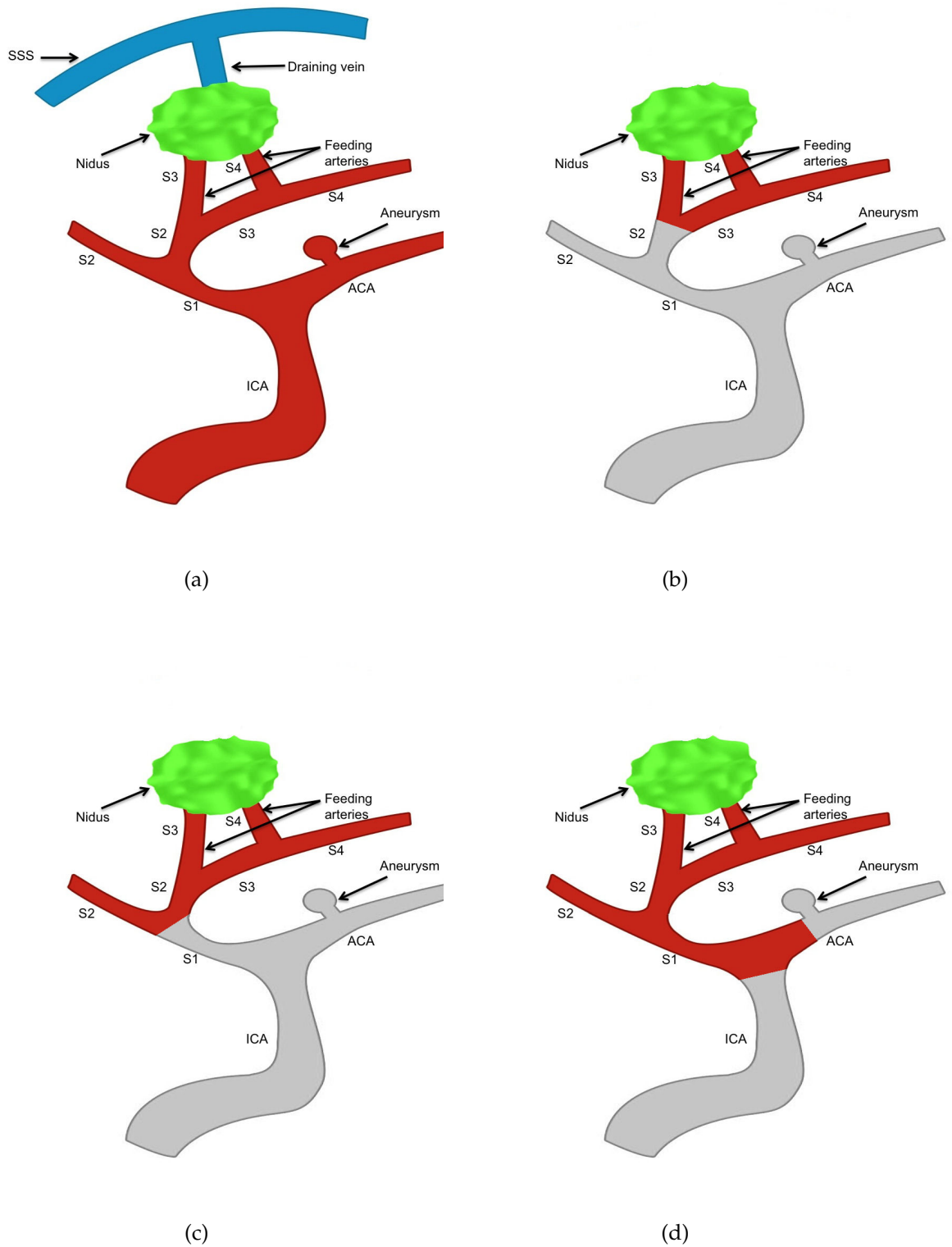


Figure 4.7: An illustration of embolization intervention planning from nidus to ICA. This planning can be facilitated by visualizing selected hierarchical levels. (a) AVM and the entire arterial network. (b) The first level vessels connected to AVM. (c) The further connected vessels of the second level. (d) The vessels from the next level.

#### 4.2.4.1 Strahler model

The most common graph hierarchical method is the *Strahler Ordering* [176], in which a directed tree is divided into three parts: root, branch and leaf. Strahler ordering begins by assigning all leaves to order 1. Then every part has its own level that is defined as follows:

$$N_{(P,L,R)} = \begin{cases} 1 & P \text{ is a leaf} \\ n + 1 & N_{(L)} = N_{(R)} = n \\ \max(N_{(L)}, N_{(R)}) & N_{(L)} \neq N_{(R)} \end{cases} \quad (4.1)$$

where  $N_{(P,L,R)}$  denotes the order of branch  $P$ , which has two children  $L$  and  $R$ .  $N_{(L)}$  and  $N_{(R)}$  denote the order of  $L$  and  $R$ .

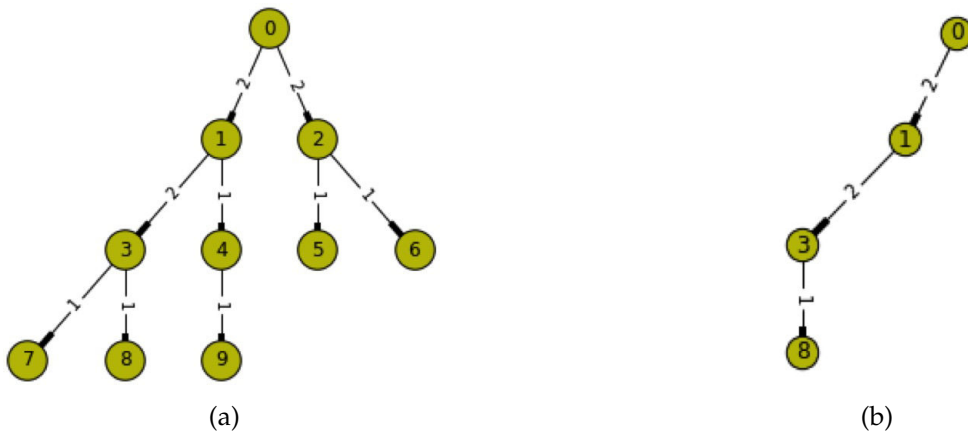


Figure 4.8: Study of the graph topology with Strahler Ordering. (a) A random directed graph with ten nodes. (b) Extracted path from node 0 to node 8.

Some works employed the Strahler modelling to analyze the vasculature hierarchical structure [134, 177].

An example of such a hierarchy can be seen in Figure 4.8(a). A directed vessel tree is obtained after the identification of the root point. According to the definition in Equation 4.1, all the terminal vessels are labelled as level 1, following vessel segments upstream, a second-order segment is formed by joining two first-order segments, a third-order segment by joining two second-order segments, and so on. The algorithm is terminated when the root is reached and all the points in the vessel tree are labelled as shown in Figure 4.8(a).

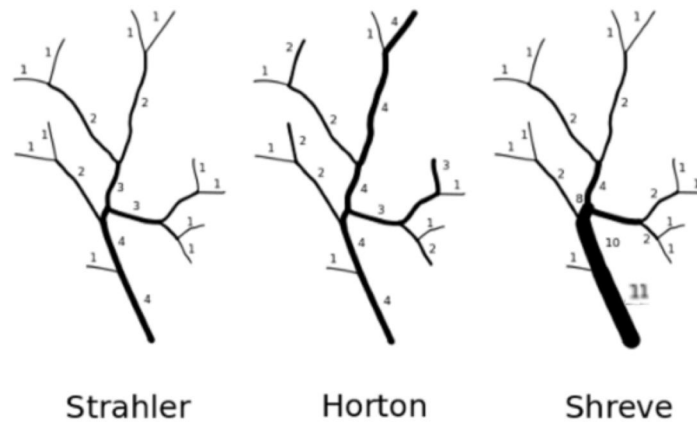


Figure 4.9: Different hierarchical models of network.

Additionally, we can easily extract the path from one point to another from the vessel hierarchy (see [Figure 4.8\(b\)](#)).

#### 4.2.4.2 Horton model

The method of Horton allows distinguishing the main branch of the stream flow from others. The algorithm is based on the hierarchization of Strahler. The branch with the highest level of Strahler is considered as the main branch. The algorithm then runs down the branches that have increased levels of Strahler or greater flow length. These branches are then labelled with the same label as the main branch. The main flow stream is then naturally obtained.

#### 4.2.4.3 Shreve model

In this scheme, the terminal branches are labelled as 1. At the junction, we sum the labels posterior branches to the junction. The anterior branch at the junction is labelled with that amount. Thus the label of a branch is the sum of its sub-branches.

A comparison of different hierarchical network models is illustrated in [Figure 4.9](#). Among these models, we have applied Strahler hierarchy model to represent our skeleton.

### 4.3 PROPOSED METHOD

In the current section, we propose an automated approach for modelling the 3D symbolic representation of cerebral vessel trees especially for the case of cerebral AVM. Binary images resulting from the segmentation of the vessel structures from 3DRA images are converted to a 3D vessel tree, which are presented by a directed graph. This description of brain vasculature provides us with its minimal topologically and geometrically correct representation, access to topological descriptors, such as hierarchies, and an easy selective visualization.

#### 4.3.1 *Skeletonization*

Here, the segmented image is skeletonized with isthmus-based parallel and asymmetric 3D thinning algorithm [155] in order to have a minimal representation of the object with its topology preservation as well as geometrical features.

To avoid topological holes, which create cycles in the skeleton, and prior to skeletonization, the segmented image is hole-closed using the algorithm described in [178].

#### 4.3.2 *Conversion from skeleton to graph*

In the previous step, we have created a skeleton of the whole cerebral vasculature. In order to construct a graph from this skeleton, the points of the skeleton should first be grouped into junctions and branches to be converted afterwards into vertices and edges.

##### 4.3.2.1 *Classification of skeleton points*

The skeleton is then decomposed into simple and terminal points, junctions and segments. In this way the complex vascular network is decomposed into individual vessel segments and is suitable for topological and quantitative analysis. Junction is a point where two or more curves meet [146]. A segment is a piece of vascular structure connecting two vessel junctions, where terminal points are considered to be junctions. Moreover, the isolated points are eliminated. This mapping of segments and junctions can be represented as a mathematical graph by associating each junction and terminal point with a vertex and each segment

with an edge in the graph. In Figure 4.10(b) an example of such a graph is illustrated.

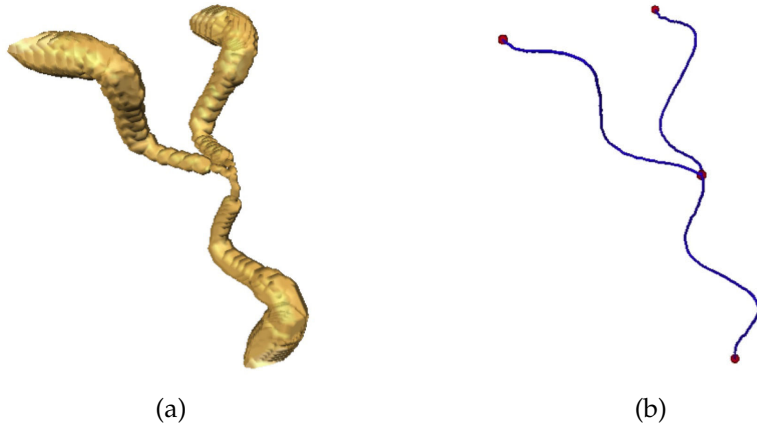


Figure 4.10: Classification of skeleton points. (a) A phantom image. (b) The skeleton of the phantom is presented by three end points (red), one junction (red) and the segments between them (blue).

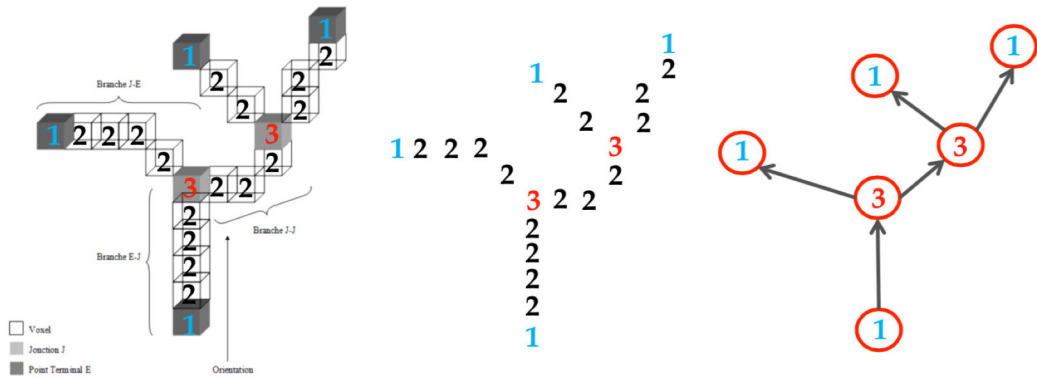


Figure 4.11: Classification of skeleton points to branch points, terminal points and junctions.

Now, it is necessary to classify the skeleton points, *i.e.*, judge one by one the skeleton voxel if it belongs to junctions, branch points or terminal points. A classic and simple method is illustrated in Figure 4.11. For each point  $x$  belonging to skeleton  $X$ , we count the number of 26-connected components of  $X \cap N_{26}^*(x)$  26 adjacent to  $x$ , and attribute this number to each each voxel.  $Im_{label}(x) = NC_a[X \cap N_{26}^*(x)]$ . Since the terminal points, branch points and junctions have,

respectively, 1, 2, 3 26-connected neighbours belonging to the skeleton, the classification of  $x$  can be obtained directly by the value of  $Im_{label}(x)$ :

$$x \text{ is a } \begin{cases} \text{terminal point} & Im_{label}(x) = 1 \\ \text{branch point} & Im_{label}(x) = 2 \\ \text{junction} & Im_{label}(x) = 3 \end{cases} \quad (4.2)$$

However, the principal ambiguity is in the identification of junctions. Based on experimental tests, we have concluded four possible skeleton classification cases, which are illustrated in [Figure 4.12](#). For each skeleton point, we calculate the number of its existing 26-connected neighbours in the skeleton. However, we suppose that other possible cases may exist whereas we have not met in our experiences.

In [Figure 4.12\(b\)](#), three skeleton points are neighbours to each other. Our algorithm enables detecting the triangle-like neighbours and choosing arbitrarily one as the junction, while reclassifying the other two "junction points" as the branch points. In [Figure 4.12\(c\)](#), there exists a center point that has four neighbours in the skeleton. We then label this point as junction and its neighbours as branch points, regardless of its neighbour number.

This proposed classification algorithm is described in [Algorithm 2](#).

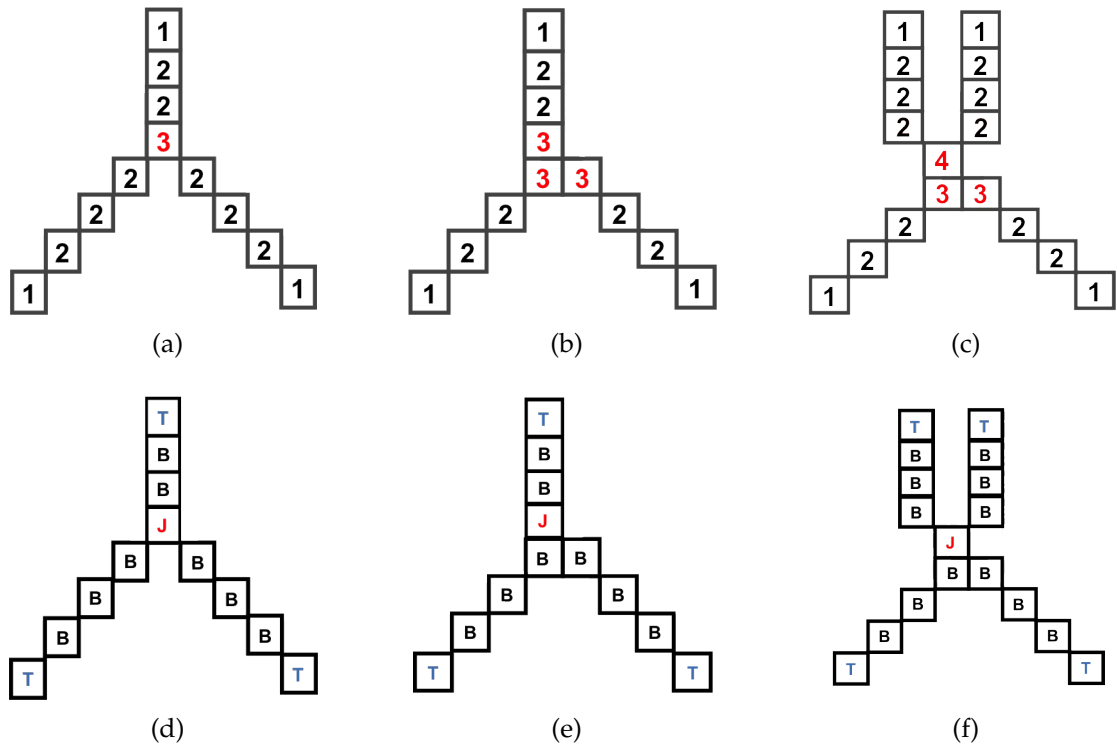


Figure 4.12: Classification of the skeleton points into three types from the number of neighbourhood. First row: three skeleton models, each voxel is labelled with the number of connected to it neighbours. Second row: type identification for each voxel: terminal points (T), branch points (B) and junctions (J).

---

**Algorithm 2** Classification of skeleton points for different cases
 

---

**Input:** A skeleton  $\mathcal{S}$ , skeleton image  $Im_{ske}$

**Output:** A label image  $Im_{label}$ , a classification image  $Im_{class}$

```

1: for all points  $p = (x, y, z) \in \mathcal{S}$  do
2:    $Im_{label}(x, y, z) = NC_a [\mathcal{S} \cap N_{26}^*(p)]$ 
3: end for
4: for all points  $p = (x, y, z) \in \mathcal{S}$  do
5:   if  $Im_{label}(p) = 4$  then
6:      $Im_{class}(p) = \mathbf{J}$  (junction point)
7:     for all points  $p_1 \in \mathcal{S} \cap N_{26}^*(p)$  do
8:        $Im_{class}(p_1) = \mathbf{B}$  (branch point)
9:     end for
10:  else if  $Im_{label}(p) = 3$  then
11:    for all points  $p_1 \in \mathcal{S} \cap N_{26}^*(p)$  do
12:      if  $\exists Im_{class}(p_1) = \mathbf{J}$  then
13:         $Im_{class}(p) = \mathbf{B}$ 
14:      else
15:         $Im_{class}(p) = \mathbf{J}$ 
16:      end if
17:    end for
18:  else if  $Im_{label}(p) = 2$  then
19:     $Im_{class}(p) = \mathbf{B}$ 
20:  else if  $Im_{label}(p) = 1$  then
21:     $Im_{class}(p) = \mathbf{T}$  (terminal point)
22:  end if
23: end for
24: return  $Im_{label}, Im_{class}$ 

```

---

#### 4.3.2.2 Construction of graph

In our implementation, the skeleton is converted to a directed graph with the obtained classification. The choice of the directed graph versus the undirected was made based on the intuitive representation of the blood flow. The creation of such a graph requires a seed point, which could be defined automatically, by selecting the vertex in the first slice, which is usually located in the terminal point of ICA.

It should be mentioned that most previous works only considered the vascular network as directed binary graphs without loops [117, 135, 174]. This assumption presents many limitations for clinical purposes. Firstly, vessels might appear as tangent due to the limits of image resolution and the presence of multiple vessels in the same region of space, known as "kissing vessel" [179]. Vascular networks can also contain loops. Even the 3 major circulatory groups are connected differently in different patients via the circle of Willis at the base of the skull [135]. It is therefore very difficult to analyze such vascular networks. In our work we use four graph models (see Figure 4.14). The first model is the most simple and classic, known as directed binary graph (see Figure 4.14(a)). Another existing model in cerebral vascular network is shown in Figure 4.14(d), where three or more vessel segments are derived from one same junctions. Besides, Figure 4.14(b) and Figure 4.14(c) describe the other two models observed in 3DRA images, with the presence of loop. We address that in the study of AVM network, especially only for the local arterial network derived from ICA. Such loops are caused by an insufficient resolution in image acquisition (Figure 4.13) or erroneous segmentation.

Starting from the seed vertex, the segment skeleton branch is followed voxel by voxel until the next junction is reached. The algorithm of creating graph is presented in Algorithm 3. This algorithm is applicable for all the four models in Figure 4.14, where the results are shown in Section 4.4. Thanks to the labelled image obtained during the classification procedure, a pre-knowledge can be used to estimate the number of sub-branches for each new junction. The vertices and edges are counted and numbered while constructing the graph.

In addition, the graph-constructing procedure allows creating a correspondence between the graph segments and vessel skeleton branches, which makes it possible to decompose the skeleton branches. Figure 4.15 illustrates an example that creates a directed graph from a phantom image.

Furthermore, we have also built a correspondence between the segmentation and the skeleton, and thus, the graph. The partitioning was performed automatically by calculating the *Euclidean Distances* between every segmented voxel and

its surrounding skeleton voxels. For a given segmented voxel, we searched for the nearest voxel belonging to the skeleton. Afterwards the segmented voxel was attributed the same label as the nearest skeleton voxel.

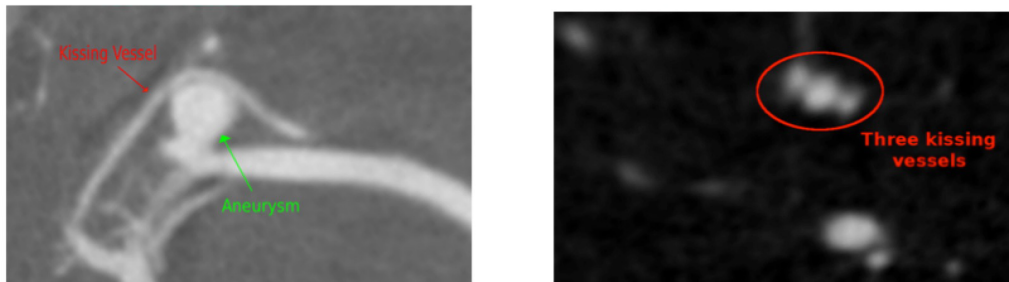


Figure 4.13: Two cut planes through 3DRA data exhibiting the kissing vessel issue: (left) A vessel runs along an aneurysm. (right) Three locally tangent vessels [179].

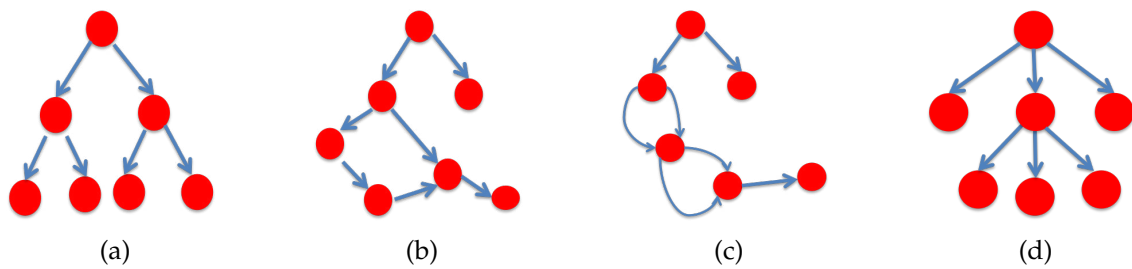


Figure 4.14: Several possible graph models of vascular skeleton network. (a) Directed binary graph. (b) Graph with the presence of loop. (c) Multi-edges graph. (d) Multi-children graph.

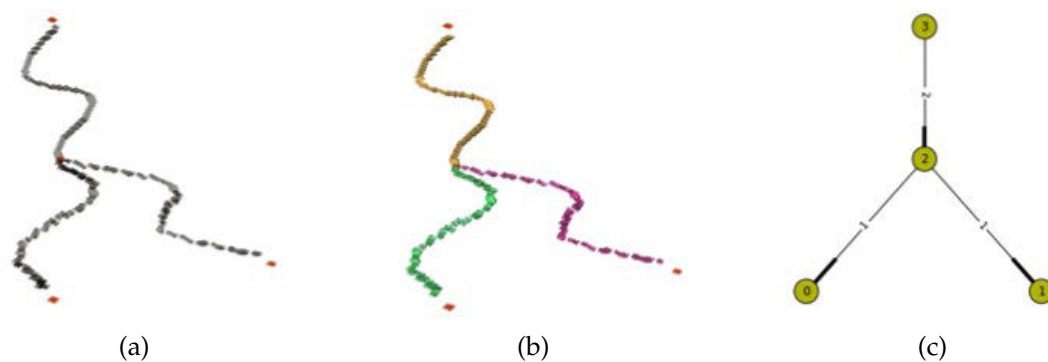


Figure 4.15: Construction of graph from the skeleton of phantom image. (a) Skeleton. (b) Decomposition of skeleton branches. (c) The constructed graph.

The direct reference between the segmented image, skeleton image and graph facilitates the feature extraction, vessel network navigation and visualization. Geometrical measurements are presented in the following section.

#### 4.3.3 Geometrical measurements

The geometrical features of vascular network are of great importance to clinicians. Here, we are interested in the following vessel parameters: junction location, vessel and/or its segment length, volume, tortuosity, mean and local radius, and local direction.

##### 4.3.3.1 Vessel length and volume

When constructing the graph, we have noted source and destination junctions of each skeleton segment. The coordinates of the two junctions define the location of the vessel branch. Since our skeleton is always one-voxel width, the length of a given vessel branch can be obtained with the skeleton points in the branch and the image resolution:

$$Length(i) = Nb_{skeleton}(i) \times r \quad (4.3)$$

where  $i$  denotes the index number of the given vessel,  $r$  denotes the image resolution.

We can also calculate branch volume by counting the voxels number belonging to this branch as:

$$Volume(i) = Nb_{seg}(i) \times r \quad (4.4)$$

##### 4.3.3.2 Vessel radius

Since a vessel branch can be approximated as cylinder with its volume and length, the maximum radius is calculated as:

$$Radius(i) = \sqrt{\frac{Volume(i)}{\pi \times Length(i)}} \quad (4.5)$$

The term of *instant radius* represents the radius at each skeleton point. Here we adopt the medial axis approach explained in [174], where a maximal ball  $B_r(x)$  of radius  $r$  and with center  $X$  is a set of points  $y \in R_n$  such that  $d(x, y) < r$ , where  $d$

is a distance, *e.g.* Euclidean. A maximal ball  $B_{r_{max}}$  of radius  $r$  for a set  $X$  is a ball that is contained in  $X$  so that there is no other ball containing it at the same time, an example is illustrated in [Figure 4.16](#).

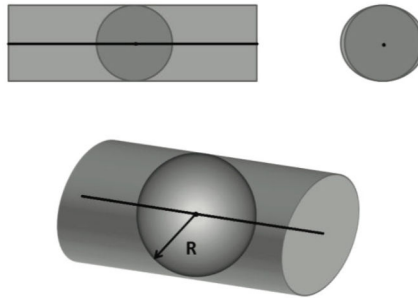


Figure 4.16: Diameter estimation with median axis [174].

#### 4.3.3.3 Tortuousness

As for the *tortuousness* of a vessel branch, we used the following formula:

$$Tor(i) = \frac{Length(i)}{D_i(j_1, j_2)} \quad (4.6)$$

where  $D_i(j_1, j_2)$  denotes the distance between the two junctions of branch  $i$ .

## 4.4 RESULTS

In this section, we applied the proposed method on both synthetic and real clinical vascular network images. To prove the robustness of our method, various types of synthetic images have been tested and validated with the ground truth.

### 4.4.1 Results of the synthetic vascular network

The synthetic vascular network was generated by a software *VascuSynth* [180, 181]. In the first step, we have tested our method on a simple synthetic image. The result is shown in [Figure 4.17](#).

We started with the extraction of centerline (see [Figure 4.17\(b\)](#)). The centerline presents very few spurious branches and a rather curvilinear and smooth overall appearance. With the topology study, different skeleton parts, such as end points, junctions and segments, were extracted. This offers insight into vessel distribu-

tion connectivity and permits the vascular tree hierarchy analysis. Then we have managed to construct the related graph, both in 3D (see [Figure 4.17\(c\)](#)) and 2D (see [Figure 4.17\(d\)](#)). In 3D graph, all the vertices occupy the same coordinates as the junctions, whereas all the segment branches are replaced by straight lines. The 2D directed graph enables us to manipulate directly on it. We have also applied the Strahler model on the 2D graph, which permits demonstrating the parent-children relations more clearly.

By seeking for the graph-related edge of each segmented voxel, we decompose the vascular network into branches. In this manner, each branch is extracted and separated from the vascular tree. The branch decomposition is shown in [Figure 4.17\(e\)](#), where each vessel branch is displayed by a user-defined color. Visually the mapping reveals a good agreement with the ground truth. It can be seen that in the bifurcation locations, due to the distance calculation from the branches to junctions, the results of the vessel segment selection are arbitrary, as in [Figure 4.17\(f\)](#). Aiming to illustrate the hierarchy results, the vessel tree is labelled according to its Strahler level. In [Figure 4.17\(g\)](#), all the terminal branches (level 1) are displayed with blue, while the principal branches were shown in green (level 2) and red (level 3).

An evident advantage of our method is to define the navigation path from one junction to another, which allows preserving only the "interesting branches" from the vessel tree. [Figure 4.17\(h\)](#) and [Figure 4.17\(i\)](#) show obtained navigation path from root (junction 6) to two different terminal points (junction 8 and 10). For a directed graph, the path from one depart point to an arrival point is unique. Our method can successfully detect all the segment branches in this path, which regroups the navigation path results.

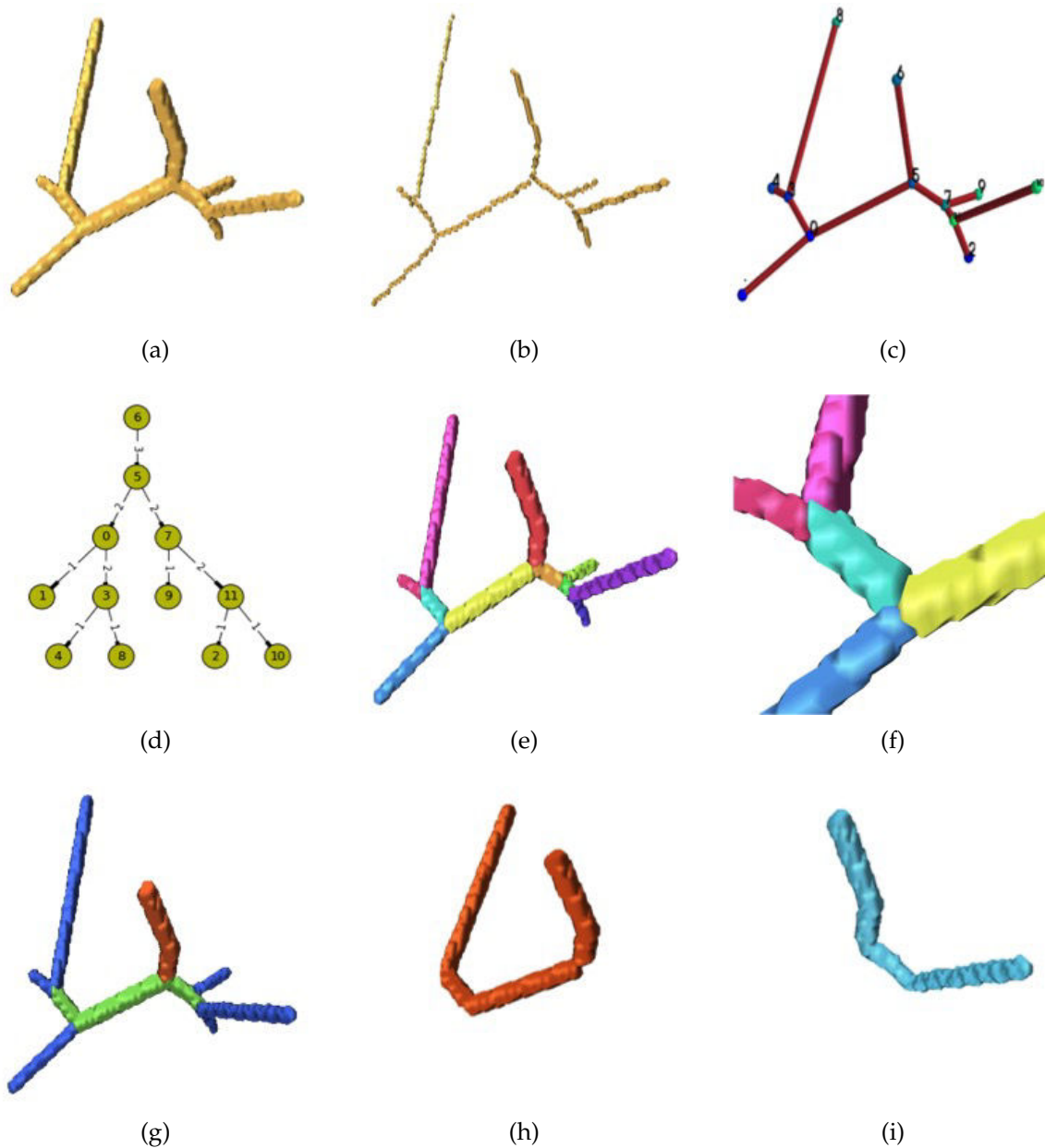


Figure 4.17: The symbolic representation results on a synthetic vascular tree. (a) The vascular tree. (b) The curvilinear skeleton with Isthmus-based thinning. (c) 3D graph representation of the vascular tree. (d) 2D graph representation with Strahler level. (e) The decomposition of branches. (f) The decomposition in bifurcations position. (g) Vascular tree colour representation of the Strahler orders. (h) The navigation path from junction 6 to 8. (i) The navigation path from junction 6 to 10.

**Algorithm 3** Graph construction from the classification**Input:** A label image  $Im_{label}$ , a classification image  $Im_{class}$ , a root point  $p_{root}$ **Output:** A directed graph  $G = (V, E)$ 


---

```

1: for all points  $p = (x, y, z) \in Im_{class}$  do
2:    $p \leftarrow untreated$ 
3:   if  $Im_{class}(p) = J \cup T$  then
4:      $V \leftarrow V \cup \{p\}$ 
5:   end if
6: end for
7:  $p_{starts} \leftarrow p_{root}$ 
8:  $p_{root} \leftarrow treated$ 
9: while not all points  $\in V$  are treated do
10:   $p_{nextstarts} = \emptyset$ 
11:  for all  $p_{start} \in p_{starts}$  do
12:     $nb_{adj} = nb(p_i) \mid \{p_i \in N_{26}^*(p_{start}) \cap (p_i \text{ is untreated})\}$ 
13:    for  $i = 1 \rightarrow nb_{adj}$  do
14:       $found_{verte} \leftarrow False$ 
15:      while  $found_{vertex} = False$  do
16:        for all  $p \in N_{26}^*(p_{start})$  do
17:          if  $(p \text{ is untreated}) \cap (p \ni V)$  then
18:             $edges(i) = edges(i) \cup \{p\}$ 
19:             $p \leftarrow treated$ 
20:             $p_{start} \leftarrow p$ 
21:            break
22:          else if  $(p \text{ is untreated}) \cap (p \in V)$  then
23:             $p_{nextstarts} \leftarrow p_{nextstarts} \cup \{p\}$ 
24:             $p \leftarrow treated$ 
25:             $found_{vertex} \leftarrow True$ 
26:             $E \leftarrow (p_{start}, p)$ 
27:            break
28:          end if
29:        end for
30:      end while
31:    end for
32:  end for
33:   $p_{starts} \leftarrow p_{nextstarts}$ 
34: end while
35: return  $G$ 

```

---

The geometrical features of the vascular network have been analyzed in the next step (see [Figure 4.19](#)). To facilitate this study, the branches and junctions are numbered. For each branch segment, the proposed method calculates automatically the two connection junctions, the volume, mean radius and length. The instant radius related to skeleton points is also computed with the medial axis method described in [Section 4.3.3](#). For the synthetic image, instant radius varies from 1 to 3 voxels and the results are illustrated in [Figure 4.19\(c\)](#).

For the synthetic images of vascular trees simulated by [180], the ground truth of hierarchical relations and geometrical parameters (only junction locations and mean vessel radius) are available. The obtained hierarchical relations have been verified and are identical with the ground truth.

We evaluate the precision of junction positions with  $D_i$  as defined in [Equation 4.7](#), where  $(x(i), y(i), z(i))$  and  $(\bar{x}(i), \bar{y}(i), \bar{z}(i))$  denote separately the obtained and real coordinates of junction  $J_i$ . For the 12 junctions detected in [Figure 4.17\(a\)](#),  $D_i$  has a maximum value of 5 while the mean value equals to 3.8.

$$D_i = |x(i) - \bar{x}(i)| + |y(i) - \bar{y}(i)| + |z(i) - \bar{z}(i)| \quad (4.7)$$

A comparison of mean radius for vessel branches in [Figure 4.17\(a\)](#) is shown in [Figure 4.18](#). The obtained vessel radius is always greater than the real one, the difference variance is  $-0.3 \pm 0.3$  (1.2 to 2.3 voxels). It is due to the fact that the mean radius is estimated based on cylinder model (see [Section 4.3.3.2](#)).

As mentioned above, our method allows dealing with particular cases of vascular network. In fact, the vascular networks are not always in tree-like form, but rather connected network with loops. The image acquisition and segmentation may lead to extra loops. Here, we present two such examples. [Figure 4.20](#) presents two synthetic images with loops and the related 3D-graph representation. [Figure 4.21](#) is an image with multi-edges, *i.e.*, two or more edges exist between two vertices.

For such images, our method provide the graph representation as well. The geometrical parameters can be correctly analyzed in the same way. In [Figure 4.21](#), the multi-edges between junction 2 and 5 are converged in 3D representation, yet it is clearly demonstrated by 2D graph representation.

The existence of loop hinders us from extracting the navigation path between two junctions and the hierarchical ordering. To solve this problem, Han *et al.* proposed [182] a topology-correction approach. Since the vessel network topology

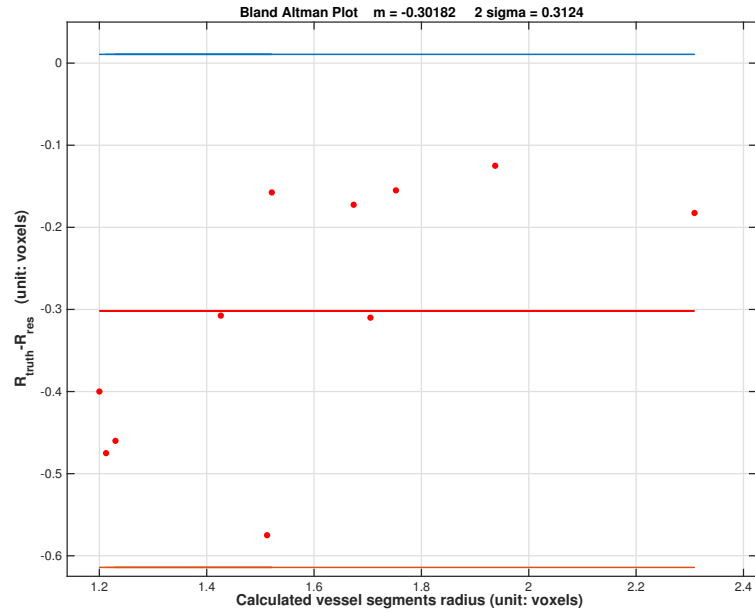


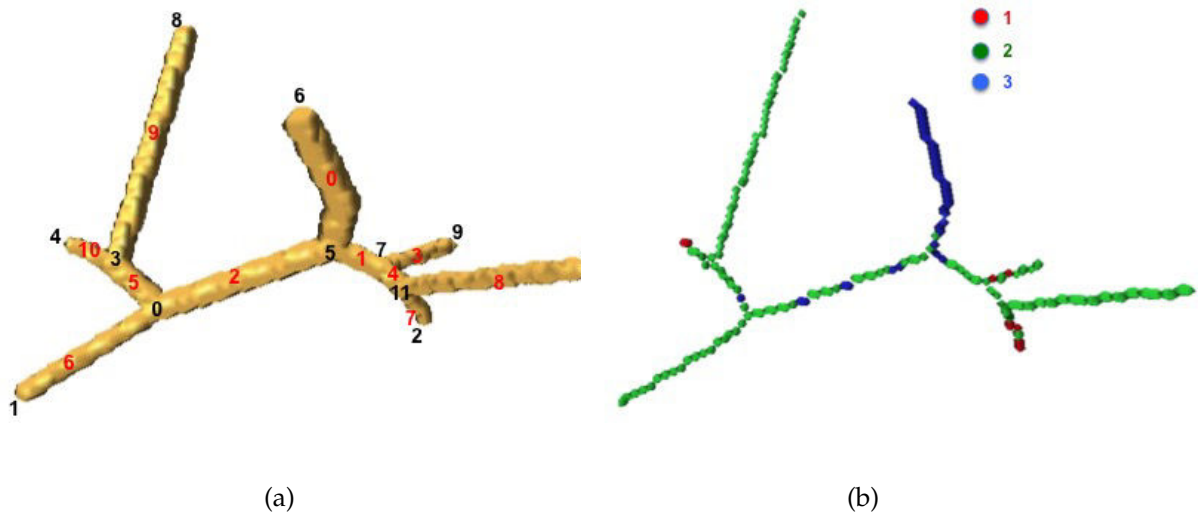
Figure 4.18: Bland Altman plot of obtained and real mean radius.

is complex, it is not obvious to correct the topology automatically, so the user interaction here is highly desirable. Depending on clinical experience or other image modalities, the neuroradiologist can choose certain edges to be eliminated, of which the related vessel branches are of little importance.

#### 4.4.2 Results of the clinical vascular network

In clinical approach, the superselective catheterization [183] is carried out in 2D angiogram under 3D Roadmap navigation, by tracing the feeding arteries in different colours (see Figure 4.23(a)). The analysis of the 3D reconstructed region around the nidus allowed identifying the principal feeding arteries and draining veins (see Figure 4.23(b)). This way, our segmentation provides a better vascular network visualization containing 3D information that can aid in embolization planning.

Furthermore, the extraction of centerline was performed (see Figure 4.23(c)). The centerline presents very few spurious branches and a rather curvilinear and smooth overall appearance. With the topology study, different skeleton parts, such as end points, junctions and segments, were extracted (see Figure 4.23(d)).



Branch number	0	1	2	3	4	5	6	7	8	9	10
Junction number (source-> destination)	6->5	5->7	5->0	7->9	7->11	0->3	0->1	11->2	11->10	3->8	3->4
Volume (voxels)	625	125	522	92	41	135	226	66	310	600	60
Mean radius (voxels)	2.82	2.23	2.43	1.80	2.56	2.32	2.06	1.45	1.85	2.16	1.95
Length (voxels)	25	8	28	9	2	8	17	10	29	41	5

(c)

Figure 4.19: Geometrical features of synthetic vascular tree. (a) The junctions and branches are numbered. (b) The related instant radius of each skeleton point. (c) Some quantitative results of the geometrical features.

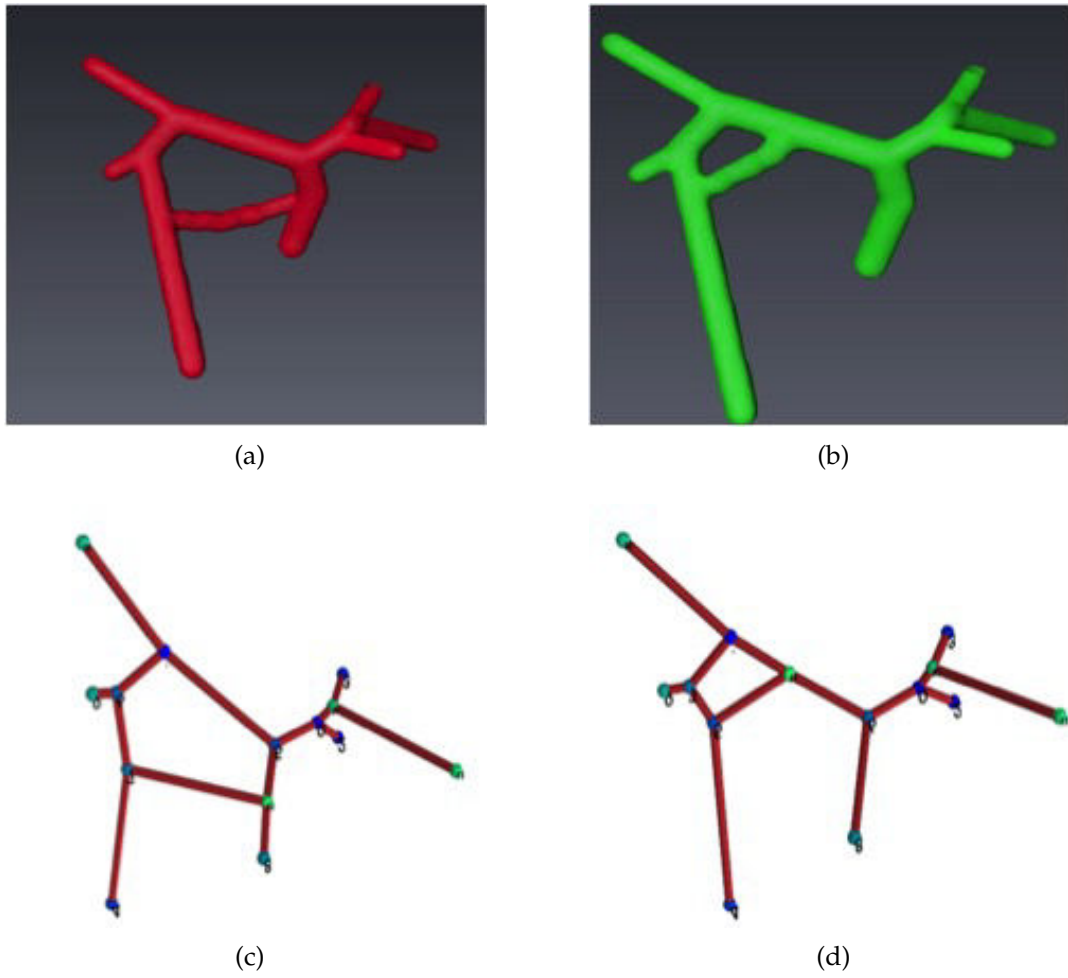


Figure 4.20: First row: two synthetic vascular images with the presence of loop. Second row: the related 3D graph representations.

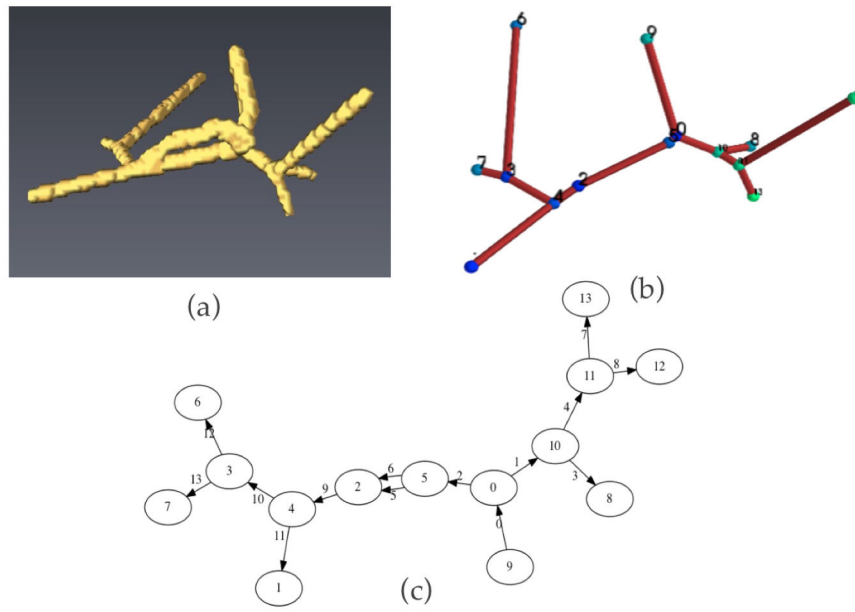


Figure 4.21: An example of synthetic vascular image with multi-edges and its graph representation in 2D and 3D.

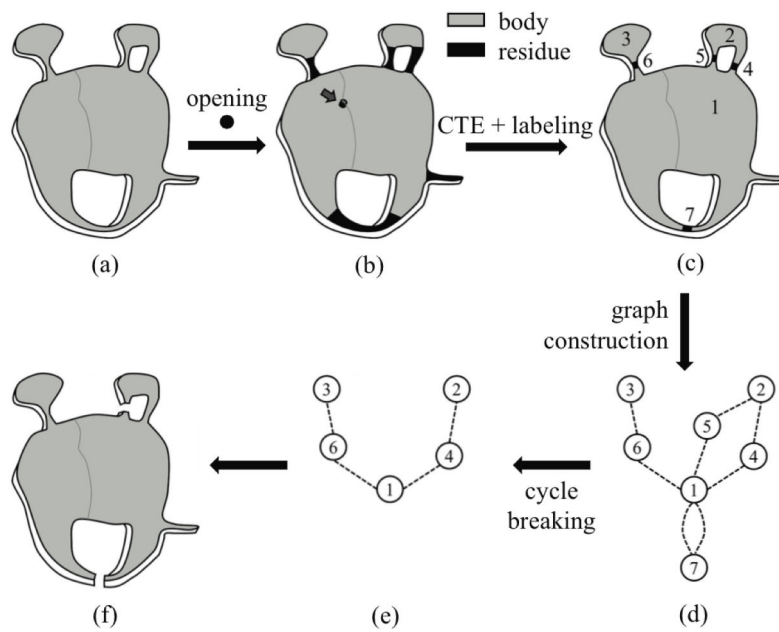


Figure 4.22: Illustration of topological correction [182].

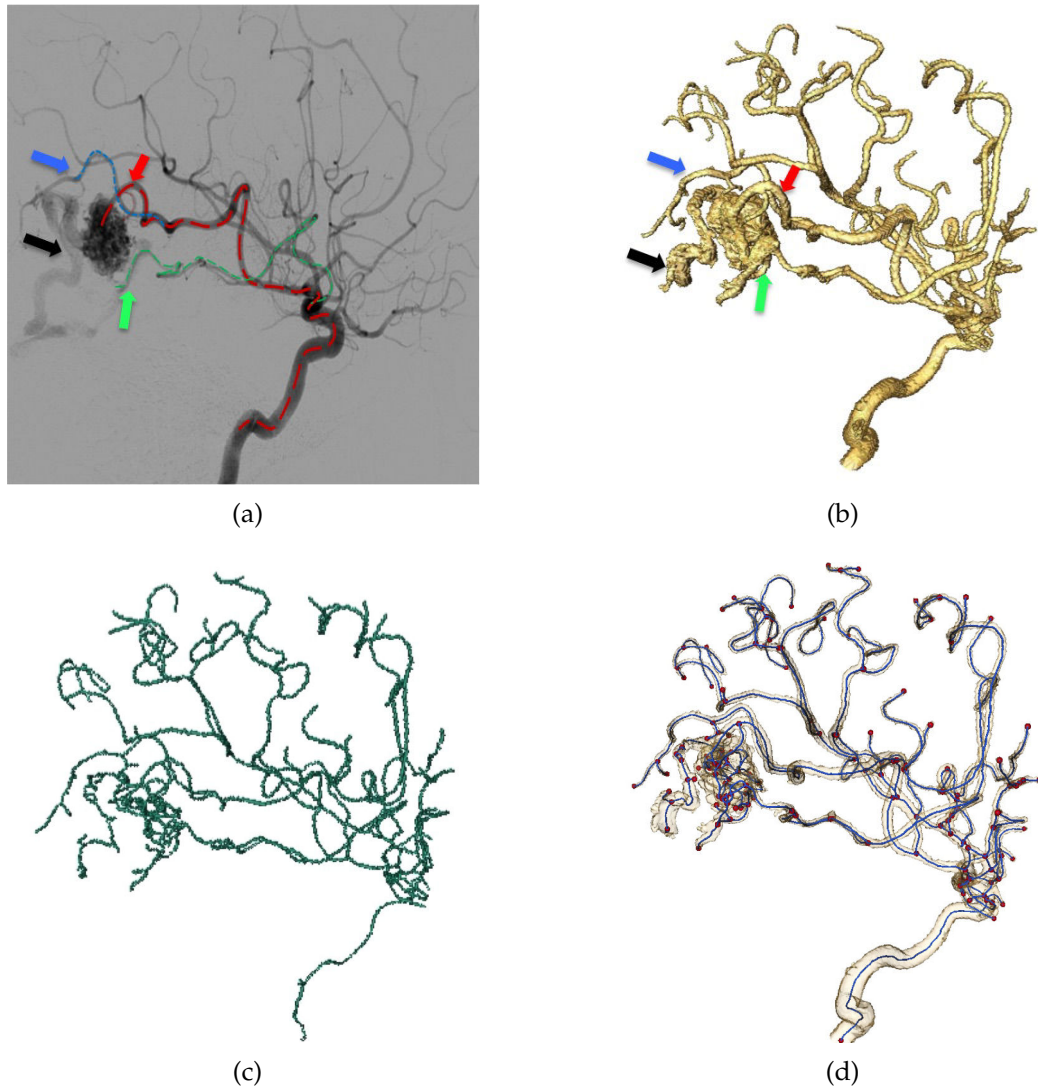


Figure 4.23: Analysis of vessel tree topology. (a) Angiogram of an AVM: clinician coloured three principal arterial feeders in red, green and blue and the draining vein in black. (b) Surface reconstruction of our segmentation. (c) Skeleton of the segmentation. (d) Skeleton graph and its parts (nodes stand for junctions and end points, segments for branches).

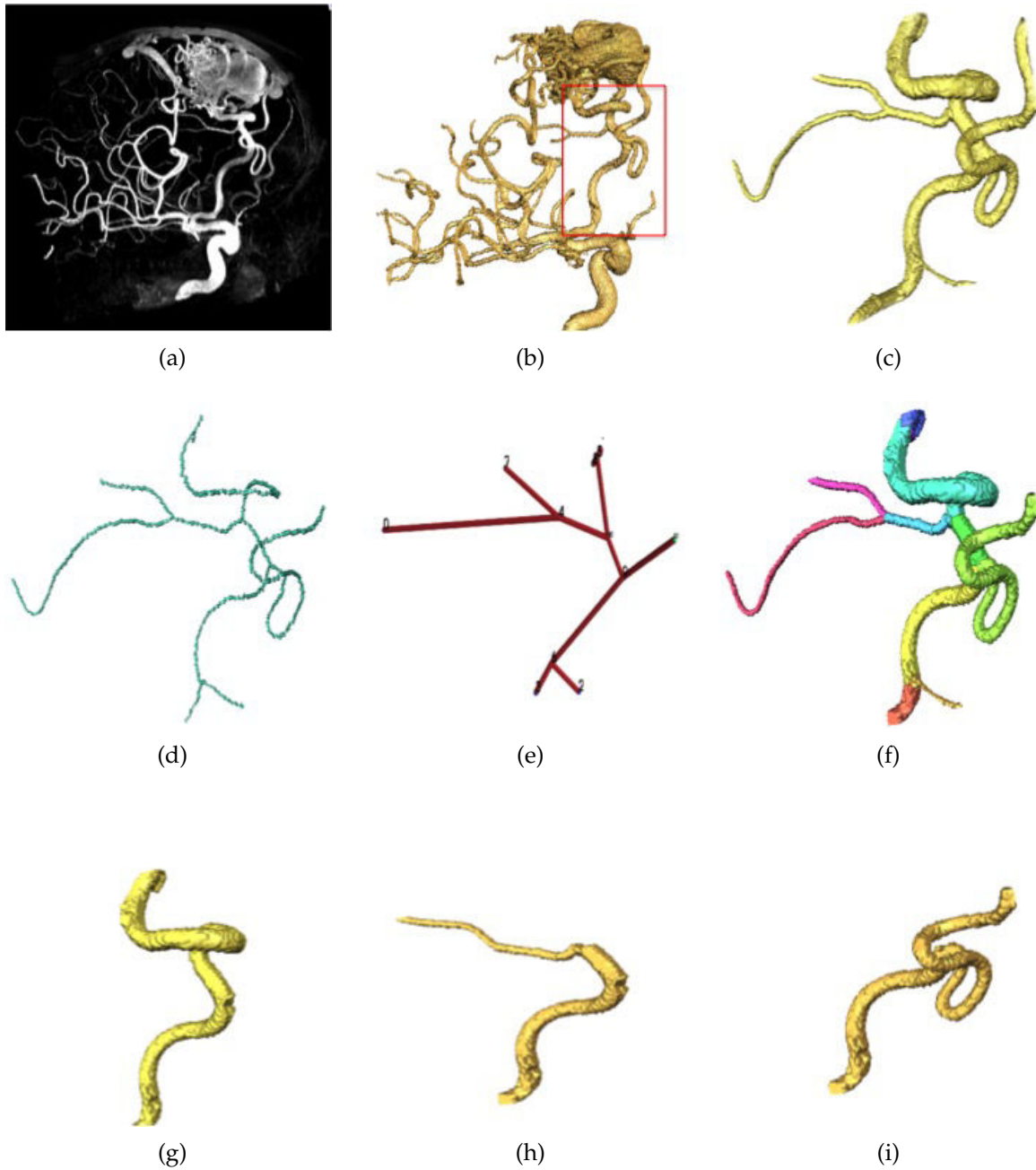


Figure 4.24: Selective visualization of vascular tree. (a) The MIP image of the vascular network. (b) The segmentation result of same patient. (c) Sub-tree connected to the nidus. (d) The skeleton of the sub-tree. (e) 3D graph of sub-tree. (f) The decomposition into vessel branches. (g, h, i) Three paths of the nidus supplying arteries till the root of the vessel.

Another clinical image results are shown in [Figure 4.24](#). From a total of 256 slices of an image, we chose the 160 ones closest to the nidus. We have applied the same analysis approach as introduced previously in [Section 4.4.1](#) to extract the skeleton and create the symbolic graph of the sub-tree (see [Figure 4.24\(e\)](#)). The decomposition is then performed as shown in [Figure 4.24\(f\)](#). Starting from the root point located in ACA (Anterior Cerebral Artery), we extracted the three arteries that possibly supplied the nidus ([Figure 4.24\(g\)](#) to [Figure 4.24\(i\)](#)).

In addition, the vessel geometrical measures were computed, as shown in [Table 4.2](#). With the knowledge of associated resolution, these parameters can be presented by either voxels or metric values. By evaluating features such as radius and length, our method enables identifying the principal artery supplying the nidus. This proposed artery is extracted with the obtained graph. The result is illustrated in [Figure 4.25](#) and validated clinically. When rotating the 3D image of constructed artery, we can easily determine a suitable orientation to judge the result. In [Figure 4.25](#), the trajectory of principal feeding artery is clearly shown and superimposed on the MIP image (see [Figure 4.25\(b\)](#)).

The proposed symbolic representation method was implemented with *Python*. The processing time of the whole procedure depends a lot on the image, *e.g.*, image size, resolution, number of branches of the vascular network. As an example, on the desktop computer with two cores 2.4GHz processors, 8GB internal memory, for one clinical image ([Figure 4.24](#)) it takes around 1 hour. For the synthetic image ([Figure 4.17](#)) it takes approximately 15 minutes.

Table 4.2: The different geometrical parameters of one clinical dataset

Branch number	0	1	2	3	4	5	6	7	8	9	10
Edge of the branch	3 → 6	6 → 2	6 → 9	9 → 11	9 → 10	10 → 5	10 → 4	5 → 1	5 → 8	4 → 7	4 → 0
Volume (voxel)	3238	460	10342	8182	3272	14420	1364	918	238	976	2274
Volume ( $mm^3$ )	1605	228	5126	4055	1621	7148	676	455	118	484	1127
Mean radius (voxel)	5.9	1.7	4.6	3.0	4.9	4.5	2.4	5.4	3.1	1.8	1.4
Mean radius ( $mm^3$ )	2.9	0.85	2.26	1.47	2.41	2.23	1.18	2.68	1.53	0.87	0.72
Length (voxel)	15	25	79	149	22	114	38	5	4	50	172
Length (mm)	5.31	8.85	27.97	52.76	7.79	40.36	13.45	1.77	1.41	17.70	60.90

## 4.5 DISCUSSION

We have proposed an automated approach for 3D symbolic representation in the application of AVM in order to facilitate the embolization planning by combining

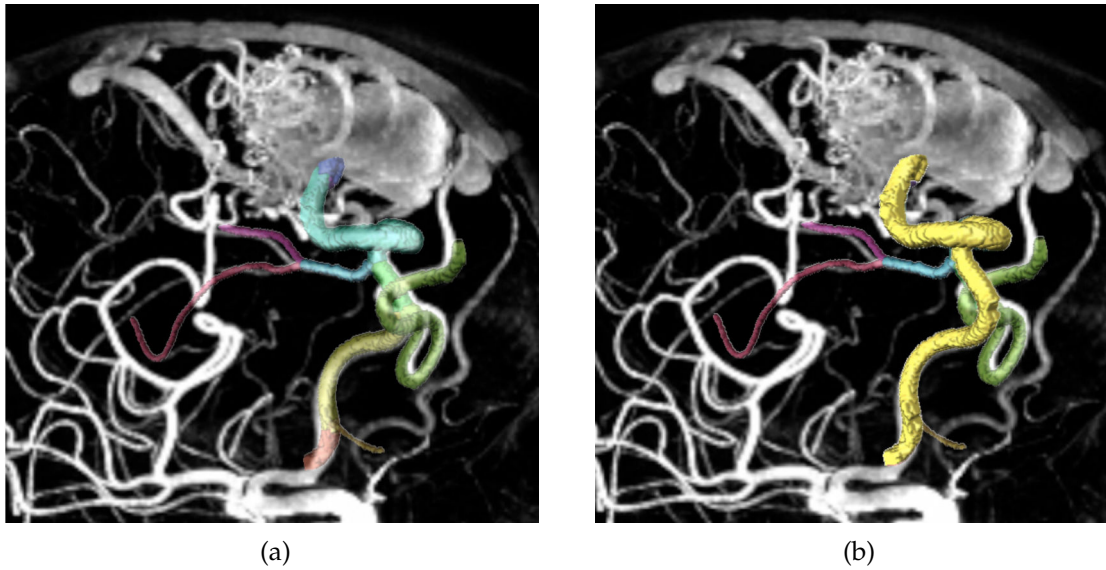


Figure 4.25: Overlay of the obtained results on MIP images. (a) Vessel tree decomposition with the graph-based approach and the related MIP image. (b) The principal feeding artery of the nidus, in yellow.

the segmentation results, the skeleton and the corresponding graph. Firstly, our proposed approach provides the possibility to distinguish solely the selected part of vascular sub-trees by depiction from its graph representation. This gives us a better visualization of the vascular network, especially locally.

Secondly, our method reveals the parent-child relationship of vessels. By means of topology analysis, each vessel segment is attributed a hierarchical level, allowing the neurosurgeon to visualize the vessels connected to nidus, and thus identify the vessels that can be safely occluded. In addition, we can determine the possible navigation path between two junction points and provide their geometric properties, such as radius (mean and instant), volume, length and tortuousness.

Thirdly, geometry features of each vascular segment are calculated by our approach, such as length, radius, volume, direction and tortuousness. Obviously, a good knowledge of vascular parameters are of great interests for the intervention planning. In clinical practice, the features could only be measured manually on medical images, whereas the accuracy is not always guaranteed due to problem of projection overlapping and human bias. In our approach, the geometry properties are obtained automatically by combining the segmentation results, the skeleton and the corresponding graph.

The segmentation results were qualitatively validated by the neuro-radiologists and present a more complete vascular network than those produced by the con-

ventional clinical software. The principal feeding arteries and draining veins connected to the nidus can be clearly identified from the reconstruction result. The Strahler ordering study obtained from the skeleton enables a description of brain vascular network tree-like model. This hierarchy model aids to simulate the navigation of embolization, finding the shortest path from the ICA to the embolization positions. It gives a better and more selective visualization of the vascular network and AVM, as well as its feeding and draining parts. In addition, the symbolic description allows describing an object, resulting from imaging, by the local characteristics. Moreover, many possibilities for future research including the use of geometrical and topological descriptors of vascular network are at our doorstep.

Our current methodology has several limitations. First, the processing time is long with desktop computer. The most time-consuming step is the decomposition of the vascular network into branches, the conversion step from graph to segmentation. This step can be parallelized in the future.

In the part of the vascular-network analysis, when decomposing the vascular tree into branches, the arbitrary choice of voxel belonging to a branch can cause a non-reproducibility. A more sophisticated junction and branch decomposition technique like in [175] can be used. In this method, the decomposition scheme is based on a partition of space according to tubes, inspired by the definition of Voronoi diagram. In such a way, this problem is turned into the evaluation of implicit functions over the surface, which seems to be robust to different geometry and bifurcation types.

Few intersections can be observed if two or more vessels are tangent and thus the topological representation is erroneous. This can be overcome by analysis for presence of cycles and further separation of the vessels. Antiga *et al.* [184] proposed vessel detection and decomposition schemes based on a partition of space according to tubes, inspired by the definition of Voronoi diagram. Thanks to centerlines, bifurcating vessels are synthetically represented by the envelopes of maximal inscribed spheres, or tubes. From tubes and their mutual intersection, an origin and a bifurcation plane are defined, which serve as absolute reference for the following steps. Thanks to this approach, the bifurcation decomposition problem is turned into the evaluation of implicit functions over the surface

Another possibility to kissing vessels correction is proposed in [185] to locally correct an existing segmentation based on the geometry of the detected incorrectly segmented regions. It can be done by analyzing paths inside the cycle region and

by straightness estimation of these paths and based on this disconnecting the vessels. See Figure 4.26 for an example.

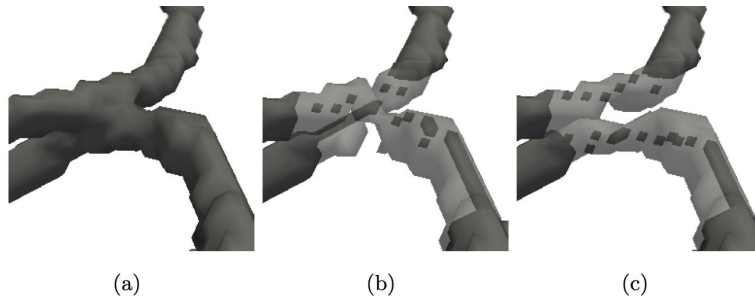


Figure 4.26: (a) Original segmentation. (b) Resulting (incorrect) adjustment of the segmentation using CS-D. (c) Resulting (correct) adjustment of the segmentation using CS (the paths used for the new segmentation are marked in a darker color than the corrected segmentation) [185].

In addition, other possible geometry measures can be calculated: local direction change, path straightness, thickness variation amplitude, path amplitude, frequency and rotation frequency [186].

Moreover, geometrical measures should be combined with the symbolic representation in the form of graph as weights or labels of the graph for trajectory calculation. In this case, it is of interest to combine the different geometry features in one single value (via a formula) as a weight of each graph vertex. For a given path, the maximum (or minimum) sum of the vertices will give the clinician an indication of the easiest path for the catheterization.

Another possibility for such a weighted graph is to augment the graph with more informative labels and use the concept of *label transfer* [187], as in case of functional atlas availability.



## CONCLUSION

---

### 5.1 CONTRIBUTIONS

This thesis aims to bring assistance to the neuro-radiologist in the perception, the interpretation and the exploitation of 3D Rotational Angiographic (3DRA) images of cerebral ArterioVenous Malformations (AVM).

Our contributions are based on a specific 3D region-growing segmentation algorithm proved to be efficient on these images. This automated algorithm starts by geodesic reconstruction applied to a single slice that provides a segmented image from which automatically are placed seed points devoted to the initialization of the region growing process.

This algorithm results in the segmentation of the whole AVM network. It directly leads to a first significant contribution that consists to get an improved visualization of AVM network which has a very complex structure.

On the other hand, a symbolic representation is deduced from the segmented vascular tree. First a skeletonization is performed using an Isthmus-based asymmetric thinning algorithm. The skeleton is decomposed into simple and terminal points, junctions and segments, from which a directed graph is built. The proposed method establishes a link between the segmented image, the skeleton and the graph, to allow vessel visualization and navigation. The whole vascular tree is decomposed to single vessel branches and for each segment, hierarchical and geometrical features are calculated to enrich the symbolic representation of the vascular tree.

Moreover, we use topological relations of the graph to provide the possibility to isolate a part of the vascular network. Thus the clinician, for instance, can obtain the vascular path relying two points which are selected interactively. This is a precious result both for understanding the complex structure of AVM and for

planning or assisting neuroradiologist interventions.

The proposed symbolic representation algorithm is not specific of either imaging modality or AVM network characteristics. It could be extended and applied to every anatomical segmented network.

Besides, we succeed in separating the three compartments of AVM: the feeding arteries, the nidus and the draining veins. This is a very innovative and promising result on this particularly complex network. This breakthrough and the whole work reported in this thesis constitutes a significant progress towards the modelization of AVM.

All this work was both validated on synthetic images and on a dataset of ten patients.

## 5.2 PERSPECTIVES

The promising results obtained in this work can benefit of complementary developments described below.

### 1) **Increase the interactivity of the graphic interface**

To apply the proposed method for clinical experiments, a software incorporated with graphic interface is under way. It will allow the neuroradiologists to interactively obtain different vessel characteristics and visualizations. More precisely, for the segmentation step, the one and only parameter involved is optimized while the obtained result is visualized and evaluated in real time. This application will also permit creating the symbolic representation for the entire segmentation as well as for local regions inside a selected polygon. The user will be able to choose a part of vascular network between two junctions for geometrical measurements, and finally, for an embolization simulation.

There is already an example of a similar software [126] called *VesselExplorer* (Figure 5.1). It integrates facilities to explore vascular trees. A subtree is selected and the vessel centerline is included. Based on the selection, various analyses techniques may be enabled. For example, distances may be measured, histograms of cross-sections may be displayed and annotations may be added. With this

program, detail-and-context visualizations, annotation and labelling are possible, and special branching types, such as trifurcations, are emphasized.

The other step forward from such software would be a possibility to modify the vessel geometry and topology in order to correct the image acquisition and segmentation errors and for intervention planning scenarios. Interventional procedures, such as coiling, stenting and AVM glue positioning as well as bypass operations, change the vessel geometry. It is, therefore, of importance to be able to simulate different scenarios of these procedures. Such modifications may be done either with a possibility to modify the vessel centerline and/or a possibility to specify the local vessel radius.

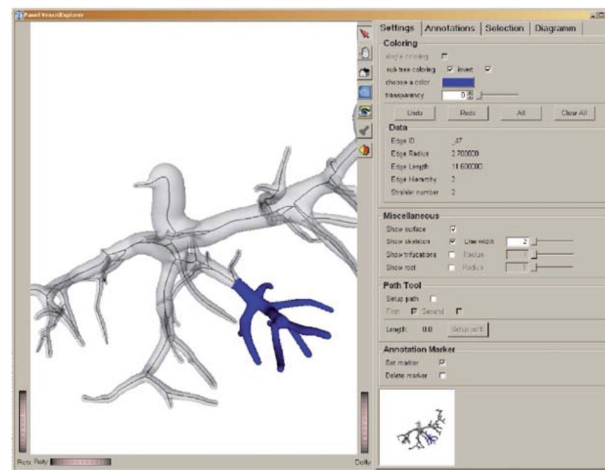


Figure 5.1: The VesselExplorer integrates facilities to explore vascular trees. A subtree is selected and the vessel centerline is included. Based on the selection various analyses techniques may be enabled. For example, distances may be measured, histograms of cross-sections may be displayed and annotations may be added [126].

## 2) Extensions for clinical application

Moreover, during the clinical intervention the neuro-radiologist only has access to a biplane classical angiographic image which provides poor 3D information on the spatial topology of the network. It would be very useful to register these angiographic images with our 3D representation of vascular tree (as it is shown in Figure 4.25).

## 3) Enrichment of symbolic representation

In our work, we enriched symbolic representation by attaching features to each junction and vessel branch, but we did not develop the exploitation of this information to increase the understanding of the complex AVM network. We still have to make that connection.

A major perspective would be to estimate the blood flow in segments of the vascular network by associating geometrical measurements and luminance ones because the intensity of pixels is related to the quantity of contrast product passing through the vessel. Indeed, in the case of AVM, the blood flow can absolutely not be approximated from geometrical information. For instance an artery with a small diameter can feed the nidus in a very important manner while that can be the opposite for an artery with a large one. Consequently, the addition of the estimation of blood flow in our modelization could be a very significant progress for medical aided-diagnosis, and to assist neuroradiologist for planning and intervention.

# Part I

## Annexes



## ANNEXES

## A.1 GEODESIC RECONSTRUCTION

The morphological geodesic reconstruction is a simple but powerful mathematical morphology tool that can be used to reconstruct objects from a binary marker image, remove objects touching image borders or fill holes. A marker image is required as input of geodesic reconstruction while the original image is used as a mask. The marked objects are reconstructed; the other ones are removed.

The geodesic reconstruction is performed on a grayscale image using two thresholds. The lower threshold ( $Thres_{low}$ ) is used to denoise the image and isolate the specific areas of interest and the upper threshold ( $Thres_{high}$ ) is defined to identify markers corresponding to the regions to be extracted. The combination of the two obtained binary images is then used to extract object regions from the original image.

Let  $I$  be a grayscale image and  $Thres_{low}$  and  $Thres_{high}$  two thresholds ( $Thres_{low} < Thres_{high}$ ), which respectively leads to the two binary images called  $J$  and  $K$ . Let  $J_1, J_2, \dots, J_m$  be the connected components of  $J$  and  $K_1, K_2, \dots, K_m$  be the connected components of  $K$ . Since it is easily proved that  $K \subseteq J$ ,  $K$  is called marker and  $J$  is called mask. The reconstruction  $R_{J(k)}$  of mask  $J$  from marker  $K$  is the union of the connected components of  $J$  which contains at least one common pixel with  $K$ :

$$R_J(k) = \cup\{J_i \mid K \cap J_i \neq \emptyset\} \quad (\text{A.1})$$

## A.2 DISTANCE REGULARIZED LEVEL SET EVOLUTION

The *Distance regularized Level Set Evolution* or DRLSE, is a new formulation of variational level set based method, the regularity of contours is inherently maintained during their evolution by calculating a regularized distance, which eliminates the need to reset the contour while keeping its accuracy. The energy function of DRLSE is expressed as:

$$\varepsilon(\phi) = \alpha R_p(\phi) + \beta L_g(\phi) + \mu A_g(\phi) \quad (\text{A.2})$$

with  $\phi(x, y, t)$  the level set function defined in the region,  $\Omega$ ,  $\alpha$  and  $\beta, \mu$  are the coefficients of these weighting functions:

$$R_p(\phi) = \int_{\Omega} p(|\nabla\Phi|) dx \quad (\text{A.3})$$

$$L_g(\phi) = \int_{\Omega} g\delta(\Phi)(|\nabla\Phi|) dx \quad (\text{A.4})$$

$$A_g(\phi) = \int_{\Omega} gH(-\Phi) dx \quad (\text{A.5})$$

where  $R_p(\phi)$  the regularization term against  $\Phi$ . To prevent the reset step,  $p$  should be minimal when  $|\nabla\Phi| = 1$ , so a simple example of  $p$  can be presented as:

$$p|\nabla\Phi| = 1 - |\nabla\Phi|^2 \quad (\text{A.6})$$

The other two energy terms depend on the image information,  $g$  is the gradient indicator, defined as:

$$g = \frac{1}{1 + |\nabla I|^2} \quad (\text{A.7})$$

$\delta(\Phi)$  is the Dirac function and  $H(\Phi)$  is Heaviside function.  $L_g(\phi)$  is minimum when  $\phi$  is located on the contour of the object.  $A_g(\phi)$  serves to accelerate the evolution speed of  $\phi$  when it is far from the object. Thus, the evolution of the

Level Set function in [Equation A.2](#) can be easily obtained by deriving the total energy:

$$\frac{\partial \phi}{\partial t} = \mu \operatorname{div} \left( \frac{p'(|\Phi|)}{|\nabla \Phi|} \nabla \phi \right) + \rho \delta \varepsilon(\Phi) \operatorname{div} \left( g \frac{\nabla \phi}{|\nabla \Phi|} \right) + \alpha g \delta \varepsilon(\phi) \quad (\text{A.8})$$



## BIBLIOGRAPHY

---

- [1] Bernhard Preim and Heinz-Otto Peitgen. Smart 3d visualizations in clinical applications. In *Smart Graphics*, pages 79–90. Springer, 2003.
- [2] Sigmund Oskar Steinheil. *Über einen Fall von Varix aneurysmaticus im Bereich der Gehirngefäße*. PhD thesis, Druck v. F. Fromme, 1895.
- [3] Xavier Combaz, O Levrier, J Moritz, J Mancini, JM Regis, JM Bartoli, and N Girard. Three-dimensional rotational angiography in the assessment of the angioarchitecture of brain arteriovenous malformations. *Journal of Neuroradiology*, 38(3):167–174, 2011.
- [4] Sean Mullan, Saeid Mojtahedi, Douglas L Johnson, and R Loch MacDonald. Cerebral venous malformation-arteriovenous malformation transition forms. *Journal of neurosurgery*, 85(1):9–13, 1996.
- [5] Wyatt L Ramey, Nikolay L Martirosyan, Joseph M Zabramski, Robert F Spetzler, and M Yashar S Kalani. A hierarchical model for the development of cerebral arteriovenous malformations. *Clinical neurology and neurosurgery*, 126:126–129, 2014.
- [6] Pierre Lasjaunias. A revised concept of the congenital nature of cerebral arteriovenous malformations. *Interventional Neuroradiology*, 3(4):275–281, 1997.
- [7] GE Perret and H Nishioka. Report on the cooperative study of intracranial aneurysms and subarachnoid hemorrhage. section vi. arteriovenous malformations. an analysis of 545 cases of cranio-cerebral arteriovenous malformations and fistulae reported to the cooperative study. *Journal of neurosurgery*, 25(4):467, 1966.
- [8] Rustam Al-Shahi and Charles Warlow. A systematic review of the frequency and prognosis of arteriovenous malformations of the brain in adults. *Brain*, 124(10):1900–1926, 2001.
- [9] C Hofmeister, C Stapf, A Hartmann, RR Sciacca, U Mansmann, P Lasjaunias, JP Mohr, H Mast, J Meisel, et al. Demographic, morphological, and clinical characteristics of 1289 patients with brain arteriovenous malformation. *Stroke*, 31(6):1307–1310, 2000.

- [10] DH Duong, A Hartmann, S Isaacson, RM Lazar, RS Marshall, H Mast, JP Mohr, J Pile-Spellman, RR Sciacca, M Sisti, et al. Arteriovenous malformations of the brain in adults. *New England Journal of Medicine*, 340(23):1812–1818, 1999.
- [11] Hunt H Batjer, Michael D Devous Sr, Burton G Seibert, Phillip D Purdy, and Frederick J Bonte. Intracranial arteriovenous malformation: relationship between clinical factors and surgical complications. *Neurosurgery*, 24(1):75–79, 1989.
- [12] Jonathan Stuart Citow, Robert Loch Macdonald, and Daniel Refai. *Comprehensive neurosurgery board review*. Thieme, 2010.
- [13] Francisco A Ponce and Robert F Spetzler. Arteriovenous malformations: classification to cure. *Clin Neurosurg*, 58:10–12, 2011.
- [14] K Radhakrishnan, PP Ashok, R Sridharan, and ME Mousa. Stroke in the young: incidence and pattern in benghazi, libya. *Acta neurologica scandinavica*, 73(4):434–438, 1986.
- [15] Robert D Brown Jr. Simple risk predictions for arteriovenous malformation hemorrhage. *Neurosurgery*, 46(4):1024, 2000.
- [16] John C Chaloupka and Daniel C Huddle. Classification of vascular malformations of the central nervous system. *Neuroimaging clinics of North America*, 8(2):295–321, 1998.
- [17] Robert F Spetzler and Neil A Martin. A proposed grading system for arteriovenous malformations. *Journal of neurosurgery*, 65(4):476–483, 1986.
- [18] Michael T Lawton, Helen Kim, Charles E McCulloch, Bahar Mikhak, and William L Young. A supplementary grading scale for selecting patients with brain arteriovenous malformations for surgery. *Neurosurgery*, 66(4):702, 2010.
- [19] E De Oliveira, Helder Tedeschi, and Jair Raso. Comprehensive management of arteriovenous malformations. *Neurological research*, 20(8):673–683, 1998.
- [20] Herbert Olivecrona and Johannes Riives. Arteriovenous aneurysms of the brain: their diagnosis and treatment. *Archives of Neurology & Psychiatry*, 59(5):567–602, 1948.

- [21] MG Yaşargil, KK Jain, J Antic, and R Laciga. Arteriovenous malformations of the splenium of the corpus callosum: microsurgical treatment. *Surgical neurology*, 5(1):5–14, 1976.
- [22] Ian G Fleetwood and Gary K Steinberg. Arteriovenous malformations. *The Lancet*, 359(9309):863–873, 2002.
- [23] Mark G Hamilton and Robert F Spetzler. The prospective application of a grading system for arteriovenous malformations. *Neurosurgery*, 34(1):2–7, 1994.
- [24] Carlo Schaller, Johannes Schramm, and Dorothee Haun. Significance of factors contributing to surgical complications and to late outcome after elective surgery of cerebral arteriovenous malformations. *Journal of Neurology, Neurosurgery & Psychiatry*, 65(4):547–554, 1998.
- [25] Alfredo Conti, Antonio Pontoriero, Giuseppe Faragò, Federica Midili, Carmelo Siragusa, Francesca Granata, Antonio Pitrone, Costantino De Renzi, Marcello Longo, and Francesco Tomasello. Integration of three-dimensional rotational angiography in radiosurgical treatment planning of cerebral arteriovenous malformations. *International journal of radiation oncology*, 81(3):29–37, Nov 2011.
- [26] Dimitre Hristov, Lina Liu, John R Adler, Iris C Gibbs, Teri Moore, Marily Sarmiento, Steve D Chang, Robert Dodd, Michael Marks, and Huy M Do. Technique for targeting arteriovenous malformations using frameless image-guided robotic radiosurgery. *International Journal of Radiation Oncology Biology Physics*, 79(4):1232–1240, 2011.
- [27] John C Flickinger, Douglas Kondziolka, Ann H Maitz, and L Dade Lunsford. An analysis of the dose-response for arteriovenous malformation radiosurgery and other factors affecting obliteration. *Journal of the European Society for Therapeutic Radiology and Oncology*, 63(3):347–54, Jun 2002.
- [28] Yoshihiro Yamamoto, Robert J Coffey, Douglas A Nichols, and E G Shaw. Interim report on the radiosurgical treatment of cerebral arteriovenous malformations. the influence of size, dose, time, and technical factors on obliteration rate. *Journal of neurosurgery*, 83(5):832–7, Nov 1995.
- [29] Bengt Karlsson, Ingmar Lax, and Michael Soderman. Can the probability for obliteration after radiosurgery for arteriovenous malformations be accu-

- rately predicted? *International Journal of Radiation Oncology Biology Physics*, 43(2):313–319, 1999.
- [30] Marc Kotowski, Asita Sarrafzadeh, Bawarjan Schatlo, Colette Boex, Ana Paula Narata, Vitor Mendes Pereira, Philippe Bijlenga, and Karl Schaller. Intraoperative angiography reloaded: a new hybrid operating theater for combined endovascular and surgical treatment of cerebral arteriovenous malformations: a pilot study on 25 patients. *Acta neurochirurgica*, 155(11):2071–8, Nov 2013.
- [31] Hans Henkes, Hans-Christean Nahser, Elisabeth Berg-Dammer, Werner Weber, Silke Lange, and D Kühne. Endovascular therapy of brain avms prior to radiosurgery. *Neurological research*, 20(6):479–492, 1998.
- [32] Y Pierre Gobin, Alexandre Laurent, Louis Merienne, Maurice Schlienger, Armand Aymard, Emmanuel Houdart, Alfredo Casasco, Dimitri Lefkopoulos, Bernard George, and Jean Jacques Merland. Treatment of brain arteriovenous malformations by embolization and radiosurgery. *Journal of neurosurgery*, 85(1):19–28, 1996.
- [33] Christopher S Ogilvy, Philip E Stieg, Issam Awad, Robert D Brown, Douglas Kondziolka, Robert Rosenwasser, William L Young, and George Hadenmenos. Recommendations for the management of intracranial arteriovenous malformations a statement for healthcare professionals from a special writing group of the stroke council, american stroke association. *Circulation*, 103(21):2644–2657, 2001.
- [34] Norman E Leeds and Stephen A Kieffer. Evolution of diagnostic neuroradiology from 1904 to 1999 1. *Radiology*, 217(2):309–318, 2000.
- [35] Sven Ivar Seldinger. Catheter replacement of the needle in percutaneous arteriography: a new technique. *Acta radiologica*, 39(5):368–376, 1953.
- [36] Suzie Bash, J Pablo Villablanca, Reza Jahan, Gary Duckwiler, Monica Tillis, Chelsea Kidwell, Jeffrey Saver, and James Sayre. Intracranial vascular stenosis and occlusive disease: evaluation with ct angiography, mr angiography, and digital subtraction angiography. *American journal of neuroradiology*, 26(5):1012–21, May 2005.

- [37] Jean-Philippe Dillenseger and Elisabeth Moerschel. *Guide des technologies de l'imagerie médicale et de la radiothérapie: quand la théorie éclaire la pratique*. Elsevier Masson, 2009.
- [38] M Matsumoto, N Kodama, Y Endo, J Sakuma, Ky Suzuki, T Sasaki, K Murakami, KE Suzuki, T Katakura, and F Shishido. Dynamic 3d-ct angiography. *American journal of neuroradiology*, 28(2):299–304, 2007.
- [39] Michael S Vaphiades, Joel Cure, and Lanning Kline. Management of intracranial aneurysm causing a third cranial nerve palsy: Mra, cta or dsa? *Seminars in ophthalmology*, 23(3):143–50, 2008.
- [40] Richard Bitar, General Leung, Richard Perng, Sameh Tadros, Alan R Moody, Josee Sarrazin, Caitlin McGregor, Monique Christakis, Sean Symons, Andrew Nelson, and Timothy P Roberts. Mr pulse sequences: what every radiologist wants to know but is afraid to ask. *Radiographics*, 26(2):513–37, 2006.
- [41] Heng-Hua Chang, Gary R Duckwiler, Daniel J Valentine, and Woei Chyn Chu. Computer-assisted extraction of intracranial aneurysms on 3d rotational angiograms for computational fluid dynamics modeling. *Medical physics*, 36(12):5612–21, Dec 2009.
- [42] Olena Tankyevych. *Filtering of thin objects: applications to vascular image analysis*. PhD thesis, Université Paris-Est, 2010.
- [43] Noboru Niki, Yoshiki Kawata, Hitoshi Satoh, and Tatsuo Kumazaki. 3d imaging of blood vessels using x-ray rotational angiographic system. In *Nuclear Science Symposium and Medical Imaging Conference, 1993., 1993 IEEE Conference Record.*, pages 1873–1877. IEEE, 1993.
- [44] Beth A Schueler, David F Kallmes, and Harry J Cloft. 3d cerebral angiography: radiation dose comparison with digital subtraction angiography. *American journal of neuroradiology*, 26(8):1898–1901, 2005.
- [45] D Gosch, W Kurze, F Deckert, T Schulz, A Patz, and T Kahn. Radiation exposure with 3d rotational angiography of the skull. *RoFo: Fortschritte auf dem Gebiete der Rontgenstrahlen und der Nuklearmedizin*, 178(9):880–885, 2006.
- [46] Carlo Cavedon, Frank Bova, William R Hendee, et al. Three-dimensional rotational angiography (3dra) adds substantial information to radiosurgery

- treatment planning of avm's compared to angio-ct and angio-mr. *Medical physics*, 31(8):2181–2183, 2004.
- [47] Marie-Odile Berger, René Anxionnat, Erwan Kerrien, Luc Picard, and Michael Söderman. A methodology for validating a 3d imaging modality for brain avm delineation: Application to 3dra. *Computerized Medical Imaging and Graphics*, 32(7):544–553, 2008.
- [48] J Moret, R Kemkers, J Op De Beek, R Kloppe, E Klotz, and M Grass. 3d rotational angiography: Clinical value in endovascular treatment. *Medicamundi*, 42:8–14, 1998.
- [49] David Fiorella, Felipe C Albuquerque, Henry H Woo, Cameron G McDougall, and Peter A Rasmussen. The role of neuroendovascular therapy for the treatment of brain arteriovenous malformations. *Neurosurgery*, 59(5):S3–163, 2006.
- [50] Yukinari Kakizawa, Hisashi Nagashima, Fusakazu Oya, Kiyoshi Ito, Yuichiro Tanaka, Kazuhiro Hongo, and Shigeaki Kobayashi. Compartments in arteriovenous malformation nidi demonstrated with rotational three-dimensional digital subtraction angiography by using selective microcatheterization: Report of three cases. *Journal of neurosurgery*, 96(4):770–774, 2002.
- [51] Florian Weiler, Christian Rieder, CA David, C Wald, and Horst K Hahn. Avm-explorer: Multi-volume visualization of vascular structures for planning of cerebral avm surgery. *Spring Eurograp*, 6:2–5, 2011.
- [52] Esther J Kim, Sandra Vermeulen, Francisco J Li, and David W Newell. A review of cerebral arteriovenous malformations and treatment with stereotactic radiosurgery. *Translational Cancer Research*, 3(4):399–410, 2014.
- [53] Philippe Gailloud. Endovascular treatment of cerebral arteriovenous malformations. *Techniques in vascular and interventional radiology*, 8(3):118–128, 2005.
- [54] Cemil Kirbas and Francis Quek. A review of vessel extraction techniques and algorithms. *ACM Computing Surveys (CSUR)*, 36(2):81–121, 2004.
- [55] David Lesage, Elsa D Angelini, Isabelle Bloch, and Gareth Funka-Lea. A review of 3d vessel lumen segmentation techniques: Models, features and extraction schemes. *Medical image analysis*, 13(6):819–845, 2009.

- [56] Jasjit S Suri, Kecheng Liu, Laura Reden, and Swamy Laxminarayan. A review on mr vascular image processing algorithms: acquisition and pre-filtering: part i. *IEEE transactions on information technology in biomedicine*, 6(4):324–337, 2002.
- [57] Petr Felkel, Rainer Wegenkittl, and Armin Kanitsar. Vessel tracking in peripheral cta datasets-an overview. In *Computer Graphics, Spring Conference on, 2001.*, pages 232–239. IEEE, 2001.
- [58] Maryam Taghizadeh Dehkordi, Saeed Sadri, and Alimohamad Doosthoseini. A review of coronary vessel segmentation algorithms. *Journal of medical signals and sensors*, 1(1):49, 2011.
- [59] Muhammad Moazam Fraz, P Remagnino, Andreas Hoppe, Bunyarit Uyyanonvara, Alicja R Rudnicka, Christopher G Owen, and Sarah A Barman. Blood vessel segmentation methodologies in retinal images—a survey. *Computer methods and programs in biomedicine*, 108(1):407–433, 2012.
- [60] Ursula Gonzales-Barron and Francis Butler. A comparison of seven thresholding techniques with the k-means clustering algorithm for measurement of bread-crumbs by digital image analysis. *Journal of food engineering*, 74(2):268–278, 2006.
- [61] Rui Gan, Wilbur C K Wong, and Albert C S Chung. Statistical cerebrovascular segmentation in three-dimensional rotational angiography based on maximum intensity projections. *Medical physics*, 32(9):3017–28, Sep 2005.
- [62] Boming Zhang, ZhengWei Xing, Jianfeng He, Sanli Yi, and Lei Ma. Local optimal threshold segmentation and reconstruction of cerebrovascular mra images. In *Biomedical Engineering and Informatics (BMEI), 2012 5th International Conference on*, pages 300–303. IEEE, 2012.
- [63] Do Yeon Kim and Jong Won Park. Connectivity-based local adaptive thresholding for carotid artery segmentation using mra images. *Image Vision Comput.*, 23(14):1277–1287, December 2005.
- [64] Rui Wang, Chao Li, Jie Wang, Xiaoe Wei, Yuehua Li, Yuemin Zhu, and Su Zhang. Threshold segmentation algorithm for automatic extraction of cerebral vessels from brain magnetic resonance angiography images. *Journal of neuroscience methods*, 241:30–6, Feb 2015.

- [65] Michael HF Wilkinson. Gaussian-weighted moving-window robust automatic threshold selection. In *Computer Analysis of Images and Patterns*, pages 369–376. Springer, 2003.
- [66] Josef Kittler, John Illingworth, and J Föglein. Threshold selection based on a simple image statistic. *Computer vision, graphics, and image processing*, 30(2):125–147, 1985.
- [67] Marco Boegel, Philip Hoelter, Thomas Redel, Andreas Maier, Joachim Hornegger, and Arnd Doerfler. A fully-automatic locally adaptive thresholding algorithm for blood vessel segmentation in 3d digital subtraction angiography. In *Engineering in Medicine and Biology Society (EMBC), 2015 37th Annual International Conference of the IEEE*, pages 2006–2009. IEEE, 2015.
- [68] Albert Chung, J Alison Noble, and Paul Summers. Vascular segmentation of phase contrast magnetic resonance angiograms based on statistical mixture modeling and local phase coherence. *IEEE Transactions on Medical Imaging*, 23(12):1490–1507, 2004.
- [69] Xin Gao, Yoshikazu Uchiyama, Xiangrong Zhou, Takeshi Hara, Takahiko Asano, and Hiroshi Fujita. A fast and fully automatic method for cerebrovascular segmentation on time-of-flight (tof) mra image. *Journal of digital imaging*, 24(4):609–25, Aug 2011.
- [70] Vicent Caselles, Ron Kimmel, and Guillermo Sapiro. Geodesic active contours. *International journal of computer vision*, 22(1):61–79, 1997.
- [71] Monica Hernandez and Alejandro F Frangi. Non-parametric geodesic active regions: Method and evaluation for cerebral aneurysms segmentation in 3dra and cta. *Medical image analysis*, 11(3):224–241, 2007.
- [72] Roberto Sanz-Requena, David Moratal, Diego Ramón García-Sánchez, Vicente Bodí, José Joaquín Rieta, and Juan Manuel Sanchis. Automatic segmentation and 3d reconstruction of intravascular ultrasound images for a fast preliminar evaluation of vessel pathologies. *Computerized medical imaging and graphics*, 31(2):71–80, Mar 2007.
- [73] Azadeh Firouzian, Rashindra Manniesing, Zwenneke H Flach, Roelof Risselada, Fop van Kooten, Miriam CJM Sturkenboom, Aad van der Lugt, and Wiro J Niessen. Intracranial aneurysm segmentation in 3d ct angiography:

- Method and quantitative validation with and without prior noise filtering. *European Journal of Radiology*, 79(2):299–304, 2011.
- [74] Xunlei Wu, Vincent Luboz, Karl Krissian, Stephane Cotin, and Steve Dawson. Segmentation and reconstruction of vascular structures for 3d real-time simulation. *Medical image analysis*, 15(1):22–34, 2011.
- [75] Chunming Li, Chenyang Xu, Changfeng Gui, and Martin D Fox. Distance regularized level set evolution and its application to image segmentation. *IEEE Transactions on Image Processing*, 19(12):3243–3254, 2010.
- [76] Heng-Hua Chang and Daniel J Valentino. An electrostatic deformable model for medical image segmentation. *Computerized Medical Imaging and Graphics*, 32(1):22–35, 2008.
- [77] Benoît Caldaïrou. Arbre des composantes connexes: méthodologie et application à la segmentation d’images médicales. Technical report, Technical report Laboratoire des Sciences de l’Image, de l’Informatique et de la Télé-détection Université Jean Monnet–Saint-Etienne.
- [78] Hrvoje Bogunović, José María Pozo, Rubén Cárdenes, and Alejandro F Frangi. Automatic identification of internal carotid artery from 3dra images. In *Engineering in Medicine and Biology Society (EMBC), 2010 Annual International Conference of the IEEE*, pages 5343–5346. IEEE, 2010.
- [79] Maximilien Vermandel, Nacim Betrouni, Christian Taschner, Christian Vasseur, and Jean Rousseau. From mip image to mra segmentation using fuzzy set theory. *Computerized medical imaging and graphics*, 31(3):128–40, Apr 2007.
- [80] Nils Daniel Forkert, Till Illies, Einar Goebell, Jens Fiehler, Dennis Säring, and Heinz Handels. Computer-aided nidus segmentation and angiographic characterization of arteriovenous malformations. *International journal of computer assisted radiology and surgery*, 8(5):775–86, Sep 2013.
- [81] Nils Daniel Forkert, Alexander Schmidt-Richberg, Jens Fiehler, Till Illies, Dietmar Möller, Dennis Säring, Heinz Handels, and Jan Ehrhardt. 3d cerebrovascular segmentation combining fuzzy vessel enhancement and level-sets with anisotropic energy weights. *Magnetic resonance imaging*, 31(2):262–271, 2013.

- [82] Ramesh Jain, Rangachar Kasturi, and Brian G Schunck. *Machine vision*, volume 5. McGraw-Hill New York, 1995.
- [83] Michiel Schaap, Lisan Neefjes, Coert Metz, Alina van der Giessen, Annick Weustink, Nico Mollet, Jolanda Wentzel, Theo van Walsum, and Wiro Niessen. Coronary lumen segmentation using graph cuts and robust kernel regression. In *Information Processing in Medical Imaging*, pages 528–539. Springer, 2009.
- [84] Yoshitaka Masutani, Thomas Schiemann, and Karl-Heinz Höhne. Vascular shape segmentation and structure extraction using a shape-based region-growing model. In *Medical Image Computing and Computer-Assisted Intervention*, pages 1242–1249. Springer, 1998.
- [85] Hiroyuki Sekiguchi, Naozo Sugimoto, Shigeru Eiho, Takashi Hanakawa, and Shinichi Urayama. Blood vessel segmentation for head mra using branch-based region growing. *Systems and Computers in Japan*, 36(5):80–88, 2005.
- [86] Huiyan Jiang, Baochun He, Di Fang, Zhiyuan Ma, Benqiang Yang, and Libo Zhang. A region growing vessel segmentation algorithm based on spectrum information. *Computational and mathematical methods in medicine*, 2013, 2013.
- [87] Tobias Boskamp, Daniel Rinck, Florian Link, Bernd Kummerlen, Georg Stamm, and Peter Mildenerger. New vessel analysis tool for morphometric quantification and visualization of vessels in ct and mr imaging data sets 1. *Radiographics*, 24(1):287–297, 2004.
- [88] Nicolas Passat, Christian Ronse, Joseph Baruthio, Jean-Paul Armspach, Claude Maillot, and Christine Jahn. Region-growing segmentation of brain vessels: an atlas-based automatic approach. *Journal of magnetic resonance imaging*, 21(6):715–25, Jun 2005.
- [89] Qing Cao, Yang Chen, Guanyu Yang, Christine Toumoulin, Huazhong Shu, and Limin Luo. Coronary vessel extraction method using an improved minimum path based region growing. In *Biomedical Engineering and Informatics (BMEI), 2013 6th International Conference on*, pages 127–131. IEEE, 2013.
- [90] Yang Chen, Qing Cao, Zhikun Zhuang, Zhou Yang, Limin Luo, and Christine Toumoulin. 3-d coronary vessel extraction using a novel minimum

- path based region growing. In *Image Analysis and Recognition*, pages 502–509. Springer, 2013.
- [91] Shan Wang, Bonian Li, and Shoujun Zhou. A segmentation method of coronary angiograms based on multi-scale filtering and region-growing. In *Biomedical Engineering and Biotechnology (iCBEB), 2012 International Conference on*, pages 678–681. IEEE, 2012.
- [92] Yanli Li, Shoujun Zhou, Jianhuang Wu, Xin Ma, and Kewen Peng. A novel method of vessel segmentation for x-ray coronary angiography images. In *Computational and Information Sciences (ICCIS), 2012 Fourth International Conference on*, pages 468–471. IEEE, 2012.
- [93] Alejandro F Frangi, Wiro J Niessen, Koen L Vincken, and Max A Viergever. Multiscale vessel enhancement filtering. In *Medical Image Computing and Computer-Assisted Intervention*, pages 130–137. Springer, 1998.
- [94] KASH Kulathilake, L Ranathunga, GR Constantine, and NA Abdullah. Region growing segmentation method for extracting vessel structures from coronary cine-angiograms. In *Moratuwa Engineering Research Conference (MERCon), 2015*, pages 142–147. IEEE, 2015.
- [95] Muder M Almi’ani and Buket D Barkana. A modified region growing based algorithm to vessel segmentation in magnetic resonance angiography. In *Systems, Applications and Technology Conference (LISAT), 2015 IEEE Long Island*, pages 1–7. IEEE, 2015.
- [96] Maciej Orkisz, M Hernández Hoyos, V Pérez Romanello, C Pérez Romanello, JC Prieto, and C Revol-Muller. Segmentation of the pulmonary vascular trees in 3d ct images using variational region-growing. *IRBM*, 35(1):11–19, 2014.
- [97] Juan Antonio Martínez-Mera, Pablo G Tahoces, José M Carreira, Jorge Juan Suárez-Cuenca, and Miguel Souto. A hybrid method based on level set and 3d region growing for segmentation of the thoracic aorta. *Computer Aided Surgery*, 18(5-6):109–117, 2013.
- [98] Rolf Adams and Leanne Bischof. Seeded region growing. *IEEE Transactions on Pattern Analysis and Machine Intelligence*, 16(6):641–647, 1994.

- [99] Nicolas Passat. *Contribution à la segmentation des réseaux vasculaires cérébraux obtenus en IRM: Intégration de connaissance anatomique pour le guidage d'outils de morphologie mathématique*. PhD thesis, Strasbourg 1, 2005.
- [100] Nicolas Passat, Christian Ronse, Joseph Baruthio, J-P Armspach, and C Maillot. Magnetic resonance angiography: from anatomical knowledge modeling to vessel segmentation. *Medical image analysis*, 10(2):259–74, Apr 2006.
- [101] Danilo Babin, A Pižurica, Rik Bellens, Johan De Bock, Yanfeng Shang, Bart Goossens, Ewout Vansteenkiste, and Wilfried Philips. Generalized pixel profiling and comparative segmentation with application to arteriovenous malformation segmentation. *Medical image analysis*, 16(5):991–1002, 2012.
- [102] Danilo Babin, Aleksandra Pižurica, Jonas De Vylder, Ewout Vansteenkiste, and Wilfried Philips. Brain blood vessel segmentation using line-shaped profiles. *Physics in medicine and biology*, 58(22):8041–61, Nov 2013.
- [103] Martino Pesaresi and Jon Atli Benediktsson. A new approach for the morphological segmentation of high-resolution satellite imagery. *IEEE Transactions on Geoscience and Remote Sensing*, 39(2):309–320, 2001.
- [104] Antonio Plaza, Pablo Martinez, Rosa Perez, and Javier Plaza. A new approach to mixed pixel classification of hyperspectral imagery based on extended morphological profiles. *Pattern Recognition*, 37(6):1097–1116, 2004.
- [105] Alice Dufour, Olena Tankyevych, Benoît Naegel, Hugues Talbot, Christian Ronse, Joseph Baruthio, Petr Dokládál, and Nicolas Passat. Filtering and segmentation of 3d angiographic data: Advances based on mathematical morphology. *Medical image analysis*, 17(2):147–164, 2013.
- [106] Olena Tankyevych, Hugues Talbot, Petr Dokládál, and Nicolas Passat. Direction-adaptive grey-level morphology. application to 3d vascular brain imaging. In *Image Processing (ICIP), 2009 16th IEEE International Conference on*, pages 2261–2264. IEEE, 2009.
- [107] Qingfen Lin. *Enhancement, detection, and visualization of 3D volume data*. PhD thesis, Linköping University, Department of Electrical Engineering, 2001.
- [108] Odyssee Merveille, Hugues Talbot, Laurent Najman, and Nicolas Passat. Tubular structure filtering by ranking orientation responses of path operators. In *Computer Vision—ECCV 2014*, pages 203–218. Springer, 2014.

- [109] Yoshinobu Sato, Shin Nakajima, Nobuyuki Shiraga, Hideki Atsumi, Shigeyuki Yoshida, Thomas Koller, Guido Gerig, and Ron Kikinis. Three-dimensional multi-scale line filter for segmentation and visualization of curvilinear structures in medical images. *Medical image analysis*, 2(2):143–68, Jun 1998.
- [110] Karl Krissian, Grégoire Malandain, Nicholas Ayache, Régis Vaillant, and Yves Troussel. Model-based detection of tubular structures in 3d images. *Computer vision and image understanding*, 80(2):130–171, 2000.
- [111] Piotr Orłowski and Maciej Orkisz. Efficient computation of hessian-based enhancement filters for tubular structures in 3d images. *IRBM*, 30(3):128–132, 2009.
- [112] Jinzhu Yang, Shuang Ma, Qi Sun, Wenjun Tan, Mengjia Xu, Nan Chen, and Dazhe Zhao. Improved hessian multiscale enhancement filter. *Bio-medical materials and engineering*, 24(6):3267–3275, 2014.
- [113] Elizabeth Bullitt, Stephen Aylward, Estrada J Bernard Jr, and Guido Gerig. Computer-assisted visualization of arteriovenous malformations on the home personal computer. *Neurosurgery*, 48(3):576–583, 2001.
- [114] Marcela Hernández-Hoyos. *Segmentation anisotrope 3D pour la quantification en imagerie vasculaire par résonance magnétique*. PhD thesis, Villeurbanne, INSA, 2002.
- [115] Gady Agam and Changhua Wu. Probabilistic modeling based vessel enhancement in thoracic ct scans. In *Computer Vision and Pattern Recognition, 2005. CVPR 2005. IEEE Computer Society Conference on*, volume 2, pages 649–654. IEEE, 2005.
- [116] Stefan Wesarg and Evelyn A Firle. Segmentation of vessels: the corkscrew algorithm. In *Medical Imaging 2004*, pages 1609–1620. International Society for Optics and Photonics, 2004.
- [117] Leslie Verscheure, Laurent Peyrodie, Anne-Sophie Dewalle, Nicolas Reyns, Nacim Betrouni, Serge Mordon, and Maximilien Vermandel. Three-dimensional skeletonization and symbolic description in vascular imaging: preliminary results. *International journal of computer assisted radiology and surgery*, 8(2):233–246, 2013.

- [118] L Florez Valencia, A Morales Pinzón, J-C Richard, M Hernandez Hoyos, and M Orkisz. Simultaneous skeletonization and graph description of airway trees in 3d ct images. In *XXVème Colloque GRETSI*, 2015.
- [119] Caroline Lacoste, Gérard Finet, and Isabelle E Magnin. Coronary tree extraction from x-ray angiograms using marked point processes. In *Biomedical Imaging: Nano to Macro, 2006. 3rd IEEE International Symposium on*, pages 157–160. IEEE, 2006.
- [120] Nicolas Flasque, Michel Desvignes, Jean-Marc Constans, and Marinette Revenu. Modélisation de structures tubulaires pour la visualisation 3d: application à des imageries d’angiographie par résonance magnétique. In *RFIA’2002-13e Congrès Reconnaissance des Formes et Intelligence Artificielle*, volume 3, pages 733–742, 2002.
- [121] Rahul Prasanna Kumar, Fritz Albrechtsen, Martin Reimers, Bjørn Edwin, Thomas Langø, and Ole Jakob Elle. Blood vessel segmentation and center-line tracking using local structure analysis. In *6th European Conference of the International Federation for Medical and Biological Engineering*, pages 122–125. Springer, 2015.
- [122] Alejandro F Frangi, Wiro J Niessen, Romhild M Hoogeveen, Theo Van Walsum, and Max A Viergever. Model-based quantitation of 3-d magnetic resonance angiographic images. *IEEE Transactions on Medical Imaging*, 18(10):946–956, 1999.
- [123] Frédéric Clarençon, Franck Maizeroi-Eugène, Damien Bresson, Flavien Maingreud, Nader Sourour, Claude Couquet, David Ayoub, Jacques Chiras, Catherine Yardin, and Charbel Mounayer. Elaboration of a semi-automated algorithm for brain arteriovenous malformation segmentation: initial results. *European radiology*, 25(2):436–43, Feb 2015.
- [124] Y Kiran Kumar, Shashi B Mehta, and Manjunath Ramachandra. Segmentation of nidus–brain avm. *International Journal of Science and Technology*, 4(2), 2014.
- [125] Ihar Volkau, Ting Ting Ng, Yevgen Marchenko, and Wieslaw L Nowinski. On geometric modeling of the human intracranial venous system. *IEEE Transactions on Medical Imaging*, 27(6):745–751, 2008.

- [126] Bernhard Preim and Steffen Oeltze. 3d visualization of vasculature: an overview. In *Visualization in medicine and life sciences*, pages 39–59. Springer, 2008.
- [127] Christian Schumann, Steffen Oeltze, Ragnar Bade, Bernhard Preim, and Heinz-Otto Peitgen. Model-free surface visualization of vascular trees. In *EuroVis*, pages 283–290. Citeseer, 2007.
- [128] Armin Kanitsar, Rainer Wegenkittl, Dominik Fleischmann, and Meister Eduard Groller. Advanced curved planar reformation: Flattening of vascular structures. In *Proceedings of the 14th IEEE Visualization 2003 (VIS'03)*, page 7. IEEE Computer Society, 2003.
- [129] Karel Jan Zuiderveld. Visualization of multimodality medical volume data using object-oriented methods. *Utrecht University, Utrecht, the Netherlands*, 92, 1995.
- [130] Zhiguang Zhou, Yubo Tao, Hai Lin, Feng Dong, and Gordon Clapworthy. Shape-enhanced maximum intensity projection. *The Visual Computer*, 27(6-8):677–686, 2011.
- [131] William E Lorensen and Harvey E Cline. Marching cubes: A high resolution 3d surface construction algorithm. In *ACM siggraph computer graphics*, volume 21, pages 163–169. ACM, 1987.
- [132] Gabriel Taubin. A signal processing approach to fair surface design. In *Proceedings of the 22nd annual conference on Computer graphics and interactive techniques*, pages 351–358. ACM, 1995.
- [133] Yoshitaka Masutani, Ken Masamune, and Takeyoshi Dohi. Region-growing based feature extraction algorithm for tree-like objects. In *Visualization in Biomedical Computing*, pages 159–171. Springer, 1996.
- [134] Horst K Hahn, Bernhard Preim, Dirk Selle, and Heinz-Otto Peitgen. Visualization and interaction techniques for the exploration of vascular structures. In *Visualization, 2001. VIS'01. Proceedings*, pages 395–578. IEEE, 2001.
- [135] Elizabeth Bullitt, Stephen Aylward, Alan Liu, Jeffrey Stone, Suresh K Mukherji, Chris Coffey, Guido Gerig, and Stephen M Pizer. 3d graph description of the intracerebral vasculature from segmented mra and tests of accuracy by comparison with x-ray angiograms. In *Information Processing in Medical Imaging*, pages 308–321. Springer, 1999.

- [136] Luc Vincent. Morphological grayscale reconstruction in image analysis: applications and efficient algorithms. *IEEE Transactions on Image Processing*, 2(2):176–201, 1993.
- [137] Robert M Haralick and Linda G Shapiro. Image segmentation techniques. *Computer vision, graphics, and image processing*, 29(1):100–132, 1985.
- [138] T Yung Kong and Azriel Rosenfeld. Digital topology: Introduction and survey. *Computer Vision, Graphics, and Image Processing*, 48(3):357–393, 1989.
- [139] Y Huang, Z-C Duan, G-L Zhu, and S-H Gong. A fast triangulation algorithm for 3d reconstruction from planar contours. *The International Journal of Advanced Manufacturing Technology*, 24(1-2):98–101, 2004.
- [140] Yu Qian Zhao, Xiao Hong Wang, Xiao Fang Wang, and Frank Y Shih. Retinal vessels segmentation based on level set and region growing. *Pattern Recognition*, 47(7):2437–2446, 2014.
- [141] Michel Couprie and Gilles Bertrand. Topology preserving alternating sequential filter for smoothing two-dimensional and three-dimensional objects. *Journal of Electronic Imaging*, 13(4):720–730, 2004.
- [142] Piotr Orlowski, Paul Summers, J Alison Noble, James Byrne, and Yiannis Ventikos. Computational modelling for the embolization of brain arteriovenous malformations. *Medical engineering & physics*, 34(7):873–881, 2012.
- [143] Piotr Orlowski, Imran Mahmud, Mudassar Kamran, Paul Summers, Alison Noble, Yiannis Ventikos, and James V Byrne. An approach to the symbolic representation of brain arteriovenous malformations for management and treatment planning. *Neuroradiology*, 56(3):195–209, Mar 2014.
- [144] Antonio Di Ieva, Mounir Boukadoum, Salim Lahmiri, and Michael D Cusi-mano. Computational analyses of arteriovenous malformations in neuroimaging. *Journal of Neuroimaging*, 25(3):354–360, 2015.
- [145] Gilles Bertrand and Grégoire Malandain. A new topological classification of points in 3d images. In *Computer Vision—ECCV’92*, pages 710–714. Springer, 1992.
- [146] Gilles Bertrand and Grégoire Malandain. A new characterization of three-dimensional simple points. *Pattern Recognition Letters*, 15(2):169–175, 1994.

- [147] Ingela Nyström and Orjan Smedby. New presentation method for magnetic resonance angiography images based on skeletonization. In *Medical Imaging 2000*, pages 515–522. International Society for Optics and Photonics, 2000.
- [148] Nicu D Cornea, Deborah Silver, and Patrick Min. Curve-skeleton properties, applications, and algorithms. *IEEE transactions on visualization and computer graphics*, 13(3):530–48, 2007.
- [149] Stina Svensson and Gabriella Sanniti di Baja. Simplifying curve skeletons in volume images. *Computer Vision and Image Understanding*, 90(3):242–257, 2003.
- [150] Punam K Saha, Robin Strand, and Gunilla Borgefors. Digital topology and geometry in medical imaging: a survey. *IEEE Transactions on Medical Imaging*, 34(9):1940–1964, 2015.
- [151] Leslie Verscheure, Laurent Peyrodie, N Makni, N Betrouni, S Maouche, and M Vermandel. Dijkstra’s algorithm applied to 3d skeletonization of the brain vascular tree: Evaluation and application to symbolic. In *Engineering in Medicine and Biology Society (EMBC), 2010 Annual International Conference of the IEEE*, pages 3081–3084. IEEE, 2010.
- [152] Fethallah Benmansour and Laurent D Cohen. Tubular structure segmentation based on minimal path method and anisotropic enhancement. *International Journal of Computer Vision*, 92(2):192–210, 2011.
- [153] Ashirwad Chowriappa, Yong Seo, Sarthak Salunke, Maxim Mokin, Peter Kan, and Peter Scott. 3-d vascular skeleton extraction and decomposition. *IEEE journal of biomedical and health informatics*, 18(1):139–47, Jan 2014.
- [154] Gilles Bertrand. New notions for discrete topology. In *Discrete Geometry for Computer Imagery*, pages 218–228. Springer, 1999.
- [155] Michel Couprie and Gilles Bertrand. Asymmetric parallel 3d thinning scheme and algorithms based on isthmuses. *Pattern Recognition Letters*, 2015.
- [156] Carlo Arcelli and Gabriella Sanniti Di Baja. A width-independent fast thinning algorithm. *IEEE Transactions on Pattern Analysis and Machine Intelligence*, (4):463–474, 1985.
- [157] Ta-Chih Lee, Rangasami L Kashyap, and Chong-Nam Chu. Building skeleton models via 3-d medial surface axis thinning algorithms. *CVGIP: Graphical Models and Image Processing*, 56(6):462–478, 1994.

- [158] Gábor Németh, Péter Kardos, and Kálmán Palágyi. Thinning combined with iteration-by-iteration smoothing for 3d binary images. *Graphical Models*, 73(6):335–345, 2011.
- [159] Gunilla Borgefors. On digital distance transforms in three dimensions. *Computer vision and image understanding*, 64(3):368–376, 1996.
- [160] Dakai Jin and Punam K Saha. A new fuzzy skeletonization algorithm and its applications to medical imaging. In *Image Analysis and Processing–ICIAP 2013*, pages 662–671. Springer, 2013.
- [161] YF Tsao and King Sun Fu. A parallel thinning algorithm for 3-d pictures. *Computer graphics and image processing*, 17(4):315–331, 1981.
- [162] Christian Ronse. A topological characterization of thinning. *Theoretical Computer Science*, 43:31–41, 1986.
- [163] T Yung Kong. Minimal non-deletable sets and minimal non-codeletable sets in binary images. *Theoretical Computer Science*, 406(1):97–118, 2008.
- [164] Christophe Lohou. Detection of the non-topology preservation of ma and sonka’s algorithm, by the use of p-simple points. *Computer Vision and Image Understanding*, 114(3):384–399, 2010.
- [165] Kálmán Palágyi. A 3d fully parallel surface-thinning algorithm. *Theoretical Computer Science*, 406(1):119–135, 2008.
- [166] Kálmán Palágyi. A 3-subiteration 3d thinning algorithm for extracting medial surfaces. *Pattern Recognition Letters*, 23(6):663–675, 2002.
- [167] Cherng-Min Ma and Shu-Yen Wan. Parallel thinning algorithms on 3d (18, 6) binary images. *Computer Vision and Image Understanding*, 80(3):364–378, 2000.
- [168] Kalman Palágyi and Attila Kuba. A hybrid thinning algorithm for 3d medical images. *Journal of computing and information technology*, 6(2):149–164, 1998.
- [169] Gilles Bertrand. P-simple points: A solution for parallel thinning. In *5th Conf. on Discrete Geometry*, number 1, pages 233–242, 1995.

- [170] Gilles Bertrand and Michel Couprie. Two-dimensional parallel thinning algorithms based on critical kernels. *Journal of Mathematical Imaging and Vision*, 31(1):35–56, 2008.
- [171] Michael Grass, Holger Schmitt, Volker Rasche, S Haehnel, Oliver Schramm, M Hartmann, and K Sartor. A method for 3d flow determination based on x-ray rotational angiography. In *International Congress Series*, volume 1230, pages 408–414. Elsevier, 2001.
- [172] Zhongyuan Qin, Xuanqin Mou, and Ruofei Zhang. A 3d modeling scheme for cerebral vasculature from mra datasets. In *IEEE International Symposium on Computer-Based Medical Systems*, page 346, 2003.
- [173] Dirk Selle, Bernhard Preim, Andrea Schenk, and Heinz-Otto Peitgen. Analysis of vasculature for liver surgical planning. *IEEE transactions on medical imaging*, 21(11):1344–57, Nov 2002.
- [174] Adam Sankowski and Andrzej Materka. Mathematical morphology analysis of 3d mra images of human brain for estimation of blood vessels parameters. In *New Trends in Audio & Video and Signal Processing: Algorithms, Architectures, Arrangements, and Applications (NTAV/SPA), 2012 Joint Conference*, pages 49–52. IEEE, 2012.
- [175] Marina Piccinelli, Alessandro Veneziani, David Steinman, Andrea Remuzzi, Luca Antiga, et al. A framework for geometric analysis of vascular structures: application to cerebral aneurysms. *IEEE Transactions on Medical Imaging*, 28(8):1141–1155, 2009.
- [176] Arthur N Strahler. Quantitative analysis of watershed geomorphology. *Eos, Transactions American Geophysical Union*, 38(6):913–920, 1957.
- [177] David A Nordsletten, Shane Blackett, Michael D Bentley, Erik L Ritman, and Nicolas P Smith. Structural morphology of renal vasculature. *American journal of physiology*, 291(1):H296–309, Jul 2006.
- [178] Zouina Aktouf, Gilles Bertrand, and Laurent Perroton. A three-dimensional holes closing algorithm. *Pattern Recognition Letters*, 23(5):523–531, 2002.
- [179] Ahmed Yureidini. *Robust blood vessel surface reconstruction for interactive simulations from patient data*. PhD thesis, Université des Sciences et Technologie de Lille-Lille I, 2014.

- [180] Preet Jassi and Ghassan Hamarneh. Vascusynth: Vascular tree synthesis software. *Insight Journal*, 2011.
- [181] Ghassan Hamarneh and Preet Jassi. Vascusynth: simulating vascular trees for generating volumetric image data with ground-truth segmentation and tree analysis. *Computerized medical imaging and graphics*, 34(8):605–616, 2010.
- [182] Xiao Han, Chenyang Xu, Ulisses Braga-Neto, and Jerry L Prince. Topology correction in brain cortex segmentation using a multiscale, graph-based algorithm. *IEEE Transactions on Medical Imaging*, 21(2):109–121, 2002.
- [183] Raphaël Blanc, Aude Seiler, Thomas Robert, Humain Baharvahdat, Maxime Lafarge, Julien Savatovsky, Jérôme Hodel, Gabriele Ciccio, Dorian Chauvet, Silvia Pistocchi, Bruno Bartolini, Hocine Redjem, and Michel Potin. Multi-modal angiographic assessment of cerebral arteriovenous malformations: a pilot study. *Journal of neurointerventional surgery*, Oct 2014.
- [184] Luca Antiga and David A Steinman. Robust and objective decomposition and mapping of bifurcating vessels. *IEEE Transactions on Medical Imaging*, 23(6):704–713, 2004.
- [185] Anneleen De Clercq. Accurate segmentation of vascular structures.
- [186] N Yu Ilyasova. Methods to evaluate the three-dimensional features of blood vessels. *Optical Memory and Neural Networks*, 24(1):36–47, 2015.
- [187] Roland Kwitt, Danielle Pace, Marc Niethammer, and Stephen Aylward. Studying cerebral vasculature using structure proximity and graph kernels. In *Medical Image Computing and Computer-Assisted Intervention*, pages 534–541. Springer, 2013.

